An investigation of a possible effect of reactor antineutrinos on the decay rate of ^{22}Na

By

Milton William van Rooy

Dissertation presented for the degree of Doctor of Natural Philosophy
in the Faculty of Science at Stellenbosch University

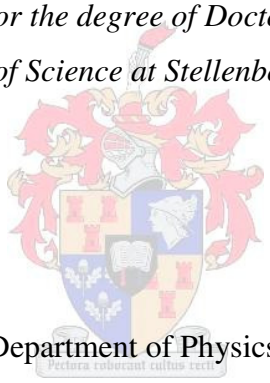

Department of Physics,
University of Stellenbosch,
Private Bag X1, Matieland 7602,
South Africa

Promoters:
Prof. Paul Papka
Dr. Frederick David Smit
Prof. Robert Johan de Meijer

March 2015

DECLARATION

By submitting this thesis/dissertation electronically, I declare that the entirety of the work contained therein is my own, original work, that I am the sole author thereof (save to the extent explicitly otherwise stated), that reproduction and publication thereof by Stellenbosch University will not infringe any third party rights and that I have not previously in its entirety or in part submitted it for obtaining any qualification.

Date: April 2015

ACKNOWLEDGEMENT

The financial assistance of the National Research Foundation (NRF) towards this research is hereby acknowledged. Opinions expressed and conclusions arrived at, are those of the author and are not necessarily to be attributed to the NRF.

ABSTRACT

Reported claims of a solar neutrino influence on radioactive β^--decay rates prompted a series of three long term measurements that were carried out at the Koeberg nuclear power plant North of Cape Town to investigate the mirror reaction of reactor antineutrinos with a β^+-source. The β^+-emitter ^{22}Na was exposed to a changing reactor antineutrino flux of the order of ~10^{12} $cm^{-2}s^{-1}$ through the various phases of reactor operation, from off to on or vice versa, to investigate the antineutrino effect on its decay rate. ^{22}Na sources were placed on the face of or inside a scintillation detector while γ-ray energy spectra were measured at source-to-reactor-core distances of 17 m and 23 m for reactor unit #1 and unit #2 respectively. The analytical method employed uses ratios of the net-peak count rates of the photopeaks in the γ-ray energy spectra while the antineutrino flux changes during the various phases of reactor operation. These ratios reduce some potential systematic factors such as dead time, but should also remain constant during all phases of reactor operation and be independent of antineutrino flux if antineutrinos have no significant effect on the decay rate of ^{22}Na. Measurement series 1 employed a $LaBr_3$(Ce) detector. Results indicated an effect between reactor-off and –on corresponding to an antineutrino interaction cross section upper limit of the order of barns, assuming that antineutrinos are indeed the cause. Subsequently, two confirmation measurements were performed using a normal (cylindrical) NaI(Tl) detector as well as a NaI(Tl) well-counter. Results of these two measurements did not indicate any correlation with the reactor status. Measurements series 3 proved to be the most sensitive measurement for detecting changes in the decay rate of ^{22}Na and an upper limit of ~10^{-25} cm^2 was estimated for the cross section of antineutrinos interacting with ^{22}Na. This upper limit is one order of magnitude smaller compared to measurements series 1 and two orders of magnitude smaller compared to measurement series 2. It is also one of magnitude smaller than the effect reported by Jenkins *et al.* and two orders of magnitude smaller than observed by de Meijer *et al*. at the Delft reactor. Considering the systematic effects encountered during each measurement series we find no significant evidence for antineutrinos affecting β^+-decay in ^{22}Na.

OPSOMMING

Berigte bewerings van son-afkomstige neutrinos se invloed op β^--verval het gelei tot drie lang termyn metings wat uitgevoer is by die Koeberg kernkrag stasie Noord van Kaapstad om die spieëldbeeld reaksie van antineutrinos met 'n β^+-bron te ondersoek. Die ^{22}Na β^+-bron is blootgestel aan 'n veranderende reaktor antineutrino vloed van die order ~10^{12} $cm^{-2}s^{-1}$ soos die reaktor deur verskeie fases van operasie gaan, vanaf afgeskakel na aangeskakel of omgekeerd, om die effek van antineutrinos op die bron se vervaltempo te ondersoek. ^{22}Na bronne was teen die voorkant of binne 'n sintillator detektor geplaas terwyl γ-straal energie spektra gemeet was by bron-tot-reaktor kern afstande van 17 m en 23 m vir reaktor eenheid #1 en #2 afsonderlik. Die analitiese metode gebruik verhoudings van die netto-piek teltempos van die fotopieke in die γ-straal energie spektra terwyl die antineutrino vloed verander tydens verskeie fases van reaktor operasie. Hierdie verhoudings verminder sekere potensiële systematiese effekte soos dooietyd en moet konstant bly tydens alle fases van reaktor operasie en moet ook onafhanklik wees van die antineutrino vloed indien antineutrinos geen effek het op die vervaltempo van ^{22}Na nie. Die eerste reeks metings het gebruik gemaak van 'n $LaBr_3$(Ce) detektor. Resultate het 'n effek getoon tussen reaktor-af en reaktor-aan wat ooreenstem met 'n boonste limiet vir die interaksie kansvlak van antineutrinos met grootteorde van barns, indien antineutrinos wel die oorsaak is. Twee reekse van opvolgende metings is uitgevoer wat gebruik gemaak het van 'n gewone (silindriese) NaI(Tl) detektor asook 'n NaI(Tl) put detektor. Resultate van hierdie metings het geen korrelasie met die reaktor status gewys nie. Die derde reeks metings was die sensitiefste om veranderinge in die verval tempo van ^{22}Na te wys en 'n boonste limiet vir die interaksie kansvlak van antineutrinos op ^{22}Na was beraam as ~10^{-25} cm^2. Hierdie boonste limiet is een grootteorde kleiner in vergelyking met reeks 1 en twee grootteordes kleiner as reeks 2. Dit is ook een grootteorde kleiner as die waarde van Jenkins *et al*. en twee grootteordes kleiner as wat de Meijer *et al*. berig het by die Delft reaktor. In agneming van die systematise probleme wat ondervind was tydens die drie reeks metings vind ons geen beduidende effek van antineutrinos op die vervaltempo van ^{22}Na nie.

ACKNOWLEDGEMENTS

I would like to thank my supervisors for their outstanding support throughout our project, mentoring me professionally as well as personally, shaping the way I think. I could not have asked for better supervisors. Our coffee break discussions and stroopwafels will be missed. In some circles Dr. Ricky Smit is known as Yoda, I am honoured to have been his pupil.

Without the support from personnel at Koeberg this project would not exist. The cooperation received from our Koeberg collaborators; Elmarie Welman, Steph Steyn and Ruan Steyn was superb. Thank you for accommodating us into your schedules and valuable discussions.

I am grateful to Stellenbosch University and iThemba LABS for providing facilities and equipment to carry out our project.

We thank C. Vermeulen for producing our ^{22}Na sources.

We are thankful to Peane Maleka assisting with Monte Carlo simulations and valuable discussions.

The EARTH foundation is thanked for its support of this project.

The European Space Agency is thanked for loaning the $LaBr_3$(Ce) detector.

The purchase of the NaI(Tl) well-counter was made possible through financial support from the Dutch Ministry of Foreign Affairs as part of the IAEA Member State Support Programme.

I thank Dr. Bruce Simpson for his valuable input and suggestions when we needed some expert advice.

Support from Prof. Robbie Lindsay is acknowledged.

The National Metrology Institute of South Africa (NMISA) is acknowledged for its financial support.

TABLE OF CONTENTS

LIST OF FIGURES

5.7 The effect of gain drift on the total count rate of spectra. As an example the ORTEC data is used. The E_γ = 511 keV peak channel position is on the left hand axis (blue) and the total count rate in the spectra is on the right hand axis (green). The time is relative to the start of the BG measurement on 13/04/2011 and is given in hours to simplify the following discussion.

5.8 Illustration of the effect of multiplicative and additive gain. c_1 And c_2 are the channels at which the peaks P_1 and P_2 should be after spectrum-stabilisation.

5.9 Positions of the E_γ = 511, 1275, 1470 and 1786 keV peaks after spectrum-stabilisation of one-hour spectra.

5.10 Mismatch of α-peak region above E_γ = 1960 keV in the spectrum-stabilised BG (top panel) and Na+BG (bottom panel) spectra during reactor-off and-on and at iTL.

5.11 Ratios of the peak positions R = $\frac{511\text{ keV}}{1275\text{ keV}}$, $\frac{511\text{ keV}}{1786\text{ keV}}$ and $\frac{1275\text{ keV}}{1786\text{ keV}}$ prior to spectrum-stabilisation of the Na+BG spectra, during reactor-off and-on and at iTL.

5.12 Standard deviations of the E_γ = 511, 1275 and 1786 keV peaks after spectrum-stabilisation.

5.13 Comparison of BG standard spectra measured during reactor-off and-on periods as well as at iTL in the energy range E_γ = 400 to 1400 keV.

5.14 Comparison of the hourly BG count rates in a wide ROI during reactor-off and-on as well as at iTL. The weighted mean during each period is also indicated by the solid horizontal lines.

5.15 A BG standard spectrum indicating the three gates used to investigate the BG count rates.

5.16 Best fit linear function to the ratios R_1 of Koeberg 26 Apr – 18 May 2011, Koeberg 18 – 21 May 2011 and Koeberg 14 – 30 June 2011.

5.17 Graphical representation of $\frac{\Delta P_{\beta_1}}{P_{\beta_1}}$ as a function of $\phi_{\bar{\nu}_e}$.

6.1 Comparison of Na+BG spectra measured with the NaI(Tl) (blue) and HPGe detector (green) on a log scale.

7.11 Decay corrected and normalised count rate in the energy region $143 < E_\gamma < 2475$ keV.

7.12 Half-life of ^{22}Na corresponding to the changes in count rate observed in the energy region $143 < E_\gamma < 2475$ keV. The literature value of the half-life of ^{22}Na (2.6027 (0.0010) y) is indicated by the solid horizontal line.

7.13 24 h Average gain correction factor applied to the Na+BG spectra as a function of time.

7.14 24 h Average dead time during the Na+BG measurement periods.

LIST OF TABLES

5.4 Net-peak count rates of the E_γ = 511, 662, 1173, 1333 and 1470 keV peaks in the average BG spectra during reactor-on and-off and at iTL.

5.5 Calculated decay constants and corresponding χ^2-values of ^{22}Na using the net-peak count rates of the E_γ = 511, 1275 and 1786 keV peaks during reactor-off and-on and at iTL.

5.6 Average net-peak count rates per hour in the E = 511, 1275 and 1786 keV peaks in the ^{22}Na standard spectra during the various measuring periods.

5.7 Ratios R_1 and R_2 during the various measuring periods and corresponding $\phi_{\bar{\nu}_e}$.

5.8 Relative change in the branching ratio β_1 as a function of antineutrino flux.

5.9 Change in the partial decay constants for case #1 and #2 as well as the corresponding interaction cross section for antineutrinos on the β^+ and electron capture decay branches of ^{22}Na, if antineutrinos were the cause. Also presented is the relative change in the total decay constant.

6.1 Summary of the quantity of data recorded with the NaI(Tl) detector during various phases of reactor operation of unit#1.

6.2 Summary of the quantity of BG data recorded with the HPGe detector during reactor-on and -of phases of unit#1.

6.3 Net-peak count rates of the E_γ = 511, 1275 and 1786 keV peaks before and after extending the linear continua by two channels.

6.4 Counting statistics of the six-hour average BG spectra in the energy region $143 < E_\gamma < 1909$ keV during the various periods while unit#1 is on.

6.5 Net-peak count rates of the E_γ = 511, 1173, 1333, 1461 and 2615 keV peaks in the average BG spectra as well as the count rate in the energy regions $143 < E_\gamma < 1568$ keV and $1569 < E_\gamma < 1909$ keV.

6.6 Net-peak count rates of the E_γ = 511, 1275 and 1786 keV peaks as well as the gross count rate in the energy region $1380 < E_\gamma < 1925$ keV, determined from a one-hour

BG corrected Na+BG spectrum using average BG from 16 to 21 February and from 27 June to 1 August, respectively.

6.7 Weighted mean of the 24 h average BG subtracted, decay corrected, and normalised count rate of the E_γ = 511 keV peak and gross count rate of the E_γ = 1275 keV peak and Gate I as well as the χ^2-value relative to the weighted mean.

6.8 Net-peak count rates in the E_γ = 511, 1275 and 1786 keV peaks of a one-hour BG subtracted Na+BG spectrum measured with the HPGe detector.

6.9 Average BG count rate during the two BG measurement periods in the energy regions $143 < E_\gamma < 1909$ keV, $143 < E_\gamma < 1568$ keV and $1569 < E_\gamma < 1909$ keV.

6.10 Change in the partial decay constants for case #1 and #2 as well as the corresponding interaction cross section for antineutrinos on the β^+ and electron capture decay branches of ^{22}Na, if antineutrinos were the cause. Also presented is the relative change in the decay constant.

7.1 Summary of the quantity of data recorded with the NaI(Tl) well-counter during various phases of reactor operation of unit#1.

7.2 Counting statistics of the hourly BG spectra in the energy region $143 < E_\gamma < 2958$ keV during various periods while unit#1 is on.

7.3 Net-peak count rates of $E\gamma$ = 511, 1173, 1333 and 2615 keV peaks in the average BG spectra as well as the count rate in the energy regions $143 < E\gamma < 467$ keV, $574 < E\gamma < 1352$ keV and $1352 < E\gamma < 1909$.

7.4 Net-peak count rates of the E_γ = 511, 1022, 1275, 1786 and 2297 keV peaks as well as the gross count rate in the energy region $143 < E_\gamma < 2958$ keV, determined from a one-hour BG corrected Na+BG spectrum using average BG from 14 to 31 December 2012 and 20 August to 8 October 2013, respectively.

7.5 Count rate in the energy region $143 < E_\gamma < 2475$ keV in the average BG spectra during the various BG measurement periods.

7.6 Mean of the ratio $\frac{\text{Gate II}}{\text{Gate I}}$ before and after the start of the decrease in this ratio.

7.7 Mean of the ratio $\frac{\text{Gross 1275 keV}}{\text{Gate I}}$ before and after a correction of 0.05% for the period between 24/03/2013 and 20/05/2013.

7.8 Mean of the corrected ratio $\frac{\text{Gross 1275 keV}}{\text{Gate I}}$ during reactor-off and-on.

7.9 Comparison of results obtained at Koeberg relative to that obtained by de Meijer et al.

8.1 Pros and cons of measurement series 1 to 3.

CHAPTER 1 Perspectives

1.1 Introduction

It is widely accepted that within uncertainties nuclear decay rates are constant and that nuclear decay follows an exponential function. Though this statement has been confirmed experimentally for many shorter half-life radionuclides it is more difficult to do so for longer half-life radionuclides such as ^{14}C ($t_{1/2}$ = 5700 (30) y [1]) [2]. During the past six years many articles have reported deviations from the exponential decay as observed in the count rate of γ-rays emitted during decay, primarily β^--decay, but also evidence against it [3 - 20].

One of the first and most popular figures illustrating nuclear decay fluctuations comes from the work of S. Alburger *et al.* in 1986 who determined the decay rate of ^{32}Si from the ratio of γ-ray counts of $\frac{^{32}Si}{^{36}Cl}$ [3]. Alburger *et al.* used an end-window gas-flow proportional counter to measure the β^--particles resulting from the β^--decay of ^{32}Si [12]. Silicon-32 ($t_{1/2}$ = 153 years) decays 100% by β^--decay to ^{32}P which has a half life of 14.262 (14) days [10]. The ^{32}Si point source used, already reached secular equilibrium before measurements were started [3]. A precision sample changer was used and comparative measurements were made of β^--particle counts from ^{36}Cl which has a half-life of 3.02×10^3 years [3]. Measurements started in 1982 at four-week intervals on each source for 40 hours each [3]. The ^{32}Si count rate was normalized to the ^{36}Cl count rate and fitted with an exponential, resulting in figure 1.1 showing periodic annual deviations with amplitude of 0.1% [3].

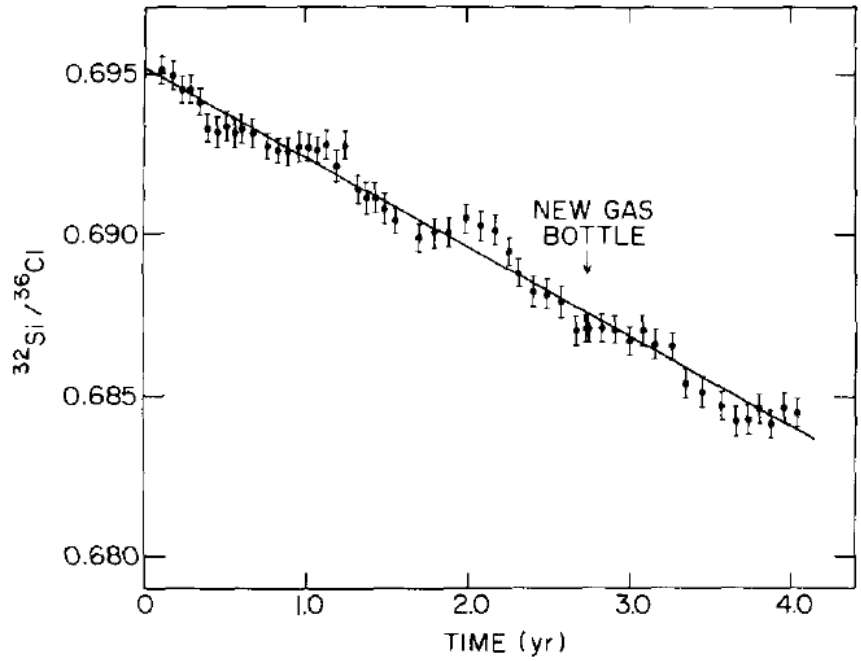

Figure 1.1: *Oscillations in the decay rate of ^{32}Si observed by Alburger et al. [3].*

A possibility that changes in temperature and relative humidity in the measuring area could have influenced the detector response and thus the $^{32}Si/^{36}Cl$ ratio is discussed, though no complete records are available, the assessment is based on records from other areas inside the same building [3]. Alburger *et al.* conclude that the deviations are of unknown origin and have no significant effect on their result [3].

In 2009 Jenkins *et. al.* reported on their reanalysis of the data collected by Alburger *et al.* using a the function $U(t) = \left[\frac{\dot{N}(t)}{\dot{N}_0}\right] e^{\lambda t}$ where $\frac{\dot{N}(t)}{\dot{N}_0}$ is the $^{32}Si/^{36}Cl$ count rate ratio, decay corrected with the value of λ used by Alburger *et al.*, $\lambda = 4.0299 \times 10^{-3}$ years^{-1} [4]. Figure 1.2 presents the result of the normalized U(t) as well the $\frac{1}{r^2}$ Earth-Sun distance as a function of time [4].

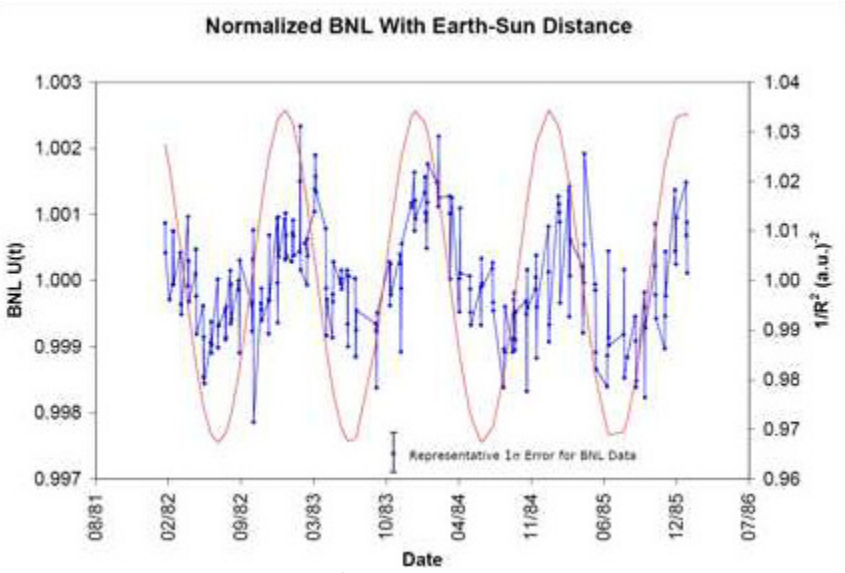

Figure 1.2: *Normalized U(t) (blue) and* $\frac{1}{r^2}$ *Earth-Sun distance (red) as a function of time [4].*

The fractional change in U(t) between perihelion and aphelion is reported to be approximately 3×10^{-3} [4]. A Pearson correlation coefficient of r = 0.52 is reported for N = 239 points resulting in a probability of 6×10^{-18} that the correlation between the count rate fluctuations and the variation in earth-Sun distance could have come from uncorrelated data.

Jenkins *et al*. also reanalysed 15 years of ^{226}Ra data collected with a pressurized 4π ionization chamber at the Physikalisch-Technische Bundesandstalt (PTB) in Germany of which the first 2 years overlap with the ^{32}Si data of Alburger *et al*. [4]. Measurements were made in current mode consisting of 30 individual measurements averaged over 3 days to obtain a data point [20]. Figure 1.3 presents the decay corrected and normalized count rates of ^{226}Ra as well the $\frac{1}{r^2}$ Earth-Sun distance as a function of time [4].

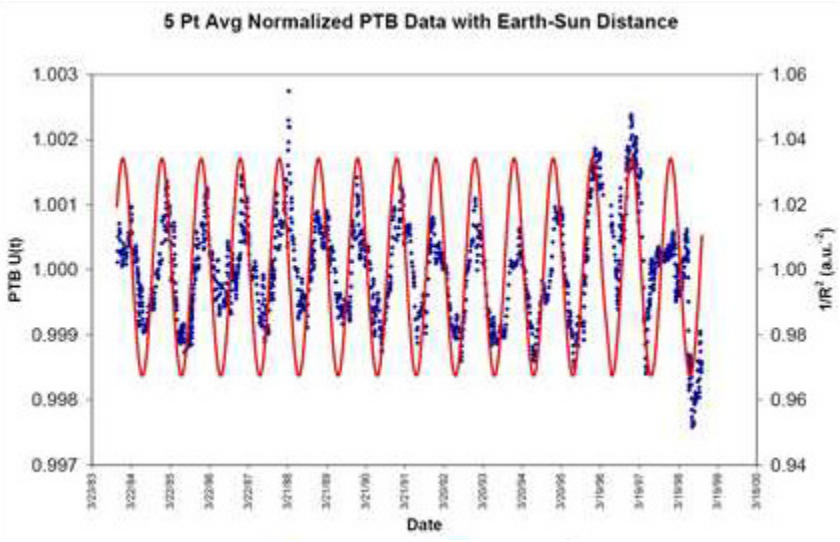

Figure 1.3: *Decay corrected and normalized* ^{226}*Ra count rates (blue) and* $\frac{1}{r^2}$ *Earth-Sun distance (red) as a function of time [4].*

Fluctuations of similar magnitude ~3 × 10^{-3} were observed in the ^{226}Ra data with a correlation coefficient of r = 0.66 for N = 1968 points corresponding to a probability of 2 × 10^{-246} that the correlation between the count rate fluctuations and the variation in Earth-Sun distance could have come from uncorrelated data [4]. Unlike Jenkins *et al*., Siegert *et al*. analyzed the ratio of count rates of ^{154}Eu/^{226}Ra and observed that the annual fluctuations vanished; concluding that the annual fluctuations observed in the individual source decay rates is due to fluctuations in the performance of the equipment used.

Still, Jenkins *et al*. conclude that they have presented evidence for decay rates (α- and β^--decay in this case) being modulated by a solar effect in terms of a varying solar neutrino flux as the Earth-Sun distance changes, or an undetected solar field of some sort [4].

Later in 2009 Jenkins *et al*. presented further evidence for their hypothesis, reporting a decrease in the decay rate of a ^{54}Mn point source during a solar flare occurring on 13 December 2006 which lasted for approximately 43 minutes [4]. ^{54}Mn γ-ray energy spectra were recorded with a 2”×2” NaI(Tl) detector connected to a pre-amplifier and main amplifier, feeding an MCA [4]. The location was an air conditioned room with a constant temperature of 19.5 (5) °C [4]. The count rate was measured for 4 hour live time period in a region of interest around the Eγ = 834.86 keV photopeak resulting from electron capture [4]. The measured count rate was compared to the expected exponential decay leading to a ~2 × 10^{-4} relative maximum decrease in count rate. Because the start of the decrease was observed

more than a day before X-ray and proton spikes were recorded by Geostationary Operational Environmental Satellites, a geomagnetic effect on the electronics (i.e. power surges) was ruled out as a cause. No details about background measurements or influences are given and therefore cannot be ruled out as a cause.

The main criticism about their approach is that they analyzed raw data obtained by a different group, without any knowledge of the measurement conditions, settings and variables, resulting in the data being taken at face value.

Table 1.1 provides the size of the effects observed in the fluctuations of the decay rates of ^{32}Si, ^{226}Ra and ^{54}Mn as well as the corresponding cross sections.

Table 1.1: *Relative size of effects observed by Jenkins et al. and the corresponding cross section.*

Nuclide	Main decay mode	Relative change in Activity	σ (cm^2)
^{32}Si	B^-	0.003	7.4×10^{-24}
^{226}Ra	α	0.003	7.1×10^{-25}
^{54}Mn	EC	0.0002	8.8×10^{-23}

Also in 2009 Semkow *et al*. showed that the fluctuations observed in the decay ^{226}Ra and ^{32}Si can be explained by systematic influences such as variations in temperature relative humidity and background radiation on proportional counters and ionization chambers [8].

In 2008 Cooper reported on the results of the thermal power output data of the three Radioisotope Thermoelectric Generators (RTG) aboard the Cassini spacecraft which was launched in 1997 and reached Saturn in 2004. Each RTG consisted of the α-emitter ^{238}Pu. The thermal power output is directly proportional to the decay rate of ^{238}Pu; producing heat [5]. During the spaceflight no significant effect on the decay rate of ^{238}Pu was observed over a 0.7 – 1.6 AU distance from the spacecraft to the Sun [5]. Cooper set an upper limit of $\sim 10^{-4}$ on fluctuations in the decay rate of ^{238}Pu [5], corresponding to $\sigma = 1.7 \times 10^{-25}$ cm^2.

In 2010 Parkhomov reported yearly oscillations of count rates measured with a Geiger-Müller detector, with magnitude of up to 0.2% from ^{60}Co and ^{90}Sr-^{90}Y β^--sources and no effect on ^{239}Pu measured with a Si-semiconductor, over a period of more than thirteen years [6]. Parkhomov only states that the analysis was performed via a Fast Fourier Transform [6].

Details of measurement conditions are not given. Parkhomov concludes that because effects are seen only on the β^--decaying ^{60}Co and ^{90}Sr-^{90}Y sources and not on the ^{239}Pu α-source, that an incoming flux of cosmic neutrinos or relic neutrinos are influencing β^--decay rates [6]. The effects seen in ^{60}Co and ^{90}Sr-^{90}Y correspond to $\sigma = 2.9 \times 10^{-24}$ cm^2 and $\sigma = 5.2 \times 10^{-25}$ cm^2, respectively.

In 2009 Norman *et al*. reported on evidence against the Jenkins hypothesis after reanalysing their own data obtained over a total of 15 years of measurements used to determine the half-lives of ^{44}Ti, ^{121}Sn^m and ^{108}Ag^m. During each measurement γ-ray energy spectra of mixed sources of ^{22}Na/^{44}Ti, ^{241}Am/^{121}Sn^m and ^{44}Ti/^{133}Ba/^{108}Ag^m were measured with HPGe detectors. Net-peak count rates were obtained by an average continuum subtraction obtained from equal energy widths above and below the photopeak of interest [7]. To minimize possible systematic effects/instabilities in the detectors due to the long term measurements, the ratios of net-peak count rates were analyzed [7]. Norman *et al*. point out that if the Jenkins hypothesis is true, it is highly unlikely that all modes of decay will be affected in quantitatively the same way, therefore the ratio of different nuclides should also show annual fluctuations [7]. After decay correcting both isotopes in the ratios, the ratio is normalized relative to the mean and the Pearson correlation coefficient is calculated for no annual variation, resulting in r = 0.9999, 0.994 and 0.999 for the respective measurements [7]. Norman *et al*. conclude that they find no evidence for correlations between the decay rates of the above mentioned radionuclides and the Earth-Sun distance and set upper limits of 0.06%, 0.024% and 0.004% on the amplitude of annual fluctuations in the decay rates, 2 to 37 times smaller than observed by Jenkins *et al*. [7].

Table 1.2 provides the size of the effects observed in the fluctuations of the decay rates of ^{22}Na, ^{44}Ti, ^{241}Am, ^{121}Sn^m, ^{44}Ti, ^{133}Ba and ^{108}Ag^m as well as the corresponding cross sections.

Table 1.2: *Relative size of effects observed by Norman et al. and the corresponding cross section.*

Nuclide	Main decay mode	Relative change in Activity	σ (cm^2)
^{44}Ti	EC	0.0006	3.8×10^{-24}
^{22}Na	B^+/EC	0.0006	8.7×10^{-23}
$^{121}Sn^m$	B^+/IT	0.00024	2.1×10^{-24}
^{241}Am	α	0.00024	2.1×10^{-25}
$^{108}Ag^m$	EC	0.00004	3.4×10^{-26}
^{133}Ba	EC	0.00004	1.4×10^{-24}

During the course of the following years many more reports of evidence for, as well as against a solar influence on decay rates have been published [3 - 20]. If the Jenkins hypothesis is true, it should also hold for the mirror reaction of antineutrinos with a β^+-source.

In a first experiment, measurements to test the above mentioned hypothesis have been carried out at a 2 MW_{th} reactor at the Reactor Institute Delft, in the Netherlands, with the CAFIA detector [21]. Nuclear reactors are anthropogenic sources of antineutrinos resulting from β^--decay of fission products. Contrary, solar neutrinos result from fission in the Sun. CAFIA is a 33% HPGe detector which was placed 8 m from the reactor core. Except for the top and the side not facing the reactor, the detector was surrounded by 10 cm of lead. Using the radioactive sources ^{152}Eu, ^{137}Cs, ^{54}Mn and ^{22}Na the effect of antineutrinos on β^+-decay was investigated by measuring γ-ray count rates. Apart from availability, these sources were chosen on the expectation that there is no effect on β^--decay and electron capture and can be used as a control. Measurements were made over a total period of 200 hours, including 65 hours when the reactor was switched off. Results of the experiment show no effect on γ-ray count rates and thus also the decay constants of ^{152}Eu, ^{137}Cs, ^{54}Mn and ^{22}Na. The upper limit of a possible influence of antineutrinos on the decay of ^{22}Na and ^{54}Mn was determined to be 2×10^{-4} corresponding to $\sigma = 3 \times 10^{-23}$ cm^2 at an antineutrino flux change of 4.7×10^{10} $cm^{-2}s^{-1}$. De Meijer *et al.* concluded that either the reactor antineutrino flux was not high enough to observe an effect or that antineutrinos might not have the same effect as neutrinos on β-decay [21].

A β^+-source does not have a threshold energy for decay to be induced by antineutrinos and in 1962 it was already suggested by S. Weinberg that the very low energy cosmological relic neutrino background could be measured using radionuclides [22]. Therefore, it is not excluded $\bar{\nu}_e$ can somehow interact with a radioactive nucleus N with greater probability than predicted:

$$\bar{\nu}_e + N \rightarrow N' + e^+. \tag{1.2}$$

As such it could provide a test of the suggestion of Jenkins *et al*. Cross-sections for neutrinos interacting with a range of β-decaying nuclei have been calculated by Cocco *et al*., listed in Table 1.3 [23]. Table 1.3 indicates that the interaction cross-sections are comparable to and even smaller than that of neutrinos interacting with free protons. Though, the highest interaction rate would be achieved with ^{3}H and ^{11}C.

Table 1.3: *Neutrino interaction cross-sections of $\beta^{\pm}$-decaying nuclei with a branching ratio greater than 80% β-decay [23].*

Isotope	Decay	Q_β (keV)	Half-life (sec)	$\sigma_{\mathrm{NCB}}(v_\nu/c)$ (10^{-41} cm^2)
^{3}H	β^-	18.591	3.8878×10^8	7.84×10^{-4}
^{63}Ni	β^-	66.945	3.1588×10^9	1.38×10^{-6}
^{93}Zr	β^-	60.63	4.952×10^{13}	2.39×10^{-10}
^{106}Ru	β^-	39.4	3.2278×10^7	5.88×10^{-4}
^{107}Pd	β^-	33	2.0512×10^{14}	2.58×10^{-10}
^{187}Re	β^-	2.64	1.3727×10^{18}	4.32×10^{-11}
^{11}C	β^+	960.2	1.226×10^3	4.66×10^{-3}
^{13}N	β^+	1198.5	5.99×10^2	5.3×10^{-3}
^{15}O	β^+	1732	1.224×10^2	9.75×10^{-3}
^{18}F	β^+	633.5	6.809×10^3	2.63×10^{-3}
^{22}Na	β^+	545.6	9.07×10^7	3.04×10^{-7}
^{45}Ti	β^+	1040.4	1.307×10^4	3.87×10^{-4}

Cross sections for neutrinos from accelerator neutrino beams on ^{12}C nuclei have also been measured from the KARMEN experiment resulting in cross sections of the order of ~10^{-42} cm^2 [24].

The cross sections determined through the previously discussed decay rate variation measurements range from ~10^{-23} cm^2 to ~10^{-26} cm^2 which is more than 16 orders of

magnitude larger than predicted by the Standard Model and values derived by Cocco *et al.* and clearly do not meet the level of sensitivity to test weak interaction processes.

From the above results one may conclude that there is quite some ambiguity on the existence of changes in the decay rate/half-life time in β^--decay induced by solar neutrinos. Part of the ambiguity arises from the detection techniques, which in many cases are based on Geiger-Müller detector counting and ionization chamber measurements which are sensitive to environmental conditions and are known to drift. Another drawback is the fact that the variation in solar neutrino flux during the measurements is rather limited at ~3%.

The observations of changing β^--decay rates, which are suggested to be caused by a changing solar neutrino flux, have initiated investigations into indirect methods of detecting antineutrinos such as the work done by de Meijer *et al*. [21] which laid the foundation for the work undertaken in this project.

The aim of this project is to improve on the sensitivity of the measurements performed by de Meijer *et al*. through γ-ray count rate measurements of ^{22}Na at the Koeberg nuclear power plant in South Africa, consisting of two 2.7 GW_{th} reactors where antineutrino flux changes of the order of ~10^{13} $cm^{-2}s^{-1}$ between reactor-off and-on can be achieved at distances of 17 m to 23m from the core of a reactor. Considering that the cross section is dependent (inversely proportional) on the flux of antineutrinos, it is expected that the two orders of magnitude increase in reactor antineutrino flux available at Koeberg should increase the sensitivity and reduce the cross section determined by de Meijer *et al*. by two orders of magnitude to ~10^{-25} cm^2, for ^{22}Na. Also considering that a more efficient $LaBr_3$(Ce) detector and NaI(Tl) well-counter will be used at Koeberg, the counting statistics should increase, depending on the measuring time, thereby increasing the sensitivity further. In conclusion these measurements will be used to assess its potential as a tool to monitor the status of a nuclear reactor while it is expected to improve the sensitivity obtained by de Meijer *et al*. by at least two orders of magnitude for ^{22}Na.

1.2 Scope and outline of the thesis

Chapter 2 provides an introduction to the history of neutrino detection, neutrino properties and the various sources thereof. Concepts of fission and fission applied to the operation of a nuclear reactor leading to the emission of antineutrinos are also discussed. Antineutrino fluxes and energy spectra from a reactor, and their relevance for reactor monitoring are

explained. This project relies on particle detection using scintillation materials; as such interactions of charged and uncharged particles with matter are discussed in Chapter 3. Chapter 4 provides details of the analytical tools used to analyse the data for changes in the decay rate. Chapters 5 to 7 provide details of the three measurements performed at Koeberg, respectively, regarding the experimental set-up and properties of ^{22}Na and the types of detector used. In Chapter 8 concluding remarks are made with a discussion on the ongoing claims of solar neutrinos affecting decay rates. An outlook for future plans regarding antineutrino detection will also be discussed.

CHAPTER 2 Antineutrinos from reactors

2.1 Discovery of neutrinos

Prior to 1930 β^--decay was seen as a two body-decay whereby a parent nucleus decays to a daughter nucleus and an electron [25, 26]. According to the laws of energy conservation the electron would have a well-defined energy, while measurements showed that electrons have a continuum shaped energy spectrum [25, 26]. This apparent violation of energy conservation puzzled physicists, particularly Wolfgang Pauli. He became so desperate to solve the missing energy puzzle, considering all factors he was left to conclude that some energy is carried away by a yet to be detected particle [25]. In 1930 he wrote a letter to colleagues at a conference on radioactivity in Tübingen, Germany [27] wherein he proposed his "desperate remedy". He proposed a particle that was charge neutral and weighed no more than an electron; he called it the neutron (neutral one) [26]. Two years later James Chadwick discovered the neutron and Fermi changed the name of Pauli's ghostlike particle to the neutrino (meaning little neutral one) [25].

This marked the beginning of the search for the neutrino. Physicists had to come up with a theory to explain the existence of the neutrino. By 1934 Enrico Fermi had developed such a theory for β-decay in terms of weak particle interactions [27, 24]. It took more than twenty years for the neutrino to be detected and prove the existence of Pauli's elusive particle.

The neutrino remained elusive until 1956 when Reines and Cowan first detected reactor antineutrinos from the Savannah River nuclear power plant. Their pioneering work utilized 1400 L of cadmium doped liquid scintillator; providing quasi-free protons to interact with the reactor antineutrinos ($\bar{\nu}_e$) via inverse β-decay [24, 26, 27]:

$$\bar{\nu}_e + p \rightarrow e^+ + n. \qquad 2.1$$

During this reaction the $\bar{\nu}_e$ interacts with a free proton (p), resulting in a neutron (n) and a positron (e^+) of which the latter slows down in the scintillator until it annihilates, whereby two E = 511 keV photons are emitted. The time delay between the antineutrino interaction, ionization and the annihilation photons energy deposition is so short that this tri-step process is seen as a single event in the detector; appropriately named the prompt energy deposition. The neutron carries away the remaining energy and is thermalized and absorbed by cadmium.

2.2 Neutrino properties

Neutrinos are fundamental, weakly interacting, electrically neutral particles emitted during weak processes such as β^+-and β^--decay [28]. As such, neutrinos are produced during weak interactions, mediated by the W- and Z-boson [25]. Neutrinos form part of the lepton family consisting of elementary particles; an electron, electron neutrino, muon, muon neutrino, tau and tau neutrino [29]. In the Standard Model each lepton has a corresponding antiparticle or antilepton belonging to one of three flavours; electron, muon or tau. These particles and their corresponding antiparticles have spin ½ and are classified as fermions [29]. In the standard model, particle decays and interactions have to conserve energy, charge end lepton number [28]. Feynman diagrams are commonly used to "visualise" particle interactions or decays. Figure 2.1 illustrates β^+-decay with a Feynman diagram, whereby a proton (p) is transformed into a neutron (n) (one up quark is transformed into a down quark) via the emission of a virtual W^+-boson which subsequently decays into an positron (e^+) and electron aneutrino (ν_e) [26, 27].

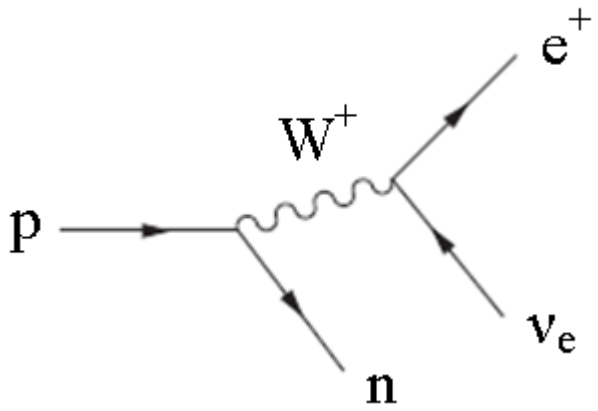

Figure 2.1: *Visual representation of β^+-decay with a Feynman diagram.*

This example of β^+-decay illustrates the conservation laws mentioned above. Table 2.1 provides the charge and lepton number of the particles involved before and after decay as well as the total charge and lepton number before and after decay.

Table 2.1: *Charge and lepton number conservation during β^+-decay.*

Particle	Charge	Lepton number
p	+	0
n	0	0
e^+	+	-1
ν_e	0	+1
Total before	+	0
Total after	+	0

In the Standard Model the wave function of a neutrino obeys the Dirac equation which describes the relativistic behaviour of spin-half particles and allows negative energy solutions interpreted as antiparticles [24, 30]. Also from the solution of the Dirac equation follows the law of conservation of helicity; describing the projection of particle spin on the direction of motion [24, 29]. Experimentally only left handed (spin anti-parallel to momentum) neutrinos and right handed (spin parallel to momentum) antineutrinos have been observed [24, 25, 29, 31]. Another property resulting from the Dirac equation is chirality which, in general is a linear combination of helicity states [25]. In the case of zero mass chirality is the same as helicity [24]. The discovery of neutrino oscillations and therefore mass implies that the Dirac theory of the neutrino does not completely correspond to the experimentally observed properties of the neutrino, consequently, helicity is not conserved [24]. In 1937 Majorana developed a relativistic wave equation for describing neutral particles resulting in a neutrino being its own antiparticle (also in the case of a photon and pion) [24, 30]. The nature of the neutrino has been studied extensively, and continues to be studied (for a recent summary on neutrinoless double β-decay experiments see [32]). Thus far it remains unclear whether neutrinos are Dirac or Majorana particles. Evidence of the Majorana neutrino would be observation of the process of neutrinoless double β-decay:

$$(A,Z) \rightarrow (A,Z+2) + 2e^-, \tag{2.2}$$

whereby it is energetically favourable for an even-even nucleus to decay via two consecutive β-decays without emitting antineutrinos. This process is not allowed for Dirac neutrinos since it violates lepton number conservation, though it is allowed for Majorana neutrinos and can be seen as two subsequent steps [24]:

$$(Z,A) \rightarrow (Z+1,A) + e^- + \bar{\nu}_e$$

$$(Z+1,A) + \nu_e \rightarrow (Z+2,A) + e^-, \tag{2.3}$$

if neutrinos and antineutrinos are the same particles. Thus far only "normal" double β-decay (simultaneous β-decay of two neutrons with emission of two antineutrinos) has been identified in thirty six even-even nuclei where typical half-lives are of the order of $t_{1/2} \approx 10^{20}$ y [24]. Double beta-decay is an extremely rare process and consequently so too is neutrinoless double-beta-decay if it is real. More specifically, neutrinoless double β^+-decay/EC is even harder to detect, see [33, 34] for details.

Neutrinos were thought to be massless particles according to the Standard Model, until the discovery of neutrino oscillations in 1998 using the SuperKamiokande detector which detected atmospheric neutrinos resulting from the interaction of cosmic rays. [28, 35]. Neutrino oscillations imply that neutrinos oscillate between three flavours as they propagate, indicating that they have non-zero mass [25] and that the three neutrino flavour eigenstates are superpositions of the three neutrino mass eigenstates. The mass difference causes each state to propagate at a different frequency, since in quantum mechanics the wavelength of a particle depends on its speed and mass, leading to a mixture or interference of the states [25, 36]. Therefore a neutrino can transform into different flavours as it propagates. The discovery of neutrino oscillations also solved the solar neutrino problem whereby the measured solar neutrino flux was approximately half of the flux predicted by solar models [29].

Since energy must be conserved, the neutrino mass can in principle be inferred from the maximum energy of electrons following β^--decay, though the electron energy measurement depends on the energy resolution of the detector. The most accurate measurement of the neutrino mass has been achieved with β^--decay of tritium (^{3}H) for which the electron antineutrino mass has been constrained to be $0 \leq m_{\bar{\upsilon}_e} \leq 4 \times 10^{-6}\, m_e = 2$ eV [25]. For two-flavour mixing, the probability that a neutrino flavour x oscillates into a flavour y in vacuum is given by:

$$P(\upsilon_x \rightarrow \upsilon_y) = \sin^2 2\theta_{12} \sin^2\left(\frac{1.27\Delta m^2 L}{E}\right), \tag{2.4}$$

where the mass squared difference is

$$\Delta m^2 = \left|m_1^2 - m_2^2\right|, \tag{2.5}$$

θ_{12} is the so called mixing angle between the mass eigenstates, L is the neutrino source-detector distance (the so called baseline) and E is the neutrino energy [25, 35]. The mixing angle θ_{ij} is a measure on the relative mixing between the mass states i and j in the different flavour states [37]. Equation 2.4 shows that the probability for oscillations will be greatest when $\theta_{12} = \pi/4$ and $L=\frac{E\pi}{2(1.27)\Delta m^2}$. The oscillations vanish if the mixing angle is zero or if the neutrinos have equal mass. Oscillations also do not occur if the mass eigenstates are zero. The term $\sin^2 2\theta_{12}$ describes the amplitude of the oscillation while Δm^2 determines the oscillation length. Three-flavour mixing becomes more complicated. The parameters θ_{12} and Δm^2 can be obtained from measurements using different baselines [38]. Neutrino propagation in matter is influenced by what is known as the Mikheyev–Smirnov–Wolfenstein effect (MSW). The MSW effect is the effect of transformation of one neutrino species (flavour) into another one in a medium with varying density [39]. Essentially neutrino oscillation is enhanced, depending on the neutrino energy and properties of the medium through neutrino scattering on electrons, protons and neutrons [24, 39]. Reactor anti-neutrino (electron antineutrino) oscillations have been reported at baselines ranging from tens of meters to hundreds of kilometers. The KamLAND detector in Japan showed a reactor antineutrino oscillation signal at an average baseline of 180 km from surrounding nuclear reactors [40, 41]. The RENO and DAYA BAY experiments observed reactor antineutrino oscillations at baselines of 1383 m [40] and 1648 m [43], respectively. The claimed improvement on the reactor antineutrino flux calculation by Mention *et al.* lead to deficits in the antineutrino flux previously measured at ILL-Grenoble, Goesgen, Rovno, Krasnoyarsk, Savannah River and Bugey at baselines < 100 m [44]. Figures 2.2 and 2.3 respectively show the ratio of the observed antineutrino flux to the calculated expected flux as a function of distance to the respective reactors at ILL-Grenoble, Goesgen, Rovno, Krasnoyarsk, Savannah River and Bugey before [40] and after [44] the recalculation of antineutrino flux. Indicated by the solid blue line is the mean of the ratios.

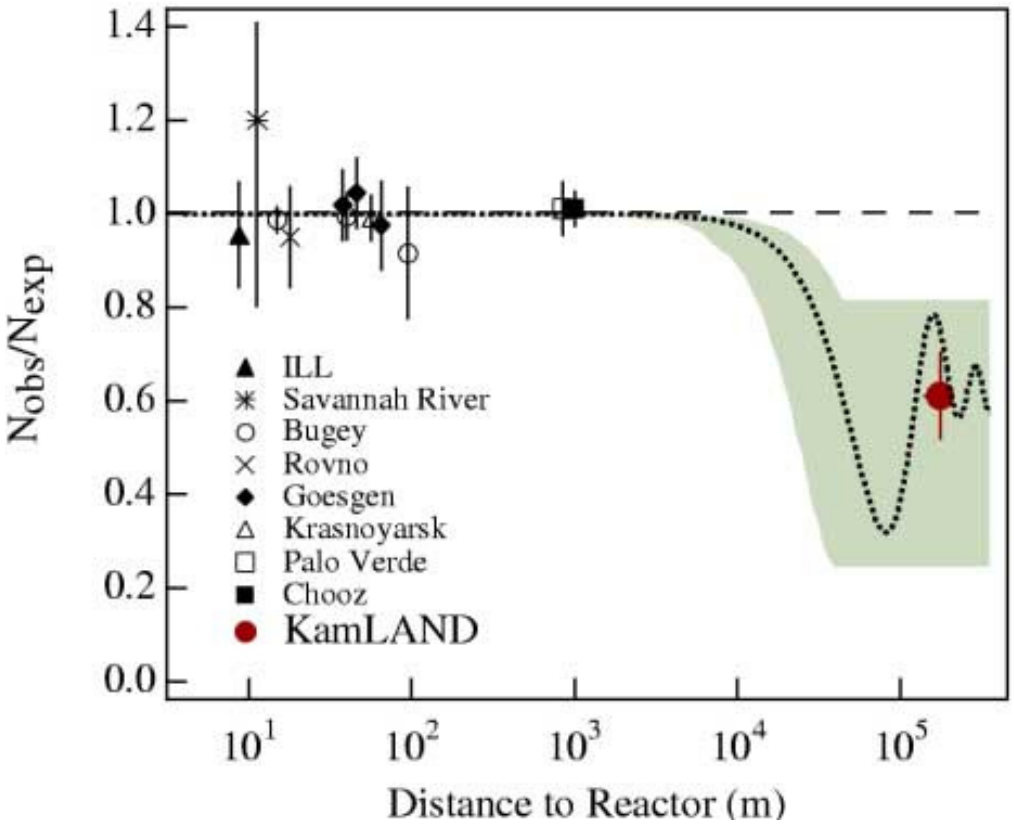

Figure 2.2: *Ratio of the observed antineutrino flux to the calculated, expected flux as a function of distance to the respective reactors at ILL-Grenoble, Goesgen, Rovno, Krasnoyarsk, Savannah River, Bugey and KamLAND before reactor antineutrino flux recalculation [40]. The dashed line indicates the case of no neutrino oscillations. The dotted line indicates the neutrino mixing case for* $\sin^2 2\theta = 0.833$ *and* $\Delta m^2 = 5.5\times10^{-5}\ eV^2$ *which represents a best-fit large mixing angle (LMA) prediction [40].*

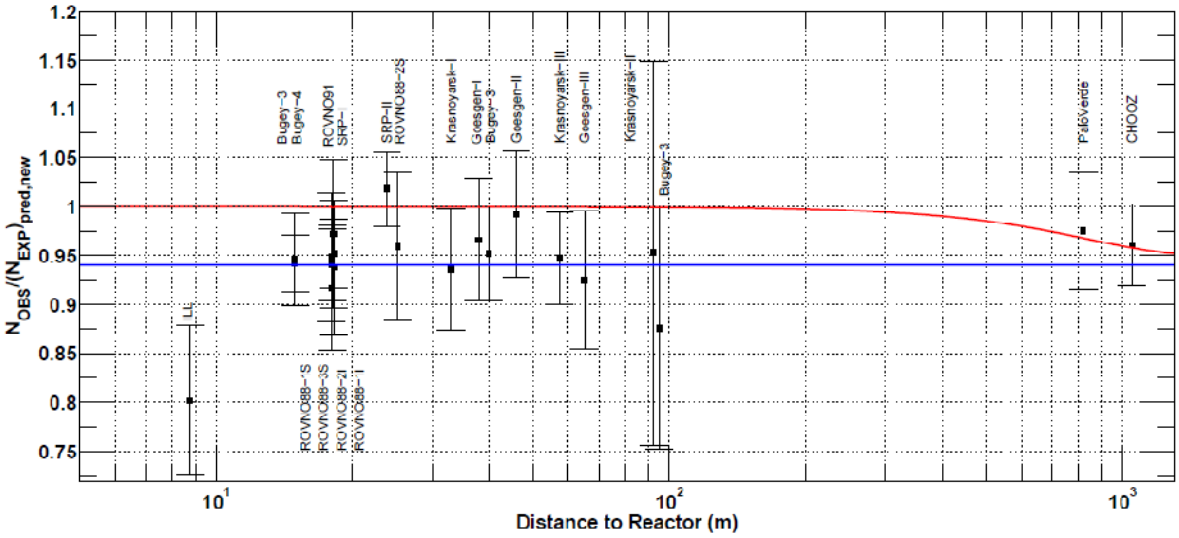

Figure 2.3: *Ratio of the observed antineutrino flux to the calculated, expected flux as a function of distance to the respective reactors at ILL-Grenoble, Goesgen, Rovno, Krasnoyarsk, Savannah River, Bugey and KamLAND [44]. Indicated by the solid blue line is the mean of the ratios [44]. The red line indicates the neutrino mixing case for* $\sin^2 2\theta_{13} = 0.06$ *[44].*

Figure 2.3 shows an average 5.7% deficit in the expected antineutrino flux and is consistent with being independent of the distance to the reactor at distances $\gtrsim$ 15 m [44]. This result is known as "The reactor antineutrino anomaly" where the deficit in the observed reactor antineutrino flux is explained through reactor antineutrino oscillation into a hypothesized fourth, non-standard neutrino [44]. This hypothesis remains to be proven. Therefore, in this work it is assumed that reactor antineutrinos do not oscillate over the short reactor-to-detector distances < 25 m.

2.3 Natural neutrino sources

Solar (electron) neutrinos are emitted during fusion processes inside the Sun with a flux of approximately $\varphi_\nu \approx 10^{10}$ $cm^{-2}s^{-1}$ [45], with energy ranging between $0 < E_\nu \leq 18.8$ MeV. Neutrinos of all flavours are emitted after the core collapse explosion of a massive star after it has exhausted its nuclear fuel [46]. Thus far the strongest upper limit for the supernova relic electron neutrino flux has been measured by Super Kamiokande as $\varphi_\nu \approx 1.2$ $cm^{-2}s^{-1}$ at a 90% confidence level for $E_\nu > 19.3$ MeV [47]. Cosmic neutrinos are also produced by pion decay through cosmic-ray interactions within the galactic disc [24]. It is also theorised in the standard Big Bang model that a cosmological relic low-energy neutrino background exists which can provide information on the Universe earlier than 300 000 years after the Big Bang,

which the Cosmic Microwave Background cannot provide [48, 49]. When high-energy cosmic rays consisting of 98% protons and heavier nuclei and 2% electrons [24, 50], reaching energies up to E ~ 10^{20} eV [51], collide with atoms in the Earth's atmosphere at approximately 15 km altitude, cascades of particles consisting of photons, neutrons, protons, pions, kaons, electrons, positrons, muons and neutrinos are emitted [52]. The main contribution to the flux of atmospheric neutrinos comes from the decay of pions, kaons and muons:

$$\pi^+ \rightarrow \mu^+ + \nu_\mu, \tag{2.6}$$

$$\pi^- \rightarrow \mu^- + \bar{\nu}_\mu, \tag{2.7}$$

$$K^- \rightarrow \mu^- + \bar{\nu}_\mu, \tag{2.8}$$

$$K^+ \rightarrow \mu^+ + \nu_\mu \tag{2.9}$$

$$\mu^+ \rightarrow e^+ + \nu_e + \bar{\nu}_\mu, \tag{2.10}$$

$$\mu^- \rightarrow e^- + \bar{\nu}_e + \nu_\mu. \tag{2.11}$$

Travelling at the speed of light and interacting weakly, muons can reach sea-level before decaying or losing completely their energy. As such it is possible for muons to interact inside a detector via ionisation, giving rise to energy deposition in a detector at ground level which contributes to an energy spectrum. The flux of muons at sea-level is approximately $\varphi_\mu \approx 0.017$ cm^{-2} s^{-1} [50] with energy depending on the energy of the primary cosmic radiation [24, 50].

According to the Bulk Silicate Earth (BSE) model consisting of crust and mantel, 99% of the radiogenic heat power of the Earth comes from the energy released during β^--decay of ^{238}U, ^{232}Th and ^{40}K [53, 54]. During β^--decay of these radionuclei:

$$(Z,A) \rightarrow (Z+1,A) + e^- + \bar{\nu}_e, \tag{2.12}$$

electron antineutrinos, known as geoneutrinos are emitted isotropically. A rough estimate of the geoneutrino flux at the surface of the Earth can be made by considering the BSE as a point source with a mass of $M_{BSE} = 4.05 \times 10^{24}$ kg [55] and calculating the mass contributions and subsequent number of atoms of ^{238}U, ^{232}Th and ^{40}K. The total mass M_j of radionuclide j (j = ^{238}U, ^{232}Th and ^{40}K) is determined by the total amount C_k of k = U, Th and

K in the Earth (in kg/kg soil) multiplied by the isotopic abundance C_j of radionuclide j, multiplied by M_{BSE}:

$$M_j = C_k \times C_j \times M_{BSE}. \tag{2.13}$$

The number of atoms N_j of radionuclide j is determined by the total mass of radionuclide j divided by its molecular mass M_{mol}:

$$N_j = \frac{M_j}{M_{mol}(j)}. \tag{2.14}$$

Now the activity A_j of radionuclide j can be determined by:

$$A_j = \lambda_j N_j, \tag{2.15}$$

where λ_j is the decay constant of radionuclide j. Assuming the BSE as a point source located at the center of the Earth, the flux of geoneutrinos $\varphi_{\bar{\nu}_e}(j)$ at the surface of the Earth due to radionuclide j can now be calculated by:

$$\varphi_{\bar{\nu}_e}(j) = \frac{N(\bar{\nu}_e)A_j}{4\pi r^2}, \tag{2.16}$$

where r is the distance from the Earth center to surface ($\approx 10^6$ m) and $N(\bar{\nu}_e)$ is the total number of antineutrinos emitted in the decay chain of radionuclide j. Table 2.2 provides the derived values, after applying equations 2.13 to 2.16, used to estimate the total geoneutrino flux at the surface of the Earth according to the BSE model.

Table 2.2: *Estimated geoneutrino flux at the surface of the Earth caused by β^--decay of the radionuclei ^{235}U, ^{238}U, ^{232}Th and ^{40}K using abundances predicted by the BSE model [54, 55, 56].*

	U		Th	K
Natural abundance C_k ($\times 10^{-6}$ kg/kg soil)	0.02		0.08	240
	^{235}U	^{238}U	^{232}Th	^{40}K
Isotopic abundance C_j	0.0072	0.9927	1.0	0.000117
Mass ($\times 10^{17}$ kg)	0.006	0.8	3.2	1.1
M_{mol} ($\times 1.67 \times 10^{-27}$ kg)	235	238	232	40
N ($\times 10^{41}$)	0.015	2.0	8.4	17.0
λ ($\times 10^{-18}$ s^{-1})	31.2	4.9	1.6	17.2
A ($\times 10^{24}$ s^{-1})	0.04	0.99	1.31	29.21
$N(\bar{\nu}_e)$	4	6	4	1
$\varphi_{\bar{\nu}_e}$ ($\times 10^6 cm^{-2}s^{-1}$)	0.04	1.2	1.0	5.7

The estimated geoneutrino fluxes in Table 2.2 add up to a total geoneutrino flux of $\varphi_{\bar{\nu}_e} = 8.0 \times 10^6$ $cm^{-2}s^{-1}$ which is of the same order of magnitude of geoneutrino fluxes provided in Ref. [55, 56, 57]. Table 2.2 also indicates that approximately 70% of the total geoneutrino flux is provided by ^{40}K, though only the geoneutrinos from ^{238}U and ^{232}Th have energy above the 1.806 MeV threshold for inverse β^+-decay on a free proton to allow detection. ^{238}U and ^{232}Th are constituents of nuclear fission reactors, therefore detecting geoneutrinos emitted during fission could serve as a method to locate natural nuclear reactors inside the Earth, called georeactors, as well as map radiogenic heat sources. Geoneutrinos originating from various elements can be distinguished by their different energy spectra, i.e. geoneutrinos with energy E > 2.25 MeV are only released in the ^{238}U decay chain. In Figure 2.4 it is shown how geoneutrinos from ^{238}U, ^{235}U, ^{232}Th and ^{40}K can be distinguished by their different energy spectra [56, 57].

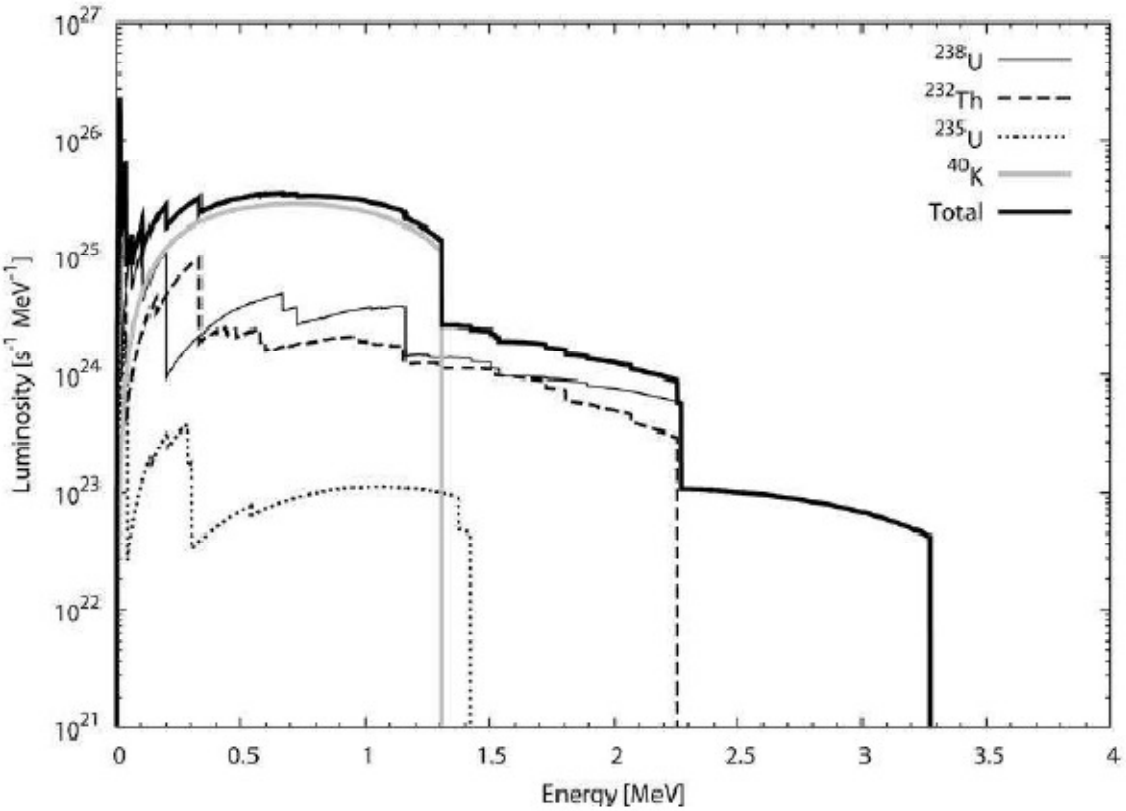

Figure 2.4: *Geoneutrino spectra from ^{235}U, ^{238}U, ^{232}Th and ^{40}K [55, 57].*

2.4 Artificial neutrino sources

All the previously mentioned sources of neutrinos and antineutrinos are natural sources, though anthropogenic sources do exist. Neutrino/Antineutrino beams are produced by particle accelerators by impinging high energy protons onto fixed targets (typically graphite or beryllium), releasing secondary charged particles of pions and kaons which can be separated and focused by magnets and decay according to equations 2.6 to 2.11 resulting in mu neutrinos or –antineutrinos [24]. Neutrino beams are convenient to use for various investigations of neutrino properties such as neutrino oscillations, neutrino interactions with various nuclei, differences between neutrinos and antineutrinos and detection of new particles.

2.4.1 Reactor antineutrinos

The largest source of artificially produced antineutrinos is nuclear reactors. Nuclear power accounts for 12.9% of the world's total electricity production with an ever increasing demand [58]. According to the IAEA database on nuclear power reactors, as of 08 January 2014, there

are 437 operational nuclear reactors worldwide and 72 more under construction [59]. Of course nuclear power has its proponents and opponents, the details of which will not be discussed here. Instead, one of the potentially most serious consequences of nuclear power will be addressed; the proliferation of nuclear weapons through diversion of fissile material from reactors into nuclear weapons programmes. The IAEA has placed the monitoring of reactors for illicit operation at the top of its agenda in terms of safeguards. Current methods of reactor monitoring take place in the form of real-time surveillance video, reports/feedback and neutron and γ-ray measurements during on-site inspections by IAEA officials. The IAEA may also monitor uranium mines, fuel fabrication and enrichment plants, and nuclear waste sites as well as any other location where nuclear material is or may be present as long as it forms part of the IAEA Non-Proliferation Treaty (NPT) signed by member states. Non-member states and nuclear facilities not bound by the NPT do not have to comply with safeguard measures and can refuse IAEA inspections. Such facilities provoke suspicion, therefore the IAEA want to adopt safeguard measures that will allow them to monitor nuclear facilities off-site. More specifically it is desired to monitor the fuel evolution in nuclear reactors remotely. The feasibility of reactor monitoring with antineutrinos has been demonstrated by the ROVNO group as well as N.S. Bowden and collaborators using the SONGS detectors [60, 61, 62].

During the past ten years great efforts have gone into developing antineutrino detectors for reactor monitoring in terms of the size of the detectors used. The size of the detectors using inverse β-decay to detect antineutrinos, as described in Chapter 1, is of the order of tons due to the very low interaction cross section of antineutrinos with matter.

Nuclear reactors work on the principle of a sustained, controlled fission chain reaction. Fission is the splitting of an unstable nucleus into two lighter, often unstable, daughter nuclides called fission fragments accompanied by the emission of a few neutrons and γ-rays [63]. The fission process can be understood qualitatively through a charged liquid drop model of a nucleus whereby its stability is determined by competition between the strong short ranged attractive nuclear force which holds the nucleus together and the longer ranged repulsive Coulomb force between the protons [25, 29, 63].

According to the Semi-Empirical Mass Formula (SEMF):

$$M(A,Z) = NM_n + ZM_p + Zm_e - a_vA + a_sA^{2/3} + a_c\frac{Z^2}{A^{1/3}} + a_a\frac{(N-Z)^2}{4A} + \frac{\delta}{A^{1/2}}, \quad (2.17)$$

where $N = A - Z$ and

a_vA is known as the volume term,

$a_sA^{2/3}$ is known as the surface term,

$a_c\frac{Z^2}{A^{1/3}}$ is known as the Coulomb term,

$a_a\frac{(N-Z)^2}{4A}$ is known as the asymmetry term and

$\frac{\delta}{A^{1/2}}$ is known as the pairing term, when a nucleus is perturbed the surface energy will increase and the Coulomb energy will decrease [25, 29]. The following parameterization of a deformed nucleus can be found in most introductory nuclear and particle physics handbooks [25, 29]. The spherical shape of the incompressible (constant volume V) liquid drop can be deformed into an ellipsoid with axis $a = R(1 + \varepsilon)$ and $b = R(1 - \frac{\varepsilon}{2})$ so that $V = \frac{4}{3}\pi R^3 = \frac{4}{3}\pi ab^2$. The surface of an ellipsoid is then expanded in terms of a and b in a power series of the perturbation ε leading to the surface energy term having the form:

$$E_s = a_sA^{2/3}\left(1 + \frac{2}{5}\varepsilon^2 + \ldots\right) \quad (2.18)$$

and Coulomb energy term:

$$E_c = a_cZ^2A^{-1/3}\left(1 - \frac{1}{5}\varepsilon^2 + \ldots\right). \quad (2.19)$$

Thus a perturbation ε changes the total energy by:

$$\Delta E = (E_s - E_c) - (E_s - E_c)_{SEMF} = \frac{\varepsilon^2}{5}\left(2a_sA^{2/3} - a_cZ^2A^{-1/3}\right). \quad (2.20)$$

The deformation is energetically favourable when $\Delta E < 0$, then fission can occur. This condition results in:

$$\frac{Z^2}{A} \geq \frac{2a}{a_c} \approx 49, \tag{2.21}$$

which is satisfied by $Z > 116$ and $A \geq 270$ for which spontaneous fission can occur. There are approximately 100 nuclei that are known to fission spontaneously such as ^{252}Cf and ^{250}Cm.

Figure 2.5 shows schematic of the fission process relative to the potential energy V(r) of the nucleus during different phases of the fission process [1]. The solid line represents the potential of the parent nucleus, at distances above the saddle point R (where the nuclear and Coulomb forces are in balance), the potential varies as approximately $\frac{1}{r}$ and the deformed nucleus experiences a stronger internal repulsion due to the Coulomb repulsion of the two "lobes" such that the "lobes" rupture and form daughter nuclei.

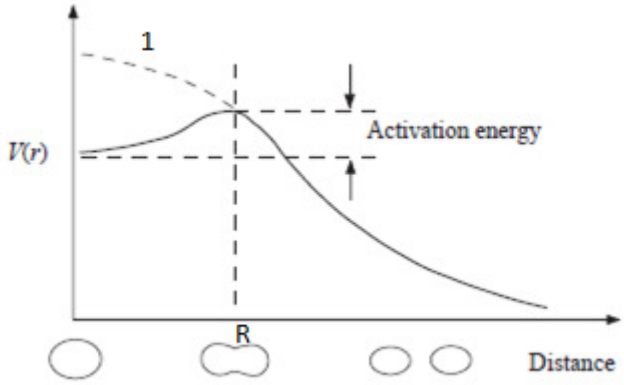

Figure 2.5: *Schematic of the fission process as a function of the potential of a nucleus experiencing a perturbation [25].*

The potential at R represents a fission barrier which a nucleus has to overcome for it to fission. The energy needed for a nucleus to overcome the fission barrier is known as the activation energy, indicated in Figure 2.5. Though in principle many heavy nuclei can fission by quantum-mechanical tunnelling, the probability for this is so small that for most nuclei it is never observed. For nuclei with $\frac{Z^2}{A} \gtrsim 49$ the fission barrier disappears and the potential follows the dashed line indicated by the number 1 in Figure 2.5. In a nuclear reactor the above mentioned perturbation is provided by neutrons, though the resulting reaction depends

on the energy of the incident neutron. Generally neutrons are classified according to their kinetic energy, shown in Table 2.3 [26].

Table 2.3: *Classification of neutrons according to kinetic energy [26].*

Category	Energy
Cold neutrons	< 0.003 eV
Slow (thermal) neutrons	0.003 – 0.4 eV
Slow (epithermal) neutrons	0.4 – 100 eV
Intermediate neutrons	100 eV– 200 keV
Fast neutrons	200 keV – 10 MeV
High energy (relativistic) neutrons	> 10 MeV

A neutron incident on a nucleus can either be scattered or absorbed, the probability of which is described by the interaction cross section σ of each reaction measures in barns (1 barn = 10^{-24} cm^2). The total interaction cross section σ_t is determined by the sum of the scattering σ_s and absorption σ_a cross sections [63]:

$$\sigma_t = \sigma_s + \sigma_a. \tag{2.22}$$

Further, neutron scattering can either be elastic or inelastic, where in the case of the former, momentum and kinetic energy is conserved, while during inelastic scattering only momentum is conserved and the nucleus is promoted to an excited state which will de-excite by emitting one or more γ-rays [63]. The scattering cross section can then be expressed as the sum of the cross section for elastic σ_n and inelastic $\sigma_{n'}$ scattering [63]

$$\sigma_s = \sigma_n + \sigma_{n'}. \tag{2.23}$$

For nuclei that are fissionable, the incident neutron could either be captured leaving the nucleus in an excited state which will decay by γ-ray emission or the neutron could induce fission. In both cases though the daughter nuclei are usually unstable and will decay toward the line of stability. The absorption cross section can then be expressed as the sum of the cross section for capture σ_γ and fission σ_f:

$$\sigma_a = \sigma_\gamma + \sigma_f. \tag{2.24}$$

Though several types of reactors are available, only the applicable reactor type to this work is considered. The reactors at the Koeberg nuclear power station are called thermal Pressurized Water Reactors (PWR) where reactor fuel consists of enriched uranium. Natural uranium consists of 0.07% ^{235}U and 99.3% ^{238}U. Both ^{235}U and ^{238}U are fissionable nuclei also called *fertile* material, meaning that fission can be induced. Nuclei that can also undergo fission spontaneously are called *fissile* material, such as ^{235}U. For fission to be induced in fertile material a neutron with energy at least equal to the activation energy has to be absorbed, resulting in the nucleus being excited to above the fission barrier. From the shell model the activation energy of ^{235}U has been determined to be $E_{ac}(^{235}U) = 6.2$ MeV. When a neutron with negligible energy is absorbed by ^{235}U:

$$^{235}U + n \rightarrow {}^{236}U^{*}, \tag{2.25}$$

the excitation energy E_{ex} of the compound nucleus $^{236}U^{*}$ above its ground state will be equal to the binding energy of the neutron in that state and can be determined from the energy equivalent of the atomic masses [25, 29]:

$$E_{ex}(^{236}U^{*}) = \left[m\left(^{236}U^{*}\right) - m\left(^{236}U\right)\right]c^{2}, \tag{2.26}$$

where

$$m\left(^{236}U^{*}\right) = m\left(^{235}U\right) + m_{n} = 235.043924\ u + 1.008665\ u = 236.052589\ u \tag{2.27}$$

and m_n is the mass of a neutron in u, and 1 u =931.494061 MeV/c^2 leading to an excitation energy:

$$E_{ex}(^{236}U^{*}) = (236.052589\ u - 236.045563u) \times 931.494061\ MeVu^{-1} = 6.5\ MeV. \tag{2.28}$$

Therefore the excitation energy of $^{236}U^{*}$ is larger than the activation energy of ^{236}U and the fission barrier can in principle be exceeded by absorption of zero energy neutrons.

Applying a similar calculation to ^{238}U leads to an excitation energy for $^{239}U^{*}$ of $E_{ex}(^{239}U^{*}) = 4.8$ MeV where as its ground state activation energy is $E_{ac}(^{239}U) = 6.6$ MeV, therefore a neutron with energy $E_n \gtrsim 1.8$ MeV has to be absorbed to overcome the fission barrier. From this exercise it can be concluded that the probability for induced fission depends on the kinetic energy of the absorbed neutron, more specifically expressed in terms of the fission cross section σ_f. Moreover, cross sections increase greatly if a neutron causes an excitation,

corresponding to a specific quantum state in the compound nucleus, known as a resonance state [63, 64]. As an example Figure 2.6 shows the fission cross section of ^{235}U and ^{238}U as a function of neutron energy, where the resonance peaks related to ^{235}U are visible as sharp spikes in the epithermal neutron region. The fission cross section of ^{235}U increases even further below the epithermal region and decreases above the resonance peaks. Also shown is the poor fission cross section of ^{238}U below $E_n \approx 1$ MeV after which the fission cross section increases in the fast neutron region.

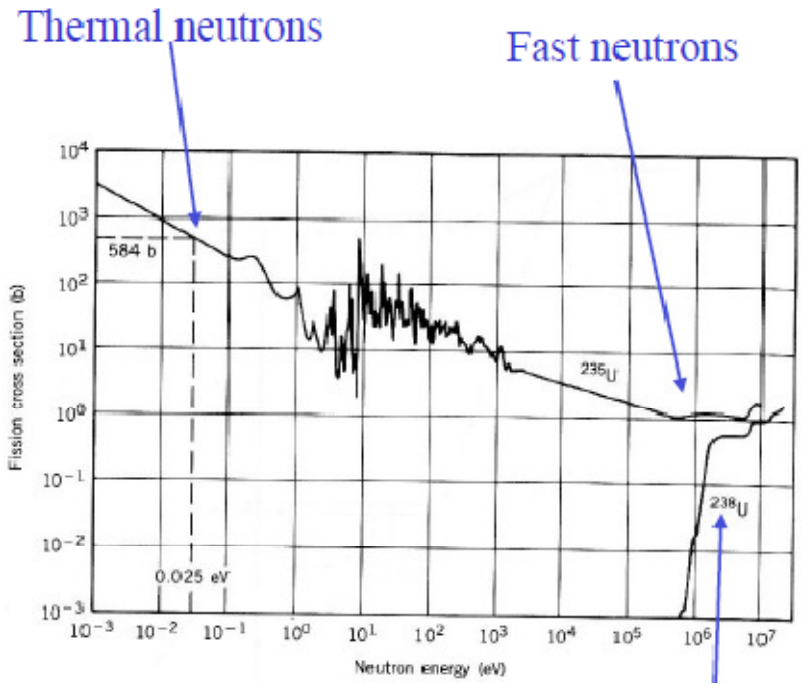

Figure 2.6: *Fission cross sections of ^{235}U and ^{238}U as a function of neutron energy, also shown are the resonance peaks of ^{235}U, visible as sharp spikes.*

Each fission releases an average number of neutrons, not all of the same energy. For a chain reaction to occur the emitted neutrons have to feed the next generation of fission which is dependent on the neutron energy.

The criticality factor k describes the conditions required for a sustained chain reaction [25]:

$$k = \frac{\text{number of neutrons produced in the } (n+1)^{th} \text{ stage of fission}}{\text{number of neutrons produced in the } n^{th} \text{ stage of fission}}. \qquad (2.29)$$

When $k \approx 1$ the reactor is in a state called critical during which a sustained and controlled chain reaction is possible. When $k < 1$ the reactor is termed subcritical during which the

reaction will terminate. When k > 1 the reactor is termed supercritical and an accelerated chain reaction will occur during which the released energy continues to increase and could cause an explosion. On average the fission of a ^{235}U nucleus releases approximately 2.5 fast neutrons with energy $E_n \approx 2$ MeV [25, 64]. In naturally occurring uranium the neutrons will gradually lose energy as they scatter off the heavy uranium nuclei until they are absorbed in the neutron capture resonance peaks of ^{238}U between 10 eV < E_n < 100 eV for which the capture cross section of ^{238}U is greater than the fission cross section of ^{235}U, shown in Figure 2.7. Though ^{238}U can fission with fast neutrons, its fission only produces more fast neutrons.

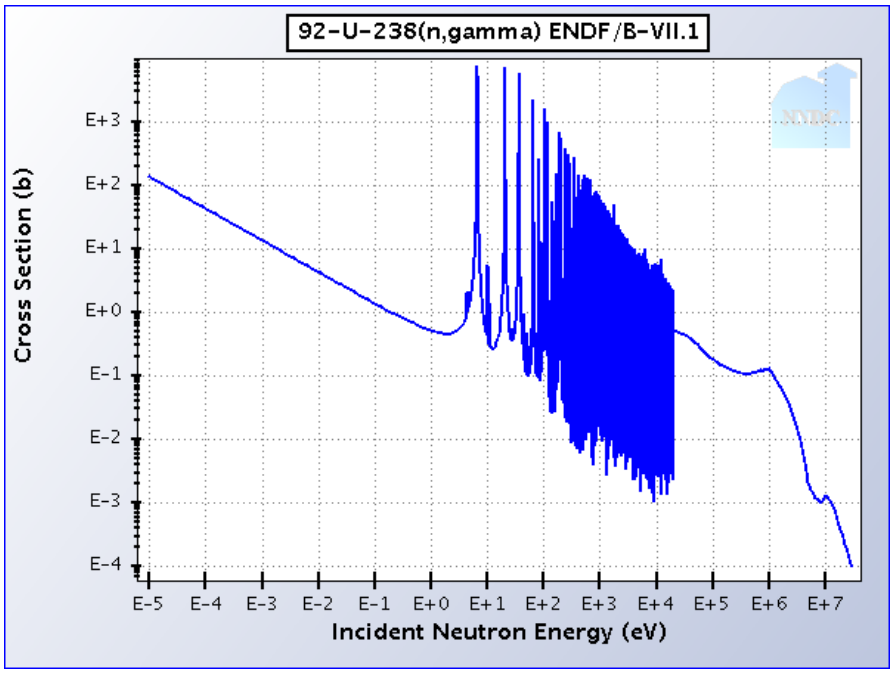

Figure 2.7: *Neutron capture resonance peaks of ^{238}U [1].*

Therefore the criticality factor is k < 1 and the next generation of fission will not occur in naturally occuring uranium. To overcome this in a reactor, a neutron moderator (usually heavy water, D_2O) is used to slow the neutrons down (thermalise) quickly enough via elastic scattering without being absorbed in the resonance peaks allowing them to be absorbed by ^{235}U to induce the next generation of fission [25]. Another solution is to increase the amount of ^{235}U relative to ^{238}U in the fuel in a process called enrichment. Commercial reactors typically use 3 – 5% enriched uranium. Usually the criticality factor is controlled by a combination of neutron moderators, uranium enrichment and also the geometry of the fuel assembly and reactor vessel. The criticality factor can also be controlled by inserting or removing control rods from the core, that have a large neutron absorption cross section and include elements such as boron, cadmium or hafnium [63]. Usually the neutron moderator is

doped with boric acid due to the high thermal neutron absorption cross section of ^{10}B, $\sigma_a(^{10}B)$ = 3840 barns [65], thus boron is also called a neutron poison of which the concentration can be controlled as desired. The number of neutrons released after each fission is known as fission neutrons and occurs almost immediately (called prompt neutrons), though approximately 1% of fission neutrons are delayed due to de-excitation of the fission fragments [63].

Thus far only ^{235}U and ^{238}U fission processes have been discussed in terms of fission cross sections, but the fission cross section σ_f only accounts for one part comprising the absorption cross section σ_a in equation 2.31. At least one thermal neutron is required to sustain a chain reaction, since more than one neutron is released per fission of ^{235}U, therefore one of the other neutrons could be used to convert fertile material to fissile material through neutron capture by ^{238}U leading to ^{239}U which decays to ^{239}Pu after a chain of successive β^--decays [63]:

$$n + {}^{238}_{92}U \rightarrow {}^{239}_{92}U \rightarrow {}^{239}_{93}Np \rightarrow {}^{239}_{94}Pu, \tag{2.30}$$

which is also a fissile isotope. If a reactor produces more fissile material than it consumes it is called a breeder reactor. This type of reactor is proposed to exist at the Earth's core-mantle boundary [66]. If ^{239}Pu captures a neutron it will become ^{240}Pu which in turn can also capture a neutron to become ^{241}Pu which is also a fissile isotope. Fissile materials are a concern for proliferation of nuclear weapons.

Each fission releases energy of approximately $E \approx 200$ MeV which heats the primary coolant inside the reactor vessel. Approximately 85% of the energy released comes in the form of the kinetic energy of the two fission fragments, the remaining energy is shared amongst the neutrons, γ-rays emitted during de-excitation of the fragments and also γ-rays, β-particles and electron antineutrinos emitted during β^- -decay of the fission products [63]. The electron antineutrinos escape the reactor and do not contribute to the heating of the primary coolant (also serving as a neutron moderator). To prevent the primary coolant from boiling, the reactor vessel is kept under pressure of 152 bar [63]. The primary coolant circulates through a steam generator kept at lower pressure to allow water fed to the steam generator to boil after heat transfer from the primary coolant. The primary coolant is pumped back into the core and the resulting steam is passed to a turbine which drives an electrical generator. This process and components are shown in Figure 2.8.

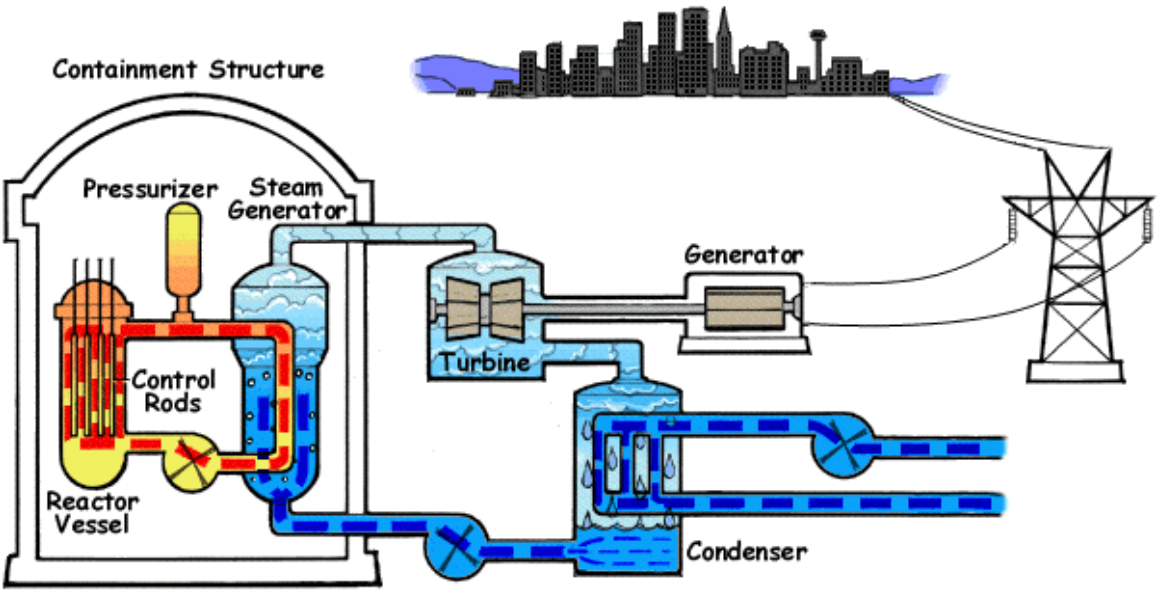

Figure 2.8: *Schematic of the components of a nuclear power station [67].*

2.4.2 Implications of fission for reactor antineutrinos

Figure 2.9 shows the many possible pairs of fission fragments that could result from thermal neutron fission of ^{235}U in terms of a mass frequency distribution of the fragments [63].

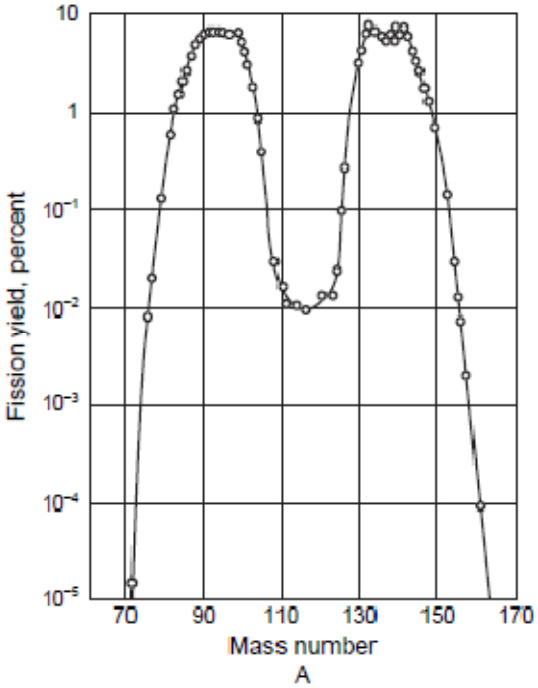

Figure 2.9: *Mass frequency distribution of the fission fragments resulting from thermal neutron fission of ^{235}U [63].*

The shape of the fragment-mass distribution shows two distinct groups. This shape is typical of fission fragments resulting from thermal neutron fission [63]. Usually the decay of the unstable neutron rich fission fragments proceeds toward the line of stability through more than one β^--decay respectively. Therefore, considering that one pair out of more than 40 pairs of fission fragments is produced per fission, leading to more than a thousand decay branches, calculating the antineutrino spectrum using first principles becomes a complex and challenging problem [68, 69]. Reactor antineutrinos with energy ranging from zero to approximately E = 15 MeV are mainly produced by β^--decay of the fission products of ^{235}U, ^{238}U, ^{239}Pu and ^{241}Pu. Only antineutrinos with energy above the E = 1.8 MeV threshold for inverse β^+-decay can be detected. Per fission, the total energy released, the energy of the antineutrinos and the number of antineutrinos emitted, depend on the specific isotope and fission products. The most accurate antineutrino fluxes from ^{235}U, ^{239}P and ^{241}Pu were obtained at the Institut Laue-Langevin in the 1980s by inverting the measured β^--spectra of fission [69, 70]. No measured β^--spectra resulting from ^{238}U fission are available since fission is only induced by fast neutrons, therefore the antineutrino spectrum has to be calculated theoretically [69, 70]. Table 2.4 provides the average number of neutrons as well as antineutrinos released per fission of ^{235}U, ^{238}U, ^{239}Pu and ^{241}Pu.

Table 2.4: *Average number of neutrons and antineutrinos released per fission of ^{235}U, ^{238}U, ^{239}Pu and ^{241}Pu [67, 68].*

Isotope	n/fission	$\bar{\nu}_e$/fission
^{235}U	2.5	5.58
^{238}U	1.7	6.69
^{239}Pu	2.9	5.09
^{241}Pu	3.0	5.89

From this group the two major fissile isotopes in a reactor (as well as a nuclear weapon) are ^{235}U and ^{239}Pu for which the average number of antineutrinos above the E = 1.8 MeV threshold for detection via inverse β^+-decay is 1.92 and 1.45, respectively [61, 71]. During a reactor fuel cycle the isotopic mass contributions change; while ^{235}U is being consumed, ^{239}Pu is produced and the fission rates change, therefore the antineutrino flux from ^{235}U fission decreases, while the antineutrino flux from ^{239}Pu fission increases [61, 72], this is known as the burn-up effect [61, 72]. The antineutrino flux is directly related to the isotopic content of the core and the key for monitoring the fissile inventory lies in discriminating

between the antineutrino flux and energy from ^{235}U and ^{239}Pu fission by measuring the respective antineutrino energy spectra. Figure 2.10 shows the calculated change in fuel composition in a PWR with 2.7 % enriched ^{235}U, in terms of the percentage of the total number of fissions during a three year fuel cycle corresponding to 30 GigaWatt-days per metric ton of ingoing uranium [73].

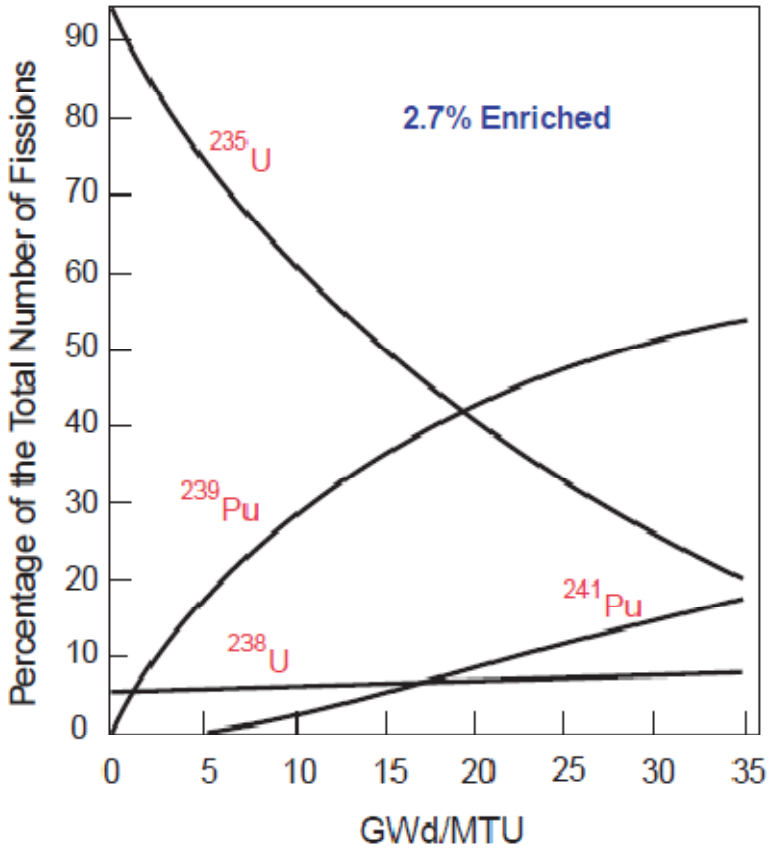

Figure 2.10: *Change in fuel composition of a PWR enriched to 2.7 % ^{235}U during a three year cycle [73].*

From Figure 2.10 it is observed that the fission rate from ^{238}U remains approximately constant while the fission rate from of ^{235}U decreases and the fission rate from ^{239}Pu increases. ^{241}Pu is also produced after two successive neutron captures by ^{239}Pu. Since the antineutrino flux is coupled to the fission rate, as ^{239}Pu accumulates and becomes the dominant contribution to the fission rate, the total antineutrino flux decreases.

Figure 2.11 shows the theoretical reactor antineutrino energy spectra from ^{235}U and ^{239}Pu fission, respectively, above the E = 1.8 MeV threshold [74, 75].

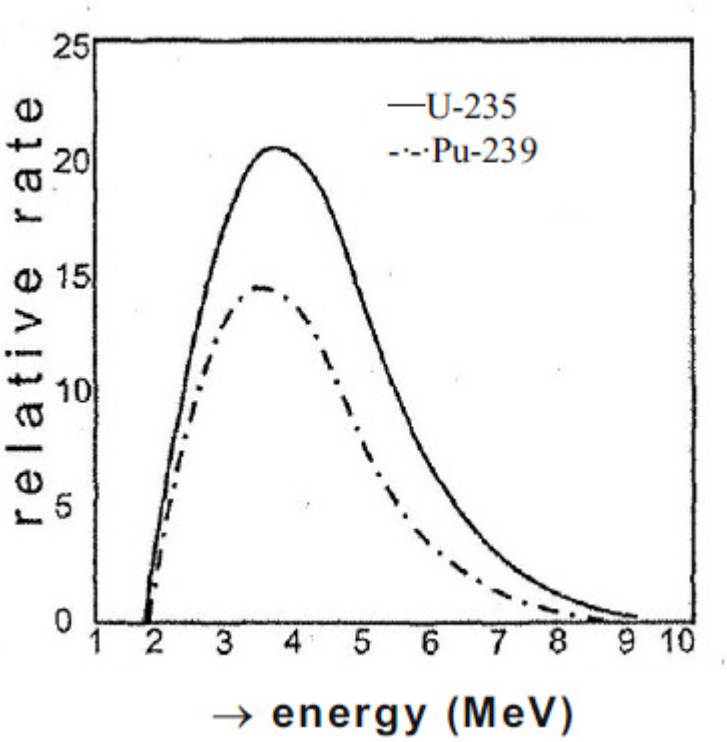

Figure 2.11: *Theoretical reactor antineutrino energy spectra and rate from ^{235}U and ^{239}Pu fission, respectively, above the E = 1.8 MeV threshold [74, 75].*

Figure 2.11 shows that the flux of antineutrinos from ^{235}U is higher than the flux from ^{239}Pu and that the antineutrino energy reaches a maximum close to E = 4 MeV, though the maximum energy is slightly lower for antineutrinos from ^{239}Pu fission. By measuring the antineutrino spectra during a fuel cycle, changes in the isotopic composition would result in changes in the antineutrino spectra thus causing deviation from the normal expected spectra. Therefore it would be possible be possible to determine if ^{239}Pu was removed from the core. Reactor monitoring with antineutrinos could therefore play a critical role in the non-proliferation of nuclear weapons.

2.5 Antineutrino flux at Koeberg

At the beginning of a reactor cycle at Koeberg, enough fuel is loaded to produce power for approximately eighteen months with a neutron yield consisting of approximately n(^{235}U) = 66 %, n(^{238}U) = 8 %, n(% ^{239}Pu) = 25 % and n(% ^{241}Pu) = 1 %.. The excess reactivity at the start of a cycle is countered with an appropriate amount of ^{10}B in the primary coolant, due to its large thermal neutron absorption cross section. If this procedure is not followed the reactor will rapidly increase in power. Through the progression of a cycle the ^{10}B concentration is reduced by 2 – 3 ppm/day. Towards the end of the cycle it becomes practically/economically unfeasible to reduce the ^{10}B concentration further. At this time a period called stretch-out is declared at either 10 ppm or 15 ppm depending on the cycle. During stretch-out the same fission reaction is ongoing as at full power. The only difference is that the reactor operates at a lower power level and therefore, less neutrons/fissions and less antineutrinos are produced. The power produced at the end of a cycle is usually at about 70 % after which it is reduced until shut down in a matter of hours.

Knowing the average number of neutrons released per fission η, the fission yield F can be determined for each isotope respectively at the start of a cycle:

$$F = \frac{N}{\eta}. \tag{2.31}$$

from which the normalised fission yield F_N is determined. The normalised number of antineutrinos from each nuclide per fission can then be determined by multiplying F_N with η. Table 2.5 provides these results.

Table 2.5: *Fuel composition at the beginning of a cycle at Koeberg, average number of neutrons and antineutrinos per fission and the normalised number of antineutrinos per fission.*

Start of cycle	N	η	$\bar{\nu}_e$/fission	F	F_N	Norm ($\bar{\nu}_e$/fission)
^{235}U	0.66	2.50	5.60	0.26	0.66	3.68
^{238}U	0.08	1.70	6.70	0.05	0.12	0.79
^{239}Pu	0.25	2.90	5.10	0.09	0.22	1.10
^{241}Pu	0.01	3.00	5.90	0.003	0.008	0.05

From Table 2.5 the total number of normalised antineutrinos per fission is obtained as 5.61 $\bar{\nu}_e$/fission. A fission releases approximately E = 200 MeV, thus a 2.7 GW_{th} reactor at Koeberg experiences approximately 8×10^{19} fissions per second leading to an isotropic antineutrino flux of $\phi_{\bar{\nu}_e} = 4.73 \times 10^{20}$ s^{-1}.

Similarly, Table 2.6 provides the details at the end of a cycle at Koeberg used to estimate the isotropic antineutrino flux as $\phi_{\bar{\nu}_e} = 4.66 \times 10^{29}$ s^{-1}.

Table 2.6: *Fuel composition at the end of a cycle at Koeberg, average number of neutrons and antineutrinos per fission and the normalised number of antineutrinos per fission.*

End of cycle	N	η	$\bar{\nu}_e$/fission	F	F_N	Norm ($\bar{\nu}_e$/fission)
^{235}U	0.40	2.50	5.58	0.16	0.41	2.31
^{238}U	0.08	1.70	6.69	0.05	0.12	0.82
^{239}Pu	0.47	2.90	5.09	0.16	0.42	2.14
^{241}Pu	0.05	3.00	5.89	0.02	0.04	0.25

The isotropic antineutrino flux at the beginning and end of the fuel cycle are almost equal and it indicates that measuring only the antineutrino flux does not provide information about the consumption and production of fissile material in the core, antineutrino energy information is also required.

The total antineutrino flux density at a distance r from the center of the core can be obtained by dividing the isotropic antineutrino flux by the surface of a sphere with radius r:

$$\phi(\bar{\nu}_e) = \frac{\phi(\bar{\nu}_e)}{4\pi r^2} \text{cm}^{-2}\text{s}^{-1}. \tag{2.32}$$

Because a second 2.7 GW_{th} reactor is a distance r' from the the measurement location, its contribution as well as the geoneutrino flux has to be taken into account to obtain the total antineutrino flux:

$$\phi(\bar{\nu}_e) = \left(\frac{\phi(\bar{\nu}_e)}{4\pi r^2} + \frac{\phi(\bar{\nu}_e)}{4\pi (r')^2} + 10^6 \right) \text{cm}^{-2}\text{s}^{-1}. \tag{2.33}$$

Figure 2.12 shows a schematic of the two reactors at Koeberg where the measurement locations are indicated by red dots. The centers of the cores are approximately l = 88 m apart.

Applying equation 2.33, the total flux at the measurement locations while both reactors are operating is estimated to be $\phi(\bar{\nu}_e) = 8\times10^{12}$ cm^{-2}s^{-1} at Koeberg I and $\phi(\bar{\nu}_e) = 1\times10^{13}$ cm^{-2}s^{-1} at Koeberg II and III. Thus an order of magnitude is gained in $\phi(\bar{\nu}_e)$ during Koeberg II and III. For calculations involving the antineutrino flux a 10% uncertainty will be added.

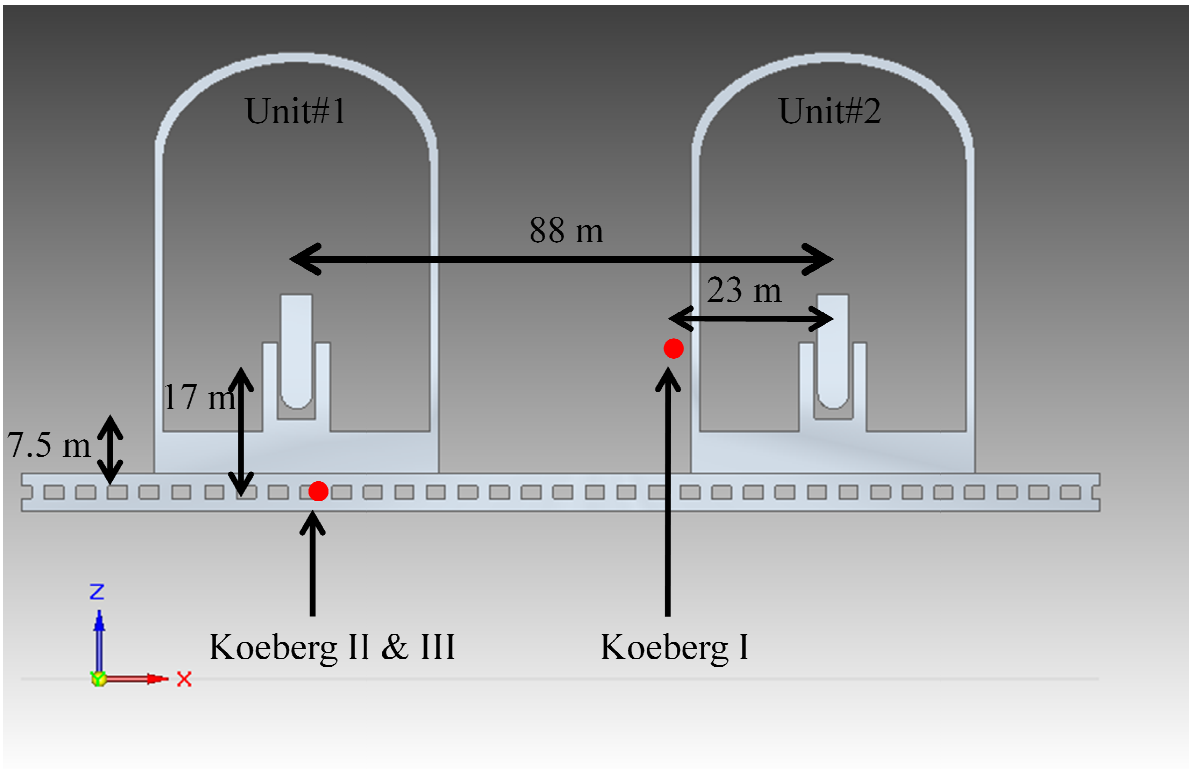

Figure 2.12: *Schematic of the two reactors at Koeberg. Measurement locations are indicated by red dots. The distances from the measurement locations to the cores are also indicated.*

Figure 2.13 shows the antineutrino spectrum calculated by Kopeikin [76] for a LWR, with similar fuel composition as at Koeberg, in the middle of the operating period. Line #1 represents all antineutrinos, #2 represents fission antineutrinos and #3 represents antineutrinos associated with neutron absorption in heavy elements like ^{238}U. Three-fourths of all emitted antineutrinos have energy below E = 1.8 MeV which remain undetected by conventional inverse β-decay measurements.

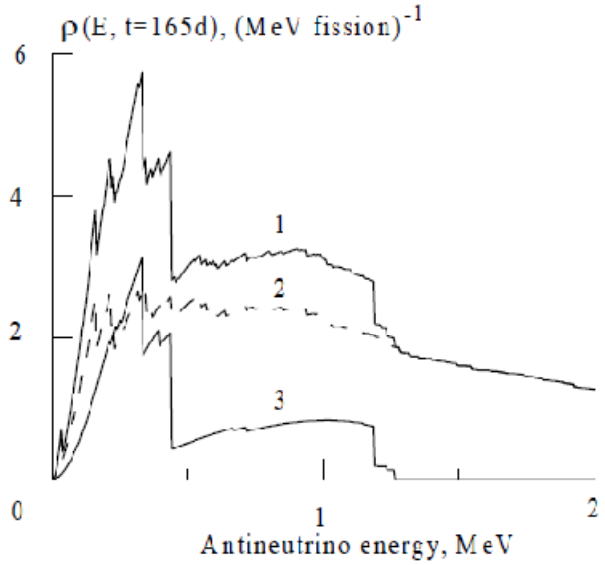

Figure 2.13: *Antineutrino spectrum of a LWR, see text for details explaining the meaning of the numbered lines [76].*

Because measurements in this project were made during several phases of reactor operation it is worthwhile to explore the antineutrino spectra at various times. Figure 2.14 shows the ratio of antineutrino spectra a certain number of days (a) after reactor start up and (b) after reactor shut down to the spectrum at the end of a 330 day operating period [76].

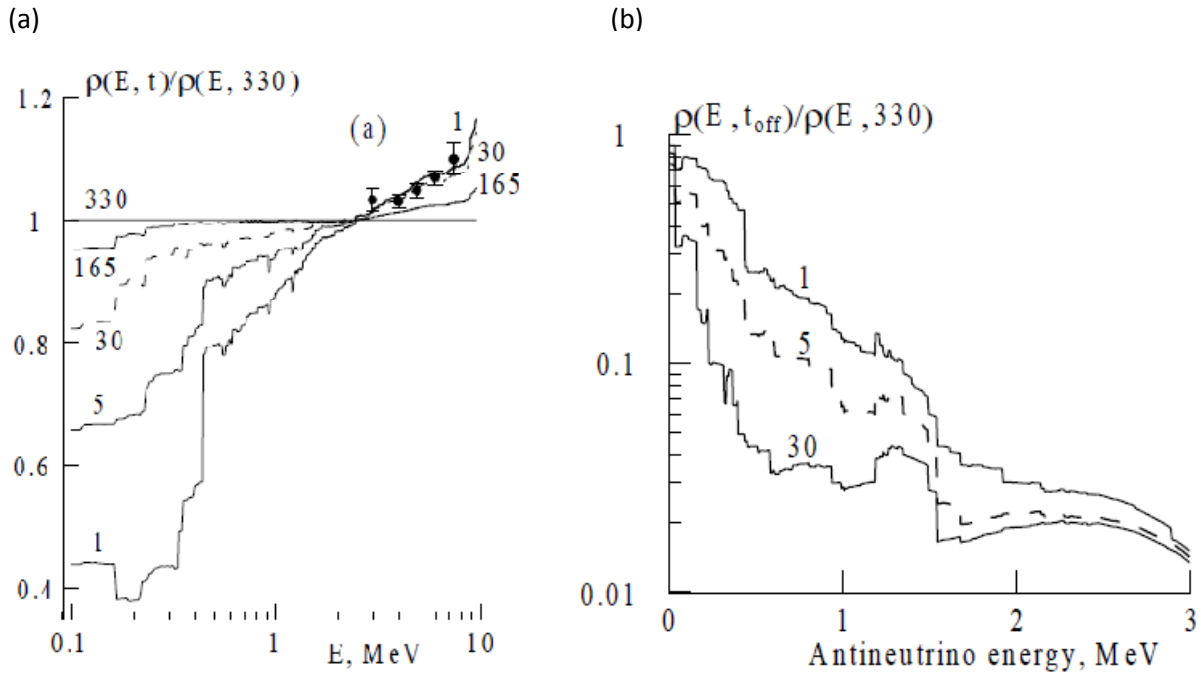

Figure 2.14: *Ratio of antineutrino spectra at various operating periods [76].*

After reactor start-up antineutrinos with energy E > 2.5 MeV dominate the spectrum in Figure 2.14 (a). From Figure 2.14 (b) the flux of antineutrinos with energy E > 1.5 MeV decreases faster than antineutrinos having energy E < 1.5 MeV. If antineutrinos do have an effect on β^+-decay rates, observing when and how the change occurs could hold information on the energy of the associated antineutrinos.

2.6 Neutrino detection

Since the detection of the neutrino by Reines and Cowan, the basic detection method has not changed. The extremely small cross section for the reaction in equation 2.1, $\sigma(\bar{\nu}_e) = 11 \pm 2.6\times10^{-44}$ cm^2 [77] requires that a large volume of scintillator be used to improve the detection efficiency. In addition, the antineutrino energy has to exceed the 1.8 MeV threshold energy for this reaction. Typically the required scintillator has a mass of the order of tons, measuring only a few hundred antineutrino events per day. Some of these detectors are aimed at monitoring nuclear reactors, studying neutrino oscillations and neutrino astronomy. The biggest undertaking in measuring neutrinos comes in the form of the Super-Kamiokande detector; consisting of 50 000 tons of ultra-pure water and approximately 11 000 photomultiplier tubes measuring Cherenkov radiation produced by neutrinos interacting with hydrogen nuclei. Super-Kamoikande is designed to monitor proton decay, antineutrinos from supernovae and study solar and atmospheric neutrinos.

Because shielding from antineutrinos is not possible, antineutrino detection could play a critical role in the monitoring and safeguarding of nuclear reactors; application thereof has been demonstrated by various groups since 1982. An overview can be found in reference [78]. Antineutrinos leaving a reactor core provide a real-time monitor of the fuel evolution of a reactor. The following sections provide an overview of the state of the art of reactor monitoring with antineutrinos.

2.6.1 Rovno detector

The first efforts to utilize antineutrino detection as a tool to monitor nuclear reactors came from physicists at Rovno Atomic Energy Station in Kuznetsovsk, Ukraine in 1982. A detection system consisting of 1050 L of Gd-doped liquid scintillator was installed 18 m below the 440 MW_{th} reactor; providing background shielding [60]. A net antineutrino rate of 760 ± 6 $\bar{\nu}$/day and 30% detection efficiency were achieved [60]. The Rovno detector was able to measure the thermal power of the reactor to 2% precision [60] by relating the antineutrino

count rate to the number of fissions in the core, since each fission releases approximately E_{tot} = 200 MeV.

2.6.2 SONGS detector

During 2003 and 2007 N.S. Bowden and collaborators designed, installed and operated the SONGS1 antineutrino detector at the San Onofre Nuclear Generating Station (SONGS) for monitoring of fissile material, demonstrating the feasibility of antineutrino detectors in the context of IAEA safeguards [61]. Their central detector consisted of four identical stainless steel cells each having a volume of approximately 0.18 m^3 (0.72 m^3 total volume) and filled with 640 kg of gadolinium (Gd) doped liquid scintillator. Each cell was read out by two 8-inch PMT's [61]. Passive shielding against neutrons and γ-rays was achieved by a six-sided water/polyethylene shield of average 0.5 m thickness. A 5-sided muon detector was used for tagging and vetoing muon-related backgrounds. A total of 28 PMT's were used to read out both the muon veto and the central detector.

The SONGS1 detector was deployed about 25 m from the reactor core of Unit#2, in the tendon gallery 10 m underground, directly below the containment dome [61, 78, 79]. The detection relies on inverse β-decay of protons resulting in a positron and neutron which interact in the scintillator, emitting γ-rays. Because γ-rays can travel up to 30 cm in the scintillator, a large number of γ-rays escape the walls of detector leading to a reactor antineutrino count rate of about 400 events per day and resulting in a detection efficiency of 10%, corresponding to an effective volume of only 0.072 m^3 [78, 79]. Figures 2.15 illustrate the correlation between reactor thermal power and reactor antineutrino count rate (a) as the reactor powers up to full power and (b) before, during and after reactor refuelling at SONGS [79].

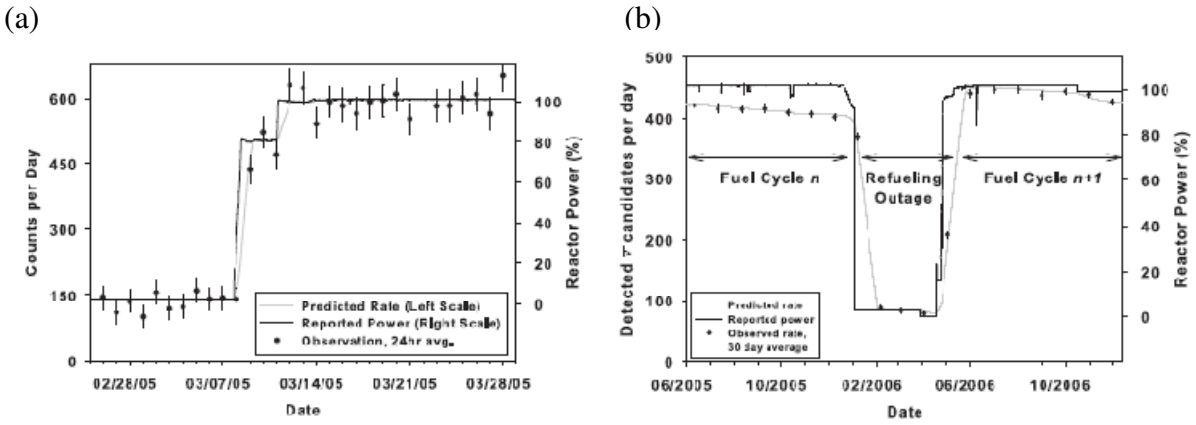

Figure 2.15: *Illustration of the correlation between reactor thermal power and reactor antineutrino count rate measured at SONGS [79].*

Having been urged by the safeguards community to avoid a toxic and flammable liquid scintillator, the collaboration built a second detector (SONGS2) based upon a non-flammable, non-toxic plastic scintillator in 2007. Although they managed to halve the total volume of the SONGS1 detector, the newer version still has a rather large total volume of 0.36 m^3 and slightly lower detection efficiency due to the detector design and the low plastic scintillator proton density. Disadvantages of the liquid based detectors are that they have to be assembled on site and special care has to be taken to prevent any spillage or leakage. The plastic based detectors can be assembled remotely and transported and installed with relative ease.

2.6.3 NUCIFER detector

The construction and operation of the NUCIFER liquid scintillator antineutrino detector is part of the Nucifer project; a collaboration between the Commissariat a l'energie atomique Direction des sciences de la matière (CEA/DSM), the CEA Direction des application militaires (CEA/DAM) and the Centre national de la recherche scientifique – Institute national de physique nucléaire et de physique des particules (CNRS-IN2P3), which aims to ascertain the effectiveness of the technology for safeguard purposes [78]. The detector has a simple design, is easy to construct, integrate, and does not have to be operated by specialists. Also employing the process of inverse β-decay, the NUCIFER detector is composed of 1.5 m^3 of Gd doped liquid scintillator enclosed in a double steel vessel, surrounded by 30 cm of lead/polyethylene shielding [78]. Readout is achieved with 16 PMTs separated from the liquid by a 25 cm thick acrylic plate [78]. The detector is monolithic, with a small surface to volume ratio which favours a high detection efficiency [78]. The whole detector volume is

kept under nitrogen atmosphere to satisfy fire-safety requirements. The base of the detector is 3×3 m^2 with a weight of 30 tons due to the steel shielding. The standout feature of this detector is its tremendous shielding capability, but this makes the detector very large and heavy. The detector is operating 7 m from the core of the 70 MW OSIRIS reactor in Saclay, France.

2.6.4 GiZA detector

The Stichting EARTH (Earth AntineutRino TomograpHy) project proposal has an aim to create a high-resolution 3D-map of the radiogenic heat sources (uranium and thorium) in the Earth's interior by detecting the direction of low-energy antineutrinos, known as geoneutrinos, emitted from these radioactive elements. As such there exists a need for direction-sensitive antineutrino detectors, also in demand for reactor monitoring. The proposed GiZA (Geoneutrinos in South Africa) detector is designed to characterize an antineutrino event by measuring the pulse-height properties of both the positron and neutron-capture signals, as well as their timing properties to provide a direction-sensitive measurement. The particle with the smallest mass (positron) will carry away most of the energy, while the particle with the largest mass (neutron) carries away most of the momentum and directional information of the antineutrino.

The detector will have a tetrahedron shape containing 40 L of ^{10}B doped liquid scintillator; ELJEN 309 which is non-toxic and has a high flame point. This shape allows position determination by triangulation measurements of the arrival times and magnitude differences of the scintillation signals. The large thermal neutron capture cross section of ^{10}B, $\sigma_{^{10}B}$ = 3840 barns, will provide a detection efficiency of 40 -50 % leading to a net count rate of 90 antineutrino events per day at a distance of 25 m from a 3 GW_{th} reactor such as SONGS.

The ^{10}B doped ELJEN 309 holds one great advantage over the traditional capture by hydrogen or Gd; a major reduction in the background count rate can be achieved by setting a time window of about 1 μs for delayed coincidences between the positron and the neutron-induced α-pulse, compared to the 28 μs of the SONGS detector. The Gd doped SONGS detector releases a γ-ray of about 8 MeV after neutron capture, the detection of which requires a large amount of scintillation material, on the other hand charged particles can be detected in smaller volumes closer to the original interaction which preserves position information and increases efficiency for the same volume.

Other similar initiatives around the world are underway with the goal to monitor nuclear reactors, mostly utilizing tonnes of scintillator. When constructing antineutrino detectors the following criteria have to be considered: measurements should be non-intrusive to reactor operations, continuous, safe, unattended, automatic and remote. Optimizing the cost, complexity, size, sensitivity and efficiency should also be taken into consideration. The above mentioned detectors rely on the direct detection of antineutrinos.

2.7 Summary

Chapter 2 provides an introduction to the history of neutrinos, neutrino properties, the many sources thereof and neutrino detection. Though in this work only the effect of antineutrinos is investigated. Therefore the basic knowledge of reactor physics and consequently how reactor antineutrinos are produced was provided in some detail so that an assessment of the antineutrino-flux and energy spectrum could be made. Chapter 3 introduces interactions of radiation with matter as this work is dependent on radiation detection.

CHAPTER 3 Particle interactions with matter

Understanding how radiation interacts with matter and the consequences thereof is important for its detection. Depending on their properties, particles can interact strongly, weakly or electromagnetically. Charged particles, for example; electrons (e^-), positrons (e^+) and alpha particles (α) interact more with matter than neutral particles such as neutrons (n) and neutrinos (ν) or photons, such as γ-rays. Studying the interaction of radiation with matter has led to the development of a range of radiation detectors of which scintillation detectors are probably the most widely used today in terms of the detection and spectroscopy of a wide range of radiations [80, 81]. Not only does the interaction of radiation with matter depend on the properties of the type of radiation (such as energy, mass and charge) but also on the properties of the detection material. In this chapter the interaction mechanisms of the most common decay products of radionuclides with matter and their implication for detection are described.

3.1 Interaction of charged particles

3.1.1 Alpha particles

An α-particle is a heavy charged particle compared to an electron, but light compared to a heavy nucleus It consists of two protons and two neutrons and is a helium nucleus [26]. Alpha particles are mainly produced by, but not restricted to, the decay of radionuclides with an atomic number greater than Z = 82; it also occurs for lower Z proton-rich nuclei [2]. The primary interaction of the positively charged α-particle is through Coulomb interaction with the orbital electrons of the atoms of the detection material [26, 80]. Interaction with nuclei is also possible but due to the large atomic radius compared to the nuclear radius the cross section for this interaction is very low and considered insignificant [26, 80]. As an α-particle passes through the detection material it interacts with many electrons simultaneously by one of two processes; either by excitation where the electron is raised to a higher energy shell or by ionization where the electron is ejected from the atom [26, 80]. Both processes involve energy transfer to electrons whereby the energy and thus velocity of the α-particle is continuously reduced until it stops [80]. By using a detection material with higher atomic number more atomic electrons become available for excitation or ionization, thereby greatly reducing the range of α-particles [80]. The higher the energy of the α-particle the greater its penetrating range will be as more electrons are required for stopping by Coulomb interaction.

The penetrating range is thus determined by three factors; energy of the α-particle, atomic number and density of the detection material [80]. Due to the heavy mass of an α-particle it does not deviate much from its path during interaction with orbital electrons, in contrast the path of an electron with equivalent energy can be more erratic [80]. In the GiZA detector the range would be a few μm.

3.1.2 Electrons

Because an electron has a smaller mass compared to an α-particle it can achieve a greater velocity with equivalent energy [26]. Energetic electrons interact with orbital electrons through the Coulomb interaction causing ionization or excitation [26]. Since the incident electron mass is equal to the orbital electron mass, the electron can transfer a significant amount of its energy to an orbital electron during scattering, causing it to be ejected from the atom [26]. The ejected electron can in turn cause ionization, called secondary ionization which can account for as much as 80% of the total ionization [26]. Electron scattering leads to deceleration of the incident electron during which energy is radiated via electromagnetic radiation called Bremsstrahlung [81]. The number of electron interactions increases as the density and thickness of detection material increases [26]. The small mass of an electron combined with its lower charge and greater velocity leads to ionization in air which is almost a factor of a thousand lower than for α-particles with equivalent energy, resulting in a greater penetrating range [26].

3.1.3 Positrons

A positron is the anti-particle of an electron; having a negative lepton number and positive charge. For this reason it is understandable that positrons interact with matter via similar mechanisms as electrons. Also, the specific energy loss and range of positrons are almost the same as for electrons. Positrons may annihilate with electrons in its flight path or at the end of its path. Prior to annihilation the positron and electron briefly form a positronium atom which is purely leptonic, consisting of the two spin-half particles. Positronium can decay electromagnetically into a number of photons, depending on its quantum mechanical state just before decay [82]. If the spin alignment of the positron and electron is parallel, the state is called orthopositronium, if the spin alignment is antiparallel it is called parapositronium [82]. In vacuum, orthopositronium decays into an odd number of photons, three being the most likely, parapositronium decays into an even number of photons, two being the most likely [82]. The dominant decay mode is via two photon decay with a branching ratio of

approximately 99.9% [82]. The lifetime of parapositronium remains approximately 125 ps in a medium such as a liquid, whereas the life-time of orthopositronium becomes considerably shorter from approximately 142 ns to 1.8 ns in a medium due to pick-off annihilation when an electron with opposite spin in the medium reacts with the positron of the orthopositronium atom resulting in two photon annihilation [82]. The two released photons are counter propagating and have energy of E_γ = 511 keV each [26, 80]. These E_γ = 511 keV photons deposit their energy far from the annihilation position due to their large range.

3.2 Interaction of neutral radiation

3.2.1 Gamma-rays

Because γ-rays are uncharged they rely on an electromagnetic interaction with an atom whereby part or all of its energy is absorbed after which energy is released from the atom through the ejection of an electron [26, 80]. The energy of the ejected electron is thus a representation of the incident γ–ray energy. The emission of an electron causes a secondary effect as it interacts via the Coulomb interaction causing ionization or excitation through the processes described in section 3.1.2. The detection of γ-rays can be seen as a two step process whereby the detection material must provide a high interaction probability for a γ-ray to yield a free electron and then act as a detector for the ejected electron. Gamma-rays interact with matter through three main mechanisms; photoelectric absorption, Compton scattering and pair production [80, 81].

3.2.1.1 Photoelectric absorption

Photoelectric absorption allows a γ-ray to be totally absorbed by an atom resulting in the emission of a photoelectron from one of the electron shells [80, 81]. The energy of the photoelectron, E_{e^-} is equal to the energy of the incident γ–ray, E_γ, minus the energy needed to overcome the binding energy of the electron, E_b [80, 81]:

$$E_{e^-} = E_\gamma - E_b. \tag{3.1}$$

The binding energy ranges from a few eV to tens of keV, therefore the energy lost by overcoming the binding energy is negligible and the photoelectron provides a measure of the energy of the incident γ-ray [80]. Photoelectric absorption is the preferred mode of interaction for low-energy γ –rays and the probability increases for detection materials with high Z. The photoelectric absorption cross section per atom, $\sigma_t(m^2kg^{-1})$, can be approximated by:

$$\sigma_t \cong \text{const} \times Z^n E_\gamma^{-3.5}, \tag{3.2}$$

where n varies between 4 and 5 over the γ-ray energy region of interest [80, 81]. Also noticed is that the cross section decreases abruptly with an increase in energy.

3.2.1.2 Compton scattering

During Compton scattering an incident γ-ray with energy E_γ transfers part of its energy to an atomic electron (assumed to be at rest), after which the γ-ray is deflected at an angle θ relative to its initial direction and the electron recoils at an angle ϕ [26, 80]. This process is illustrated by Figure 3.1. Using conservation laws of energy and momentum, the energy of the deflected γ-ray, E_γ', as a function of the scattering angle, θ, follows as:

$$E_\gamma' = \frac{E_\gamma}{1+\frac{E_\gamma}{m_0c^2}(1-\cos\theta)}, \tag{3.3}$$

where m_0c^2 = 511 keV is the rest-mass energy of an electron [80]. The energy of the recoil electron, E_e, is obtained by [26]:

$$E_e = E_\gamma - E_\gamma' - E_b. \tag{3.4}$$

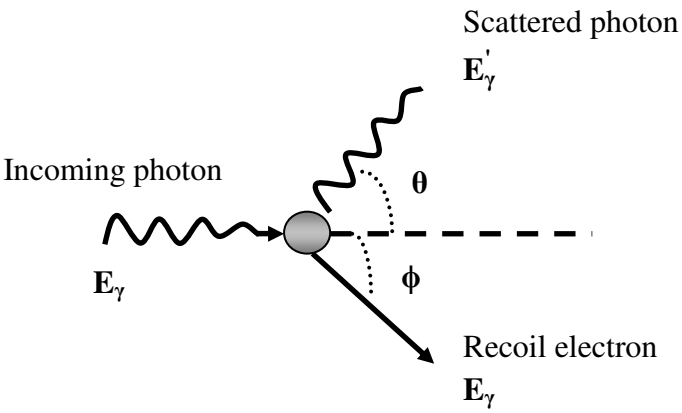

Figure 3.1: *A graphical illustration of the Compton scattering process.*

The angular distribution of scattered γ-rays is described by the Klein-Nishina formula for the atomic differential scattering cross section, $\frac{d\sigma(\theta)}{d\Omega}$:

$$\frac{d\sigma(\theta)}{d\Omega} = \frac{Z\, r_0^2}{2}\left[\frac{1}{[1+\alpha(1-\cos\theta)]^2}\left(1+\cos^2\theta+\frac{\alpha^2(1-\cos\theta)^2}{1+\alpha(1-\cos\theta)}\right)\right], \tag{3.5}$$

where $\alpha = E_\gamma/m_0c^2$ and r_0 is the atom radius [80]. This equation shows that for high-energy γ-rays forward scattering is dominant.

The cross section for Compton scattering per unit mass, $\sigma_\sigma\left(m^2kg^{-1}\right)$, is determined by:

$$\sigma_\sigma = \text{const} \times E_\gamma^{-1}. \tag{3.6}$$

Equation 3.6 shows that the probability for Compton scattering is independent of the atomic number of the detection material and only depends on its density; where more target electrons are available in a denser the material the cross section will be larger [81]. Figure 3.2 shows for the atomic differential scattering cross section the photoelectric absorption is the dominant mode of interaction for low energy γ-rays with energy up to several hundred keV, whereas pair production is the dominant mode of interaction for high energy γ-rays with energy above 5 MeV. Compton scattering is the dominant process for γ-rays with intermediate energy. In the NaI(Tl) and $LaBr_3$(Ce) detectors used in this work, the photons resulting from the decay of ^{22}Na have energies of E_γ = 511 keV and 1275 keV and mainly interact through Compton scattering.

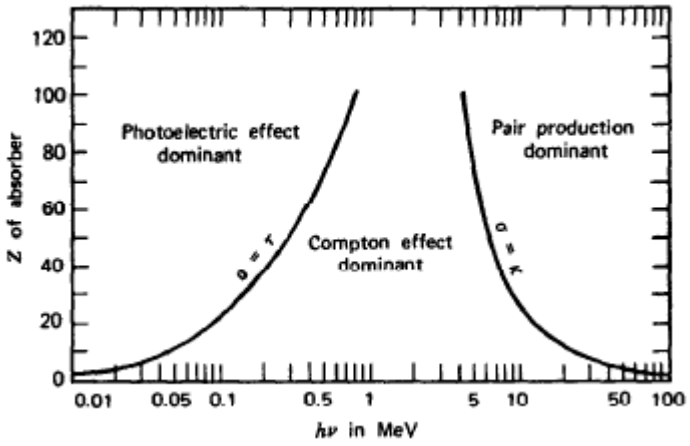

Figure 3.2: *Energy regions indicating the dominant modes of interaction for γ-rays with various energies [80].*

3.2.1.3 Pair-production

Pair production is the process whereby a γ-ray is converted into an electron-positron pair in Coulomb field of a nucleus. For this process to occur the γ-ray energy has to exceed twice the rest-mass energy of an electron; $E_\gamma > 1.022$ MeV [80, 81]. The excess energy above the 1.022 MeV required to make an electron-positron pair is shared between the electron and positron as kinetic energy [80]. The positron subsequently loses its kinetic energy slowing down in the medium, forming an intermediate state with an electron, positronium, annihilates with the electron predominantly producing two back-to-back $E_\gamma = 0.511$ MeV photons.

Pair-production is the dominant mode of interaction for γ-rays with $E_\gamma > 5$ MeV. The cross section per unit mass, $\sigma_\kappa \left(m^2kg^{-1}\right)$, is given by:

$$\sigma_\kappa = \text{const} \times ZE_\gamma^2 \tag{3.7}$$

and increases with atomic number and the square of the γ-ray energy.

3.2.2 Build-up of an energy spectrum

The interaction mechanisms described in section 3.2.1 contribute to an energy spectrum through the detection of ejected electrons. If almost all the energy of a γ-ray is transferred to an electron, either by photoelectric absorption or by multiple Compton scattering in combination with photoelectric absorption, its energy will show up in a gamma-ray spectrum as a peak at the energy of the incident γ-ray. During Compton scattering an incident γ-ray can scatter off to any angle, thus transferring either a certain maximum, part or almost none of its energy to an electron. It may leave the detector or being absorbed or scattered again in the detector (multiple scattering). The detector will record the total energy transferred to the electrons.

The recoil electron has a continuum of energy which lies between two extreme cases when the scattering angle is $0 < \theta < \pi$, leading to the minimum and maximum energy of the recoil electron. When $\theta = 0$ the γ-ray transfers no energy to an electron, $\theta = \pi$ leads to maximum energy transfer corresponding to what is known as the Compton edge in a γ-ray spectrum with discrete energy transitions. Figure 3.3 illustrates these two extremes and the shape of the continuum predicted by the Klein-Nishina formula in an ideal detector.

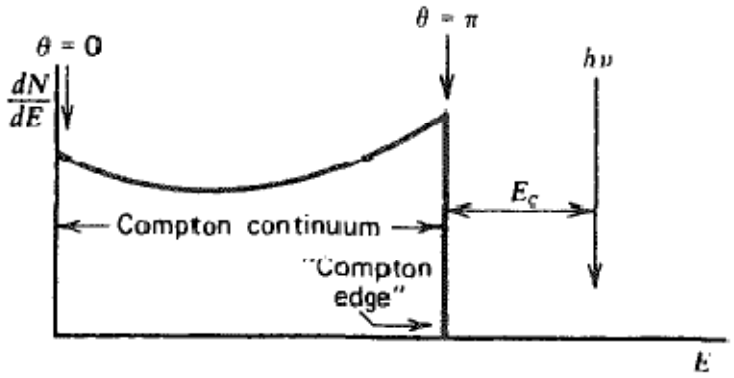

Figure 3.3: *Compton continuum in an ideal detector [80].*

From equation 3.4 the maximum energy transferred to an electron, $E_{e^-}(\theta = \pi)$, is obtained [80]:

$$E_{e^-}(\theta = \pi) = h\nu \left(\frac{2h\nu/m_0c^2}{1 + 2h\nu/m_0c^2} \right). \tag{3.8}$$

Realistically the binding energy of an electron before recoiling has an effect on the shape of the continuum, leading to the rounding-off of the Compton edge and a finite slope instead of the abrupt cut-off at the Compton edge. Low energy peaks resulting from the interaction of γ-rays with the material surrounding a detector are commonly seen in spectra.

A backscatter peak resulting from a γ-ray Compton scattering off the surrounding material is usually seen between $200 < E_\gamma < 250$ keV [80]. Photoelectric absorption of γ-rays in the surrounding material leads to the emission of x-rays, also seen in the low energy region of spectra [80]. The process of pair production results in the incident γ-ray losing energy through the emission of two $E_\gamma = 511$ keV photons. The two $E_\gamma = 511$ keV photons can either be detected fully or partially, in coincidence with the original γ-ray resulting in a photopeak corresponding to the incident γ-ray energy or lower energy sum peak [80]. If both of the $E_\gamma = 511$ keV photons are not detected a so called double escape peak results at an energy of $2m_0c^2$ below the energy of the incident γ-ray, if only one of the $E_\gamma = 511$ keV photons is detected a so called single escape peak is observed at an energy of m_0c^2 below the energy of the incident γ-ray [26, 80].

3.2.3 Coincidence summing

Situations when two γ-rays are fully detected within the time resolution of the detector lead to the summing of the energy of the individual γ-rays, forming a coincidence sum peak at the energy of the sum. The summation of partial energy loss interactions leads to sum events at energies below the sum peak. Coincidence summing effectively removes counts from the individual full-energy peaks of the individual discrete energy γ-rays. For two γ-rays, γ_1 and γ_2, in coincidence, the full-energy peak area in the absence of summing is:

$$N_1 = \varepsilon_1 S y_1 \tag{3.9}$$

and

$$N_2 = \varepsilon_2 S y_2, \tag{3.10}$$

where ε_1 and ε_2 are the intrinsic full-energy peak efficiency of the detector for γ_1 and γ_2, respectively, S the source activity and y_1 and y_2 the yields of γ_1 and γ_2 per disintegration [80]. The probability of simultaneous detection of γ_1 and γ_2 is the product of the individual detection probabilities multiplied by a factor $W(0^\circ)$ which accounts for any angular correlation between the γ-rays. $W(0^\circ)$ is defined as the relative yield of y_2 per unit solid angle about the 0° direction defined by the detector position, given that γ_1 is emitted in the same direction [80]. If γ_1 and γ_2 result from the same decay branch, the area of the sum peak, N_{12}, is then obtained [80]:

$$N_{12} = S\varepsilon_1\varepsilon_2 y_1 W(0^\circ)$$

$$= S\varepsilon_1\varepsilon_2 y_1 W(0^\circ). \tag{3.11}$$

For most cascade transitions $W(0^\circ)$ is in the range 1 to 1.2 and can usually be neglected, for a well-counter $W(0^\circ)$ will equal unity [83]. The number of events removed from the full-energy peak of γ_1, $N_1|_{\text{with summing}}$, for example, during coincidence summing is obtained by:

$$N_1|_{\text{with summing}} = N_1 - N_{12}$$

$$= \varepsilon_1 S y_1 [1 - \varepsilon_2]. \tag{3.12}$$

This method serves as an approach to describe coincidence summing in a cylindrical crystal in Chapter 4.

3.3 Summary

Chapter 3 describes the interaction of charged and neutral particles with matter, laying the basis for understanding how particles are detected; represented by an energy spectrum and how it is built-up. Features of an energy spectrum were discussed and how the features are related to the interaction of the particles with matter. An introduction to coincidence summing is provided in a general case which will be applied to the γ-rays resulting from the decay of ^{22}Na; being detected in a cylindrical crystal as well as a well-counter in Chapter 4. Chapter 4 also provides a description of the methods used to analyse energy spectra.

CHAPTER 4 Analytical methods

Various methods to analyse γ-ray spectra differ in the resulting accuracies and precisions. For detecting subtle changes in decay rates a robust method is required delivering the best accuracy and precision. Each method is based on a set of assumptions, which consequently lead to systematic uncertainties and hence reduce the accuracy. In high statistics measurements like those performed in this project, high precision is obtained and accuracy becomes the limiting quantity. In this chapter the most accurate method, which turned out to be the Net-Peak Ratio Analysis (NPRA), is described.

To reduce systematic uncertainties γ-ray spectra are spectrum-stabilised to ensure that they possess the same energy to channel relation such that they can be summed or subtracted, and certain regions of interest (ROIs) can be analysed.

This chapter describes the off-line gain-stabilisation procedure and NPRA.

4.1 Spectrum-stabilisation

Changes in temperature and humidity may lead to gain shifts in gamma-ray spectra. A gain-shifted spectrum, S(j) can be stabilised with respect to the reference spectrum $S^*(i)$, where j and i are the respective channel numbers. A method for stabilising gain-shifted spectra was developed by Stapel *et al*. [84] and is employed in this work. It is assumed that the mapping function m(j) = i relates the channels of S and S^* through a second order polynomial:

$$i = m(j) = a_0 + a_1 j + a_2 j^2. \tag{4.1}$$

Through the mapping function m(j) the contents of the channels in the spectrum S can be redistributed over the channels of the stabilised spectrum S^* with the following equation:

$$S_i^* = \sum_{m(j+1)>i}^{m(j)<i+1} \frac{\min\big(i+1, m(j+1)\big) - \max(i, m(j))}{m(j+1) - m(j)} S_j. \tag{4.2}$$

A code was written in MATLAB to carry out the stabilisation; the code was checked by calculating a few stabilised spectra by hand and was compared to the output of the code.

4.2 Uncertainties

Associated with any measurement and analysis, are uncertainties. Uncertainties are either statistical or systematic of nature; they are related to precision and accuracy, respectively. Precision reflects the spread around a mean value; whereas accuracy refers to how close a mean value of a measurement is to the true value. In the final result the uncertainty is determined by the propagation of uncertainties under operands like addition and multiplication. The top panel in Figure 4.1 shows schematically examples of a precise measurement with a low accuracy and the bottom panel a very accurate measurement with a low precision, the true value is indicated by the straight line at a value of 5.

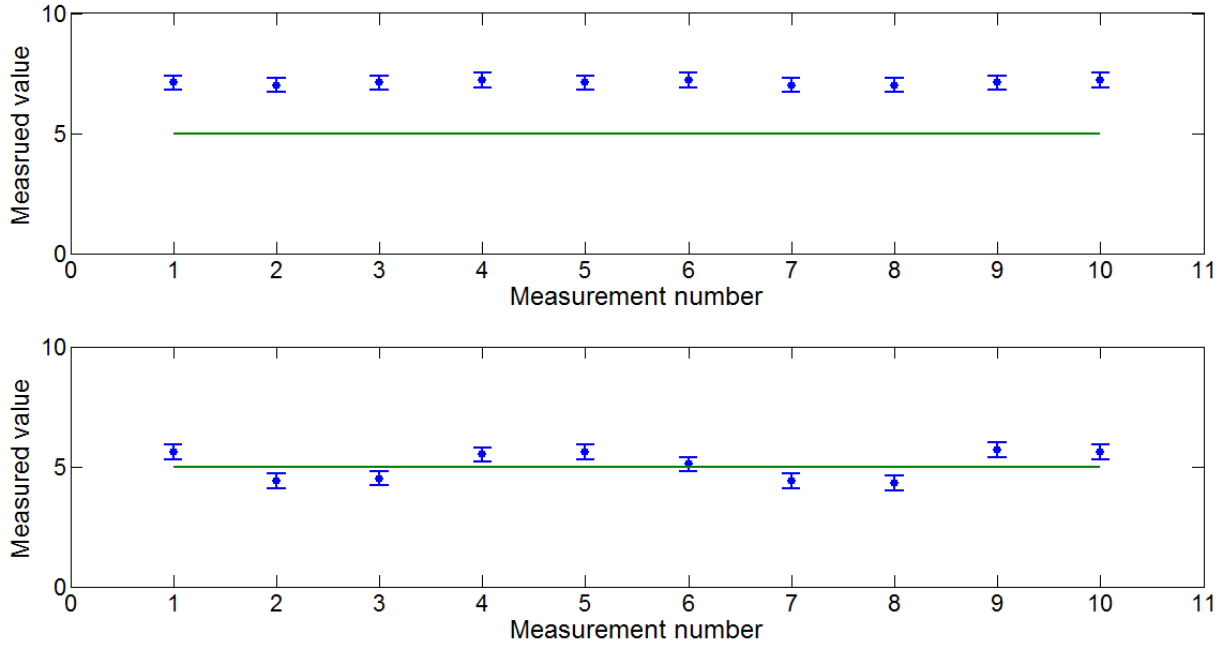

Figure 4.1: *A precise measurement with low accuracy (top) and an accurate measurement with low precision (bottom).*

For M independent measurements of a quantity x_i with uncertainty σ_i, where i = 1,…,M, the values are Gaussian distributed around a mean value $\bar{x}$. The mean value can be estimated by a weighted mean [85]:

$$\bar{x} = \frac{\sum_i^M \frac{x_i}{w_i}}{\sum_i^M \frac{1}{w_i}}, \tag{4.3}$$

where each measurement is weighted by its own variance:

$$w_i = \sigma_i^2. \tag{4.4}$$

The sample variance of the set of measurements indicates the spread of the values around the mean and is a collective property of the set [85]:

$$\mathrm{var}(\bar{x}) = \frac{1}{M\text{-}1}\sum_{i=1}^{M}(x_i\text{-}\bar{x})^2 = \sigma_x^2, \tag{4.5}$$

where σ_x is the standard deviation of the set.

Specific rules for uncertainty propagation have to be applied to calculations involving functions of multiple variables, f(u, v) [79]:

$$f = au \pm bv \quad \rightarrow \quad \sigma_f^2 = a^2\sigma_u^2 + b^2\sigma_v^2 + 2ab\sigma_{uv}^2, \tag{4.6}$$

$$f = auv \quad \rightarrow \quad \frac{\sigma_f^2}{f^2} = \frac{\sigma_u^2}{u^2} + \frac{\sigma_v^2}{v^2} + 2\frac{\sigma_{uv}^2}{uv}, \tag{4.7}$$

$$f = \frac{au}{v} \quad \rightarrow \quad \frac{\sigma_f^2}{f^2} = \frac{\sigma_u^2}{u^2} + \frac{\sigma_v^2}{v^2} - 2\frac{\sigma_{uv}^2}{uv}, \tag{4.8}$$

where a and b are constants. By applying the propagation of uncertainties the variance in the weighted mean is determined:

$$\sigma_{\bar{x}}^2 = \frac{1}{\sum_{i=1}^{N}\frac{1}{w_i}}. \tag{4.9}$$

In most cases it is expected that the measured values x_i follow some function or mean value. To test how well the measured data fit to the mean, a Chi-squared (χ^2) test can be applied, defined as [85]:

$$\chi^2 = \frac{1}{M - \nu}\sum_{i=1}^{M}\frac{(x_i\text{-}\bar{x})^2}{w_i} = \frac{1}{M\text{-}1}Q, \tag{4.10}$$

where ν is the number of parameters that has to be extracted (the mean in this case, thus ν = 1). The χ^2-value provides a measure of the difference between the measured data and the function that the data are expected to follow [86]. If there is good agreement of the data with i.e. the mean value, then each data point will deviate from the mean by approximately one standard deviation, resulting in a Q-value approximately equal to $M - \nu$ [87]. Therefore the

expected value of χ^2 is equal to unity [87]. A χ^2-value much larger than unity indicates that significant deviations from the expected function occur, possibly due to a poor choice of the expected function or poor measurements polluted by systematic uncertainties or incorrect assignment of uncertainties [85]. A very small χ^2-value indicates that either the measured data are unrealistically close to the expected function or that the uncertainties have been overestimated, therefore reducing the χ^2-value [87]. The χ^2-value is related to a chosen confidence level of a result; indicating the probability that the true value of an unknown parameter lies within a certain number of standard deviations from the measured parameter [86, 87, 88]. The significance level of a result is related to the confidence level through the compliment of the confidence level [88]. The significance level, also known as the P-value gives the probability that deviations from the null hypothesis are due to chance only and provides a method to decide whether or not the null hypothesis can be rejected [86, 87 88]. For a normal distribution, values are spread around their mean and the null hypothesis would be that significant deviations from the mean do not occur. Often and in this work a confidence level of 95% is chosen which corresponds to a P-value of 5% [86, 87]. Obtaining a χ^2-value which corresponds to a P-value > 5% means that the null hypothesis cannot be rejected and the true value of the mean lies within 1.96σ of the measured mean [87]. The P-value can be looked up in a Chi-square distribution table as a function of the number of degrees of freedom, $M - \nu$ and χ^2.

When data are expected to follow a more complex function of multiple parameters, a $\chi 2$-minimisation can be applied to extract the values of parameters that will produce the best fit to the data. No prescribed method for estimating the uncertainty of the parameters exists, but most commonly, in equation 4.10, Q is Taylor expanded to second order, around the value of the parameter where χ^2 is a minimum [81], i.e. for $\chi^2(\lambda)$:

$$Q(\lambda) = Q(\lambda_{min}) + \frac{1}{2}\frac{\partial Q}{\partial \lambda}\left(\lambda - \lambda_{min}\right)^2$$

$$= Q(\lambda_{min}) + \frac{1}{\sigma^2}(\lambda - \lambda_{min})^2, \qquad (4.11)$$

since

$$\sigma^2 = \left|\frac{1}{2}\frac{\partial^2 Q}{\partial \lambda}\right|^{-1}. \qquad (4.12)$$

At $\lambda = \lambda_{min} + \sigma$:

$$Q(\lambda_{min} + \sigma) = Q(\lambda_{min}) + 1 \tag{4.13}$$

and

$$\chi^2(\lambda_{min} + \sigma) = \chi^2(\lambda_{min}) + \frac{1}{M\text{-}1}. \tag{4.14}$$

Thus, the uncertainty of λ_{min} corresponds to the region between the values of λ where the χ^2-distribution is equal to $\chi^2(\lambda_{min}) + \frac{1}{M\text{-}1}$. This is graphically illustrated in Figure 4.2.

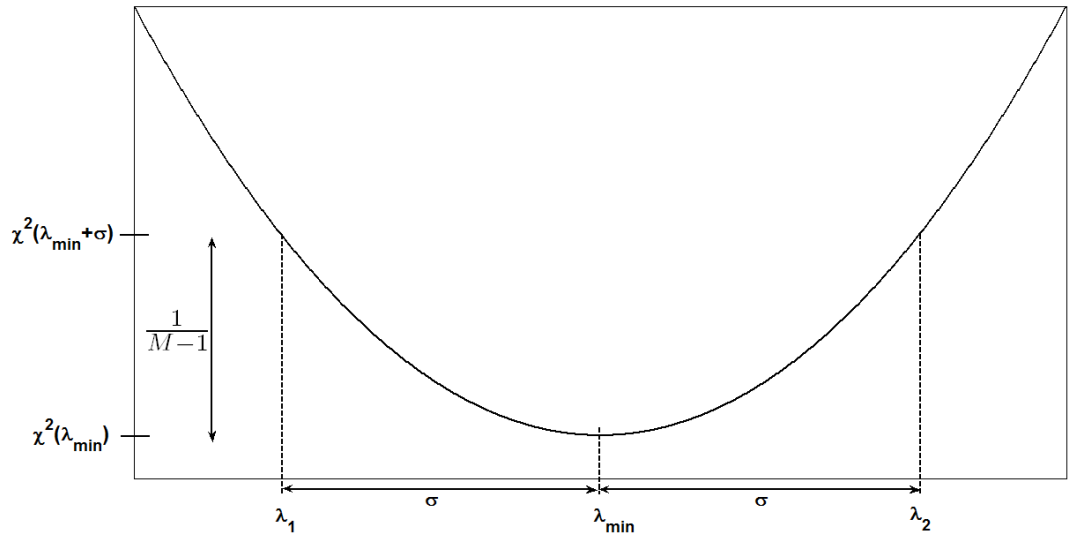

Figure 4.2: *Graphical illustration of the method used to estimate the uncertainty of λ_{min}.*

It is well-known that nuclear decay is governed by Poisson statistics [80, 81, 85], implying that the count rate is a measurement of the mean count rate, $N = \overline{N}$, with standard deviation:

$$\sigma_N = \sqrt{\overline{N}}, \tag{4.15}$$

and variance:

$$var(N) = \sigma_N^2 = N. \tag{4.16}$$

The relative uncertainty is determined by [85]:

$$\frac{\sigma_N}{N} = \frac{1}{\sqrt{N}}, \tag{4.17}$$

therefore high precision can be obtained with high statistics. By counting for longer, higher statistics can be obtained, thereby reducing the statistical uncertainty.

Systematic uncertainties on the other hand depend on the measuring equipment and the analysis method. Commonly, in an energy spectrum a fit is made to a peak and the continuum under the peak to determine the net-peak count rate. Various software exist with which net-peak count rates can be determined by fitting routines, but is heavily dependent on assumptions of the shape of the peak and continuum. Each assumption has its own effect on the result and also introduces systematic uncertainties of which the size is generally unknown. The analysis with the least assumptions, provided they are more or less correct, yields the lowest systematic uncertainty. For this work it is important that the statistical uncertainties do not exceed the systematic uncertainties. To reduce the effect of systematic uncertainties, fitting software was not employed. Instead a very simple net-peak area method was applied where by the continuum is estimated by an average continuum (also known as a linear continuum) and the peak area is determined by a direct summation of count rates per channel. This forms the basis for the Net-Peak Ratio Method which detects changes in branching ratios relative to changes in net-peak count rates. Uncertainties stated in this work are at 1σ.

4.3 Net-Peak Ratio Method

Different continuum shapes can result in different net-peak count rates and no method will be free from systematic uncertainties. The simplest shape is a linear continuum. The net-peak count rate is determined by setting three regions of interest; one over the peak ROI-P, one to the low-energy side ROI-L and one to the high-energy side ROI-H of the peak. These ROIs comprise N_{ch_L}, N_{ch_P} and N_{ch_H} number of channels in width, respectively. The continuum under the peak, N_c, is estimated from the average count rates in ROI-L and ROI-H and subsequently subtracted from the count rates of ROI-P to obtain the net-peak count rate:

$$N_c = \frac{N_{ch_P}}{2}\left(\frac{N_L}{N_{ch_L}} + \frac{N_H}{N_{ch_H}}\right), \tag{4.18}$$

where N_L and N_H are the count rates of ROI-L and ROI-H, respectively. The net-peak count rate N_P^{net} and its variance var(N_P^{net}) are given by:

$$N_P^{net} = N_P - N_c, \tag{4.19}$$

$$\mathrm{var}\left(N_P^{net}\right) = \mathrm{var}(N_P) + \left(\frac{N_{ch_P}}{2}\right)^2 \left(\frac{\mathrm{var}(N_L)}{N_{ch_L}} + \frac{\mathrm{var}(N_H)}{N_{ch_H}}\right). \tag{4.20}$$

The ratio of net-peak count rates is obtained by:

$$R = \frac{N_{P_1}^{net}}{N_{P_2}^{net}}, \tag{4.21}$$

with variance:

$$\mathrm{var}(R) = R^2 \left(\frac{\mathrm{var}\left(N_{P_1}^{net}\right)}{\left(N_{P_1}^{net}\right)^2} + \frac{\mathrm{var}\left(N_{P_2}^{net}\right)}{\left(N_{P_2}^{net}\right)^2}\right). \tag{4.22}$$

Figure 4.3 illustrates linear continua of varying size, applied to the asymmetric E_γ = 511 keV peak measured with a ^{22}Na source outside and inside a NaI(Tl)well counter.

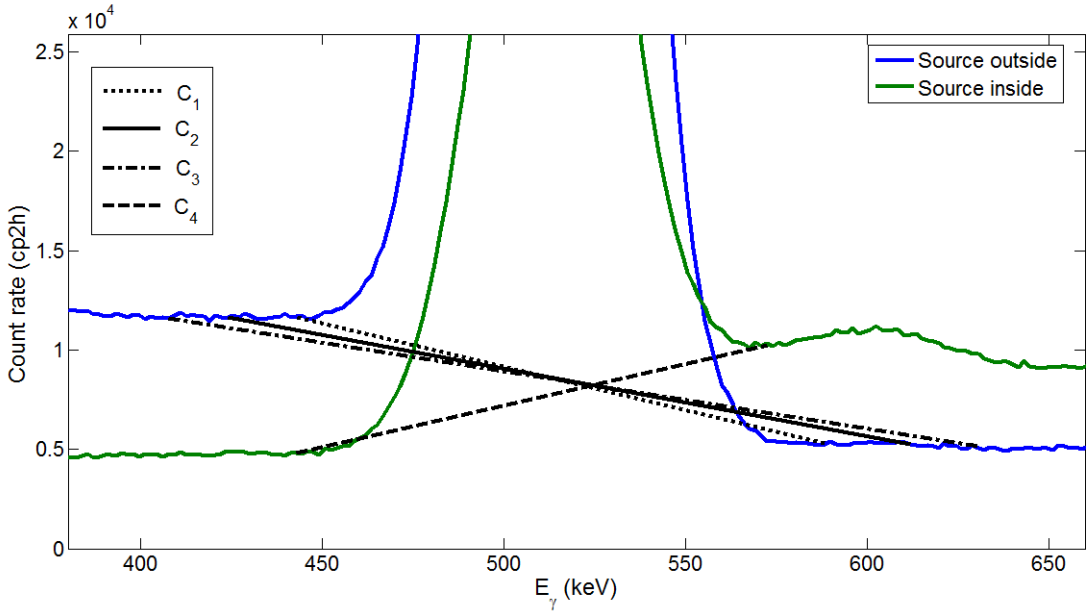

Figure 4.3: *Comparison of linear continua of varying size, applied to the E_γ = 511 keV peak measured with a ^{22}Na source outside and inside a NaI(Tl)well counter.*

Table 4.1 compares the net-peak count rates of the E_γ = 511 keV peak measured with the source outside the well-counter when the continua C_1, C_2 and C_3 are applied, where C_2 and C_3 have been extended by ten and twenty channels on both sides respectively, relative to C_1.

Table 4.1: *Net-peak count rate of the E_γ = 511 keV peak with the ^{22}Na source outside a NaI(Tl) well-counter, applying the three linear continua illustrated in Figure 4.3.*

	Net-peak count rate (cp2h)	% difference relative to C1
C1	3257000 (2000)	
C2	3223000 (2000)	1
C3	3188000 (2000)	2

Table 4.1 shows that the net-peak count rate of the E_γ = 511 keV peak after applying C_2 and C_3, decreases by 1% and 2% respectively, relative to C_1. This exercise shows that systematic uncertainties in determining net-peak count rates cannot be avoided and that the net-peak count rate is dependent on the choice and range of the function used to estimate the continuum. The true shape of the continuum is generally unknown and any estimation of the continuum shape introduces systematic uncertainties. This statement is justified by the decrease and increase of the continuum count rate on the low-and high energy side of the E_γ = 511 keV peak respectively when the source is measured inside the well counter, illustrated in Figure 4.3. This indicates that the continuum under a peak does not have a predetermined function that describes it.

4.3.1 Application to measurement series 1

For measurement series 1, applied to the BG subtracted average ^{22}Na spectra, the observed ratios of the net-peak count rates, $R_1 = \frac{N_{511}^{net}}{N_{1786}^{net}}$ and $R_2 = \frac{N_{1275}^{net}}{N_{1786}^{net}}$ can be expressed as:

$$R_1 = \left(1 + \frac{\beta_0}{\beta_1}\right)\frac{1}{\Omega\varepsilon_{1275}^F} - (1 + \alpha_{1275}) \tag{4.23}$$

and

$$R_2 = \frac{1 - \beta_0}{2\beta_1\Omega\varepsilon_{511}^F} - (1 + \alpha_{511}). \tag{4.24}$$

The ratios expressed by equations 4.23 and 4.24 are independent of the source activity and only functions of the branching ratios, detection efficiencies solid angle and possible pile-up.

Intermezzo 4.1: *Effects of pile-up on a spectrum*

Pile-up in a detector can affect peaks by increasing the peak width [84]. Pile-up is a function of count rate [89], therefore the effect will decrease for a decaying source, meaning that peak width will become smaller as the source decays. Consequently, pile-up can lead to inaccurate BG corrections and net-peak count rate estimations which are dependent on fixed regions of interest. Therefore, pile-up is also a source of systematic uncertainty. If no effects of pile-up are present in a spectrum, or if the effect is minimal, equations 4.23 and 4.24 are valid. In the case of high counting statistics obtained with a detector such as the $LaBr_3(Ce)$ detector used in this work, peak broadening of two channels does not affect net-peak count rate estimations. As an example table 4.2 provides the net-peak count rate of the E_γ = 1275 keV peak before and after ROI-P is decreased by two channels, by shifting ROI-L and ROI-H by one channel toward the peak.

Table 4.2: *Net-peak count rate of the E_γ = 1275 keV before and after decreasing ROI-P by two channels.*

	Net-peak count rate (cph)
Before	477330 (50)
After	477350 (50)

Table 4.2 shows that the net-peak count rate of the E_γ = 1275 keV peak is not affected by a two channel variation in peak width and will therefore not be affected by pile-effects of the same size.

Assuming that the source-detector geometry does not change as a function of time, the ratios should be constant through all periods of measurements and independent of changes in antineutrino flux. Since $\beta_0 \ll \beta_1$ the ratio R_2 is much more sensitive to changes in the branching ratio, β_1, than the ratio R_1. If β_1 is affected by some process it will manifest as a change in the magnitude of R_2. The insensitivity of R_1 to changes in the branching ratio can be used to correct for changes in the solid angle (source-detector geometry) that might have occurred as the source was moved to different locations. The detection efficiency ratios for the first measurement series have been estimated through Monte Carlo simulations (MCNPX): $\alpha_{511} = 0.781$ and $\alpha_{1275} = 1.81$.

To relate a change in R_2,ΔR_2, from reactor-on to reactor-off to a change in β_1, $\Delta\beta_1$, equation 4.24 is expressed as:

$$R_2 = \frac{a}{\beta_1} - b, \tag{4.25}$$

where $a = \frac{1-\beta_0}{2\Omega\varepsilon_{511}^F} = (R_2 + b)\beta_1$ and $b = (1 + \alpha_{511})$.

The derivative of R_2 w.r.t β_1 becomes:

$$\frac{\partial R_2}{\partial \beta_1} = -\frac{a}{\beta_1^2}, \tag{4.26}$$

or equivalently:

$$\Delta\beta_1 = -\frac{\beta_1^2}{a}\Delta R_2. \tag{4.27}$$

The value of *a* is obtained from R_2 from the control measurement at iTL which incorporates a change in solid angle and efficiency between Koeberg and iTL. At iTL the source was placed back relative to the detector to match the geometry at Koeberg as close as possible. The change in source-detector position is of the order of a millimeter compared to the 76.2 mm diameter of the $LaBr_3$(Ce) detector. The small systematic uncertainty can be corrected for by *a* and comparison of R_1 at the two locations with reactor-off and zero-antineutrino flux respectively.

4.4 Summary

Chapter 4 describes the methods used to analyse γ-ray spectra. The algorithm to adjust spectra for gain-drift, so called spectrum stabilisation is described. An introduction to uncertainties and uncertainty propagation related to measurements and analyses is provided. The net-peak ratio method is described and it is shown that a linear continuum subtraction introduces the least systematic uncertainties. It was also shown that pile-up does appear to have a significant effect on the net-peak count rates.

CHAPTER 5 Measurement series 1: $LaBr_3(Ce)$ detector

To test the hypothesis that antineutrinos affect nuclear β^+-decay rates, a source of antineutrinos, a β^+-source and a γ-ray detector are needed. Fortunately, anthropogenic sources of antineutrinos are available in the form of nuclear fission reactors. In April 2011 access was granted to the Koeberg nuclear power station (photograph shown in Figure 5.1) in the Western Cape, South Africa where electricity is generated by two 2.7 GW_{th} reactors.

Figure 5.1: *A photograph of the Koeberg nuclear power station with reactor unit#1 on the right and unit#2 on the left [84].*

The Koeberg nuclear power station operates according to a ten year production plan entailing predetermined shut down and start up dates for both units. Operating cycles may last for fifteen to eighteen months. Scheduled outages may last for thirty to eighty days, during which routine maintenance and refuelling occurs. Outages are scheduled such that either one of the units is always operating while the other experiences an outage. The ten year production plan allows measurements (such as in this work) to be carried out only during specific periods of time when a reactor makes the transition from on to off or vice versa, therefore measurements at reactors requires patience and a certain resignation to circumstances as well as a long term outlook to collecting data. An unscheduled shut down would also provide the opportunity to carry out a measurement, while the reactor is in outage and later started up again.

Comparing γ-ray spectra of ^{22}Na during reactor-on and-off periods, with changing antineutrino flux, could provide a method to detect changes in the decay constant. The following three chapters describe the equipment and set-up used, measuring process as well as the experimental results of three such series of measurements respectively.

This chapter describes measurement series 1, which was carried out outside the containment wall of unit#2 using a $LaBr_3(Ce)$ detector while unit#2 made the transition from off to on.

5.1 Properties of ^{22}Na

Figure 5.3 shows the decay scheme of ^{22}Na.The ground state of radionuclide ^{22}Na has a half-life of $t_{1/2}$ = 2.6027 y (10) [1] and decays 0.056% by β^+-decay directly to the ground state, ^{22}Ne(0), and 90.33% by β^+-decay to the first excited state, ^{22}Ne(1), of ^{22}Ne. Decay to the first excited state also proceeds 9.62% through electron capture (EC) as indicated in Figure 5.2. De-excitation of ^{22}Ne(1) results in the emission of a E_γ = 1275 keV γ-ray, β^+-annihilation produces two counter propagating E_γ = 511 keV annihilation photons.

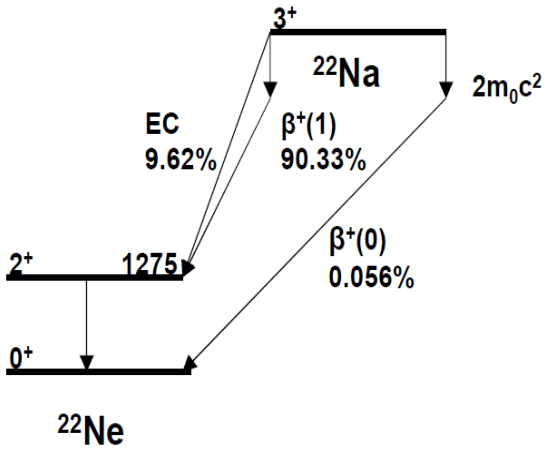

Figure 5.2: *Decay scheme of ^{22}Na.*

5.2 $LaBr_3$(Ce) detector properties

Courtesy of the European Space Agency, a 3"×3" $LaBr_3$(Ce) scintillation detector was obtained on loan for the duration of measurement series 1. The detector was manufactured by Saint Gobain, of the BrilLianCe 380 type. $LaBr_3$(Ce) detectors were invented in 2001 at Delft University of Technology and the University of Bern [90] and have a number of favourable characteristics. Compared to CsI and NaI detectors, these detectors have superior energy resolution of 3% at E_γ = 662 keV (Cs), high internal efficiency, high light yield (60 000 photons/MeV), high density (5.29 g/cm^3) and high flame point of 783 °C [90, 91]. A disadvantage of this detector and all inorganic scintillators is that they are hygroscopic [90]. Unlike High Purity Germanium (HPGe) detectors they do not have to be cooled to LN_2 (liquid nitrogen) temperatures. The typical timing resolution is ~ 200 ps depending on the detector size and the light decay-time constant is ~ 35 ns [90]. The self-activity caused by the decay of the naturally radioactive Lanthanum isotope, ^{138}La, might be considered to be a disadvantage as it contributes to intrinsic background with an approximate activity of 500 Bq for the above mentioned crystal size.

The radionuclide ^{138}La has two decay modes as illustrated in Figure 5.3:

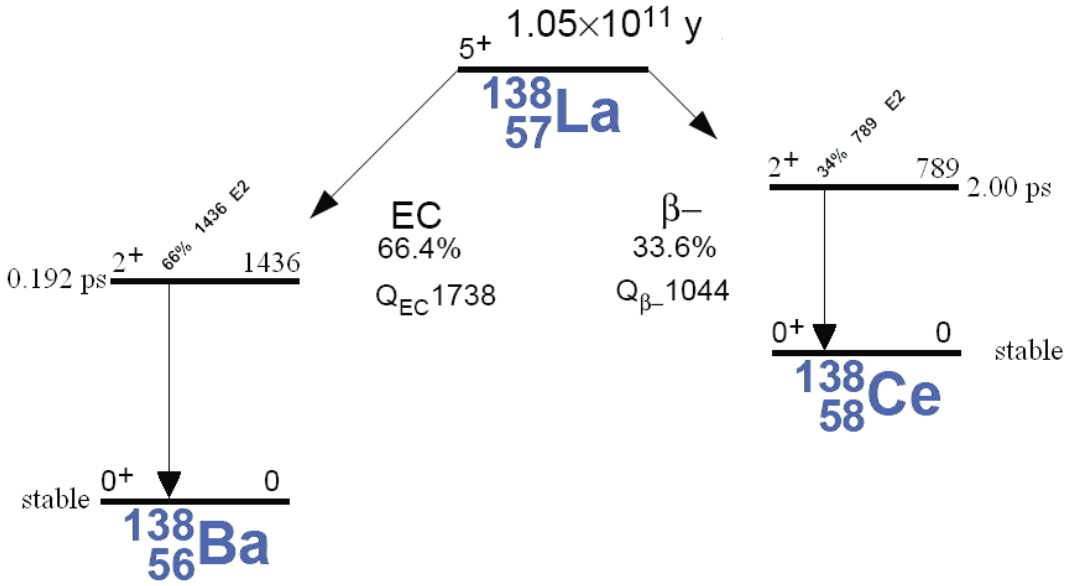

Figure 5.3: *Decay scheme of ^{138}La [92].*

one branch, comprising 66.4% of the decay proceeds through EC to the $J^{\pi} = 2^{+}$ state of ^{138}Ba, decaying by a E_{γ} = 1436 keV γ-ray to its ground state. Refilling of the unoccupied electron shells results in coincident emission of E_{γ} = 32 – 37 keV barium X-rays. Of the decay the remaining 33.6% populates the $J^{\pi} = 2^{+}$ state of ^{138}Ce via beta-minus (β^{-}) decay. This state subsequently decays to ^{138}Ce(0) by the emission of a E_{γ} = 789 keV γ-ray.

The intrinsic detector background can be considered to be constant due to the short four month period of the measurement compared to the $t_{1/2} = 1.02\times10^{11}$ y half-life of ^{138}La [1]. Intrinsic detector background is an internal source to the detector; no outside effects such as temperature and air pressure play a role. The detector background also contains alpha-contaminants (α) from the decay chain of ^{227}Ac which has a half-life of $t_{1/2}$ = 21.772 y [1].

Lanthanum is a silvery white element primarily obtained from monazite ores. Monazite ores are composed of a combination of the elements La, Ce, Th, Nd, Pr and Y. The presence of ^{227}Ac monazite ores is not unexpected because it is part of the decay chain of ^{235}U which is also present in the ores [93]. Due to the very similar chemical and physical properties of lanthanum and actinium, their separation is too costly and difficult and would make these detectors even more expensive.

An intrinsic detector-plus room background spectrum (BG) is presented in Figure 5.4 in blue, together with a ^{22}Na (Na+BG) spectrum in green.

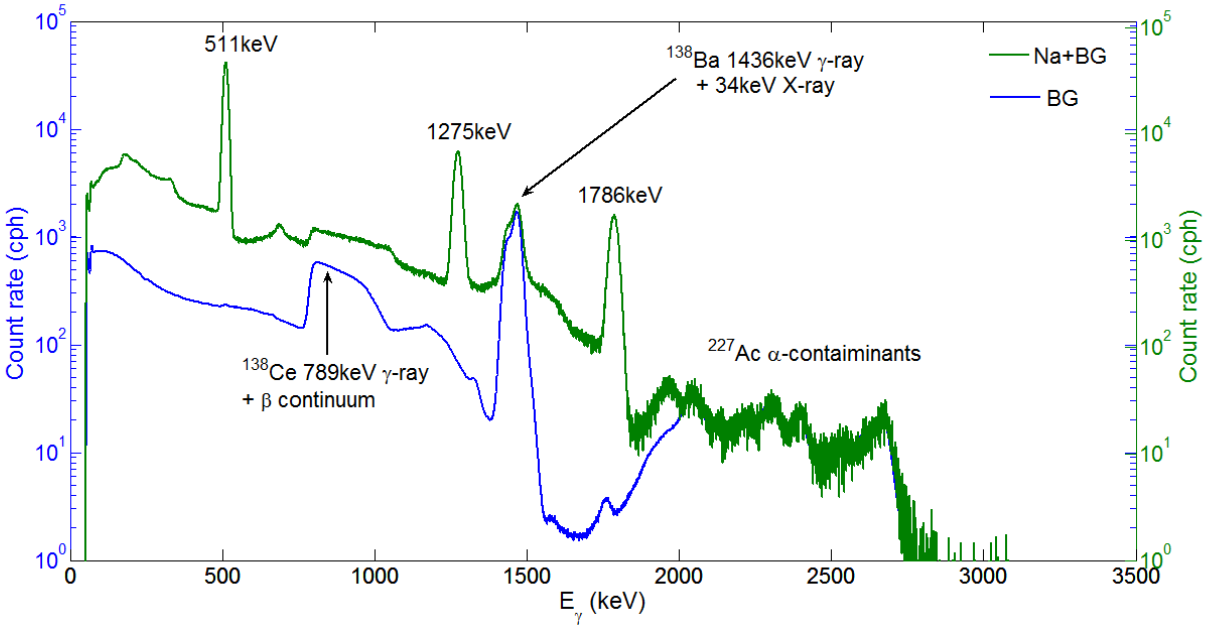

Figure 5.4: *Intrinsic background of a $LaBr_3$(Ce) detector, placed inside a lead shield, illustrated in blue, and a Na+BG spectrum illustrated in green.*

The Na+BG spectrum exhibits in addition to the BG features coincident summing effects due to the ^{22}Na source being placed onto the front side of the detector. Coincident summing occurs because, due to the short lifetime of the first excited state of ^{22}Ne(1), t ~ 5.9 ps, compared to the timing resolution of detector, a E_γ = 511 keV annihilation photon and the E_γ = 1275 keV γ-ray resulting from β^+-decay are detected within the time resolution of the detector and hence the signals will be summed. This effect leads to a sum peak at E_γ = 1786 keV and extends all the way up to 2 MeV due to triple coincidence involving the fore mentioned summing and in addition the second annihilation photon backscattered in the lead shielding.

5.3 Experimental set-up

At the Koeberg nuclear power station equipment was set-up in a passage next to the outside of the containment wall of unit#2, approximately l = 23 and 66 m from the centre of the cores of unit#2 and unit#1, respectively. This was the closest allowable position to the core of unit#2 at that time. The air temperature in the passage fluctuated above room temperature.

Figure 5.5 shows a photograph of the set-up used at Koeberg. The $LaBr_3(Ce)$ detector was shielded from room background with a low-activity lead cylinder with a wall thickness of d = 9.2 cm and a 12 mm thick inner copper lining. From one side of the lead cylinder the detector and from the other side the source holder could be inserted. The source holder contained two ^{22}Na sources with an activity of A ~ 2 kBq each, manufactured at the Radionuclide Division of the National Research Foundation iThemba Laboratory for Accelerator Based Science (NRF iThemba LABS) on 13/04/2011. The source-holder side was closed off with a lead lid. Due to the high-voltage base and pre-amplifier of the detector protruding from the lead cylinder on the opposite side, a 20 cm wide gap remained between the cylinder and the back lid. A trolley and cage were used to transport, house and protect the equipment from human interference while in operation.

Figure 5.5: *Set-up and equipment at iTL used during the first measurement series.*

The $LaBr_3(Ce)$ detector has a built-in pre-amplifier which was connected to an ORTEC 572 spectroscopy amplifier, powered by a NIM-bin. An operating voltage of V_{bias} = +560 V was applied to the detector using an ORTEC 556 high-voltage power supply. The signal from the pre-amplifier was fed into the ORTEC 671 spectroscopy amplifier with a shaping time of τ_s = 0.5 µs. The baseline restoration (BLR) was set on "auto". The signal from the amplifier was received by the data-acquisition system which consisted of an ATOMKI palmtop MCA (8k-01) and a laptop. The ATOMKI MCA was powered from the laptop via a USB cable. To be able to correct for and minimize the effect of gain-drift, γ-ray spectra of 8192 channels were recorded and stored on the laptop hard drive at ten-minute intervals. The MCA stored spectra according to the date and time that the run was started as well as the spectrum number. In the off-line analyses the spectra were inspected, gain-matched and subsequently grouped into one-hour spectra.

5.4 Measurement description

The measurement started on 13/04/2011 while unit#2 was in a scheduled outage for maintenance and refuelling while unit#1 was operating at full-power. Background was measured until 26/04/2011 after which the ^{22}Na (Na+BG) source was inserted and measured until 09/06/2011. On 14/05/2011 unit#1 experienced an unscheduled shut down for approximately seventeen hours before being powered-up again and reaching full-power on 16/05/2011. On 18/05/2011 unit#2 was powered-up reaching full-power on 27/05/2011.

Most unfortunately, during the power-up of unit#2 the spectroscopy amplifier started to malfunction and eventually broke down, causing some loss of data. On 14/06/2011 the ORTEC 572 amplifier was replaced with a CAEN N968 spectroscopy amplifier using the same settings as the ORTEC amplifier. While both reactors were operating at full-power, Na+BG measurements continued with the CAEN amplifier until 30/06/2011 after which a final BG measurement was made until 29/07/2011.

Prior to the measurement at Koeberg the detector was installed at iThemba LABS (iTL) to optimize the set-up. After the Koeberg measurement the detector was moved back to iTL to make control measurements using the CAEN amplifier. Table 5.1 provides a summary of the number of one-hour BG and Na+BG spectra measured with each of the amplifiers respectively during the various phases of operation of unit#2.

Table 5.1: *Summary of the quantity of data recorded during various phases of reactor operation of unit#2 in 2011.*

Location	Date	Amplifier	Number of one-hour spectra	Type of spectrum	Power level of unit#2 (% of maximum)
Koeberg	13/04 - 26/04	ORTEC	234	BG	0
Koeberg	26/04 – 18/05	ORTEC	309	Na+BG	0
Koeberg	18/05 – 21/05	ORTEC	78	Na+BG	25
Koeberg	25/05 – 26/05	ORTEC	10	Na+BG	90
Koeberg	02/06 – 03/06	ORTEC	29	Na+BG	90
Koeberg	14/06 – 30/06	CAEN	329	Na+BG	100
Koeberg	30/06 - 29/07	CAEN	324	BG	100
iTL	29/07 – 08/08	CAEN	233	BG	N/A
iTL	08/08 – 18/08	CAEN	163	Na+BG	N/A

A total of 234 one-hour BG spectra and 309 Na+BG spectra were obtained with the ORTEC amplifier while unit#2 was off. Another 78 Na+BG spectra were obtained while unit#2 operated at 25% of full-power. After 21 May 2011 the ORTEC amplifier started to break-down, allowing only 10 and 29 Na+BG spectra to be salvaged while unit#2 operated at 90% of full-power, respectively. With the CAEN amplifier a total of 324 Na+BG spectra and 324 BG spectra were obtained while unit#2 operated at full-power. For the control measurement with the CAEN amplifier at iTL 233 BG spectra and 163 Na+BG spectra were obtained.

5.5 Reliability of the data acquisition system

The high air temperature associated with the measurement venue, as well as the replacement of the ORTEC amplifier prompted an investigation into the performance of the electronics and quality of the data recorded which can provide an estimation of systematic uncertainties. It is well documented that the performance of PMT's can be affected by changes in temperature, fatigue, hysteresis and changes in count rates all of which can lead to gain-drift [81, 94, 95]. Other factors such as instabilities in the high voltage and electronics associated with the data acquisition system as well as the dependency of the light output of a scintillator on temperature can also lead to gain changes [80, 81, 96, 97, 98, 99, 100, 101]. All these factors predominantly may affect the shape of the spectra, but not necessarily the net-peak contents.

As a first priority the effect of gain changes on the data was investigated. Gain changes causing a continuous change in peak position is called drift, whereas a sudden change in the peak position is called a shift. Figure 5.6 shows the peak channel positions of the E_γ = 511, 1275, 1470 and 1786 keV peaks in the ten-minute spectra during the various measuring periods as a function of time.

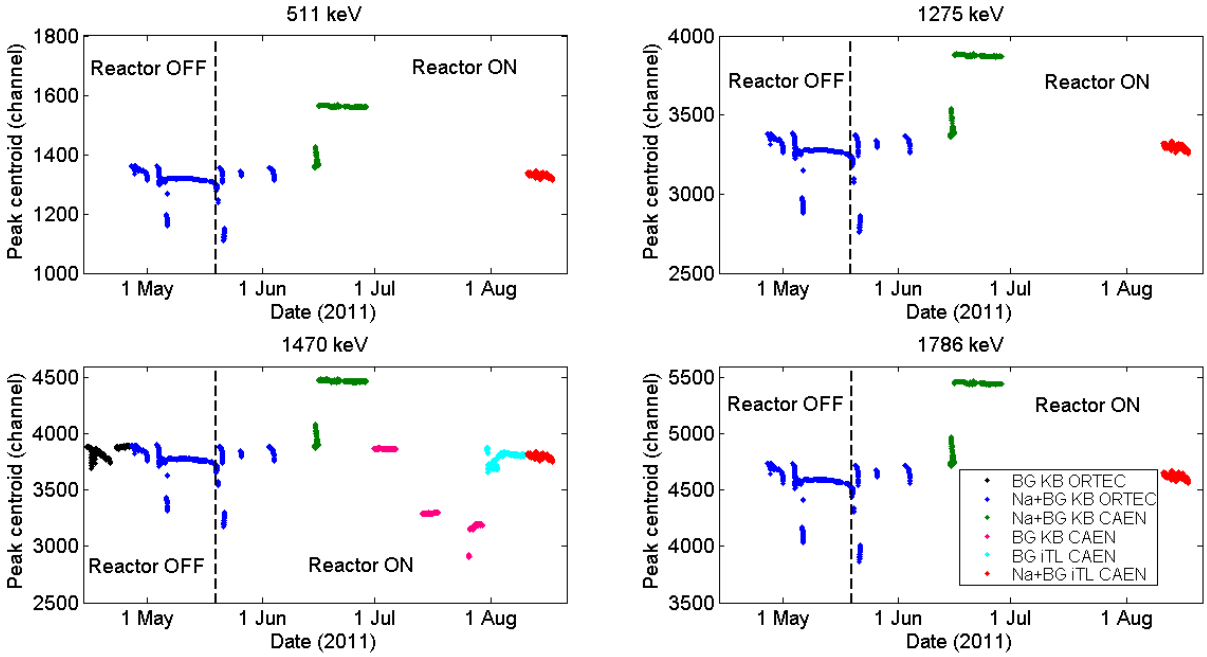

Figure 5.6: *Peak centroid positions in energy spectra measured with the $LaBr_3(Ce)$ detector. The figure illustrates the drift experienced by the E_γ = 511, 1275, 1470 and 1786 keV peaks in the ten-minute spectra. Off and on periods of unit#2 are indicated by the dashed lines.*

Though short periods of stability are experienced during all measuring periods, the most obvious and abrupt/extreme drift appears in the Na+BG spectra measured with the ORTEC amplifier between 1 May and 1 June 2011 where a shift of approximately 16% occurs. The BG with the ORTEC amplifier experiences a 5% shift. The Na+BG spectra measured with the CAEN amplifier show an abrupt change of approximately 10% in the peak centroid position on approximately 15 June 2011 whereas the BG spectra show a shift of approximately 25% between 1 July and 1 August 2011. Extreme changes in gain are known to be caused by sudden changes in count rates [81, 95]. Since the gain shift is not continuous and no sudden changes in count rate are experienced during Na+BG measurements this effect can be excluded as a cause of gain shift.

The effect of air temperature variations in the range of T = -5 to 45 °C on $LaBr_3(Ce)$ detectors has been investigated by R. Casanovas *et al.* [102] and found that a room temperature change of T = 25 to 45 °C resulted in a gain drift of approximately 16% toward the low-energy side. Because the response of $LaBr_3(Ce)$ was found to be fairly stable with temperature [103], gain changes could be caused by the PMT. Since the air temperature at the measurement venue was not constant or controlled the PMT sensitivity to temperature changes could be one factor causing gain changes. The other possibility for causing gain-shifts and-drifts is an unstable high voltage power supply. It can be argued that the gain-drift starting on 14 June 2011 (seen as a short, sharp rise) after installing the CAEN amplifier and the gain drift starting on 1 August 2011 (seen as a short, sharp dip, then increasing to the starting level) after starting the BG measurement at iTL are due to the high voltage power supply and PMT stabilising after a period of inactivity. After this period of stabilising the gain becomes more stable and continues to vary around a mean value. The exact cause of the gain changes is not known and might be due to a combination of different factors.

Figure 5.7 shows an example of how gain changes, represented by the E_γ = 511 keV peak drift in blue, affect the total count rate of Na+BG spectra, in green, as a function of time.

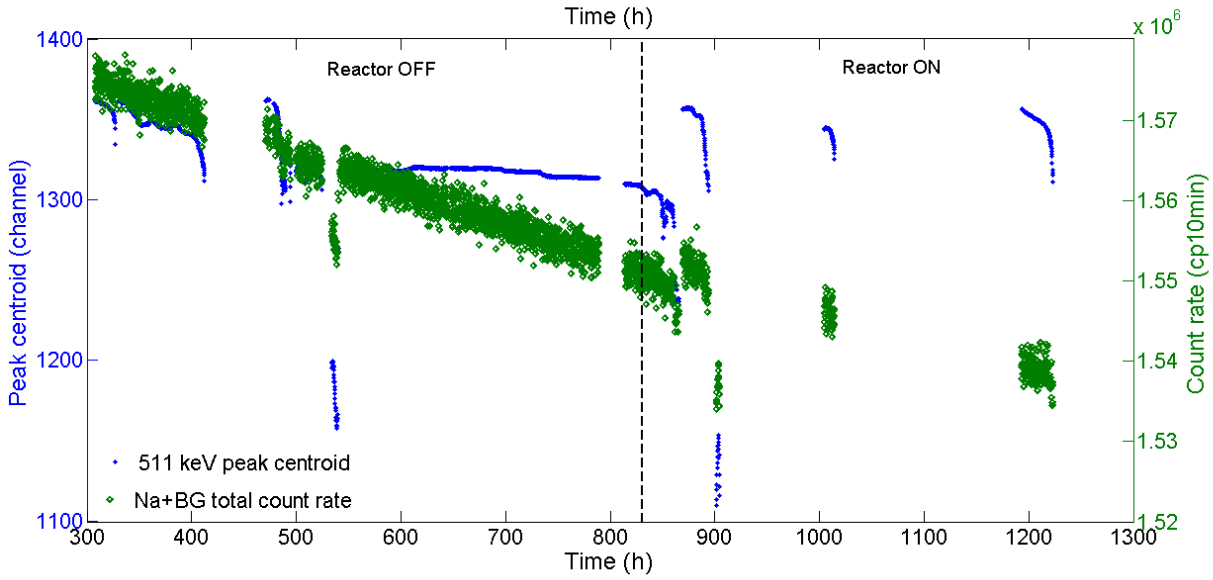

Figure 5.7: *The effect of gain drift on the total count rate of spectra. As an example the ORTEC data is used. The E_γ = 511 keV peak channel position is on the left hand axis (blue) and the total count rate in the spectra is on the right hand axis (green). The time is relative to the start of the BG measurement on 13/04/2011 and is given in hours to simplify the following discussion.*

Figure 5.7 illustrates the correlation between gain drift and total count rates in the ten-minute Na+BG spectra measured with the ORTEC amplifier. Gain drift toward the low-energy side causes a loss of counts below the threshold energy set on the MCA resulting in a decrease in the total count rate. Gain drift toward the high-energy side allows low energy counts to fall above the threshold energy, causing an increase in the total count rate. An overall decrease in count rate occurs due to the decay of ^{22}Na but clear dips and jumps in count rate can be observed at about t = 530, 880 and 900 h where drastic gain changes occur. A peak shift of approximately 20% at t = 900 h leads to a change in the total count rate of approximately 1%. Because the ^{22}Na source is decaying, the effect of gain changes on net-peak count rates cannot be investigated by simply comparing count rates. Moreover, the gain shifts at t = 530, 880, 900, 1000 and 1200 h do not provide enough counting time to provide sufficient statistics to investigate possible changes in the ratio of net-peak count rates caused by gain changes.

Because gain changes alter the shape and size of pulses, the binning of pulses in the MCA will change which causes the energy calibration of spectra to change. When spectral analyses involve background subtraction and regions of interest it is important for spectra to have the same energy calibration. For this reason the BG and Na+BG spectra measured with both amplifiers were spectrum-stabilised to match a single energy calibration as close as possible. In intermezzo 5.1 the effects of multiplicative and additive gain changes are discussed as a possible cause for the mismatch of peak positions even after spectrum-stabilisation.

Intermezzo 5.1: *Effect of multiplicative and additive gain changes*

The effect of multiplicative and additive gain on spectra is illustrated by figure 5.8, the top panel shows that the gain affected peaks, P_1 and P_2, should be multiplied by the same correction factor, x_2, to be shifted to the correct channel numbers c_1 and c_2 respectively. This is an example of multiplicative gain. The bottom panel shows an example where the gain experienced by P_1 and P_2 is not the same, with P_1 ending up at P_1' due to an additive term in the gain. Due to the additive term, P_1 and P_2 have to be multiplied by two different correction factors, x_2 and x_1 respectively. Applying a linear stabilisation using only one correction factor in the case where there is multiplicative as well as additive contributions to the gain would cause a misalignment of the peaks, i.e. if only the correction factor x_1 is

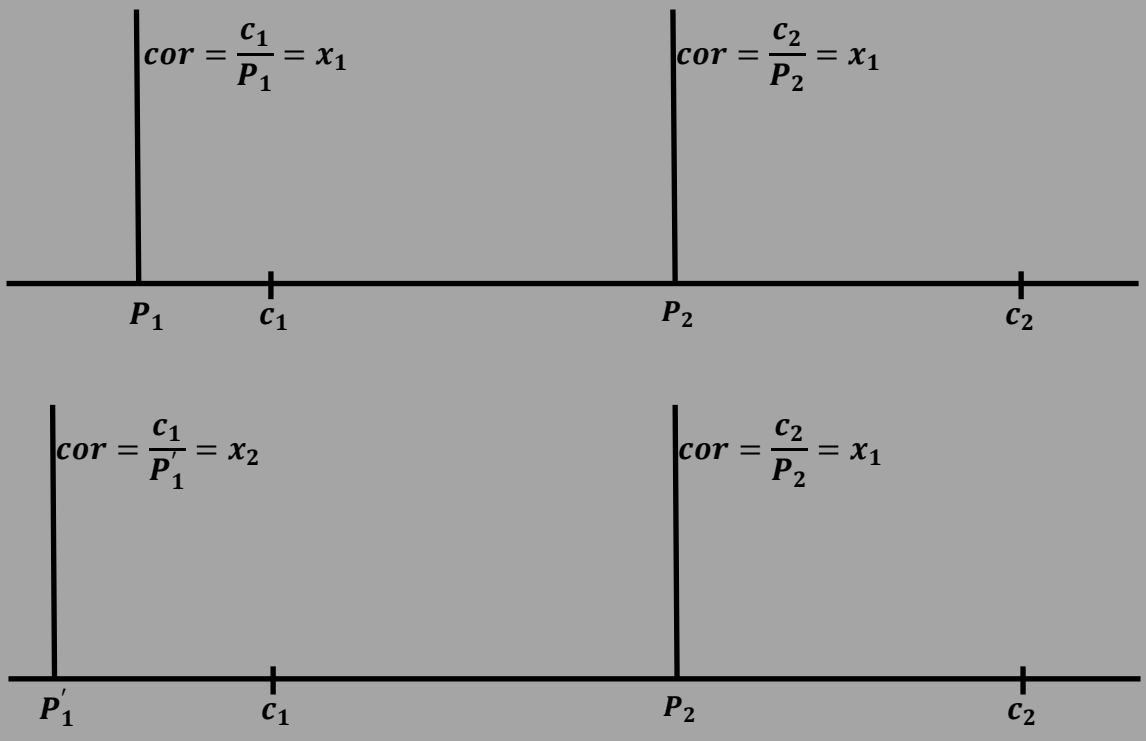

Figure 5.8: *Illustration of the effect of multiplicative and additive gain. c_1 And c_2 are the channels at which the peaks P_1 and P_2 should be after spectrum-stabilisation.*

is used to gain stabilize the peaks P_1 and P_2, only P_2 would end up at the correct channel number c_2. The misalignment of peaks can have an effect on the net-peak count rate due to the set ROIs which can exclude part of a peak and include part of the continuum, thus affecting the background and continuum subtraction. This is of course a source of systematic uncertainty and illustrates the importance of having real-time gain-stabilisation

software. Off-line spectrum-stabilization allows a spectrum to drift without a user-controllable limit, thus allowing a mixture of multiplicative and additive gain changes to take place. With real-time gain-stabilization spectra can be corrected more frequently (of the order of seconds to minutes, depending on the count rate under the peak which is used as a reference) thus minimizing the chance for mixed gain terms.

Figure 5.9 illustrates the effectiveness of the spectrum-stabilization procedure with all the peaks (of one-hour spectra) now lying inside one channel, except the E_γ = 1470 keV peak which varies approximately five channels.

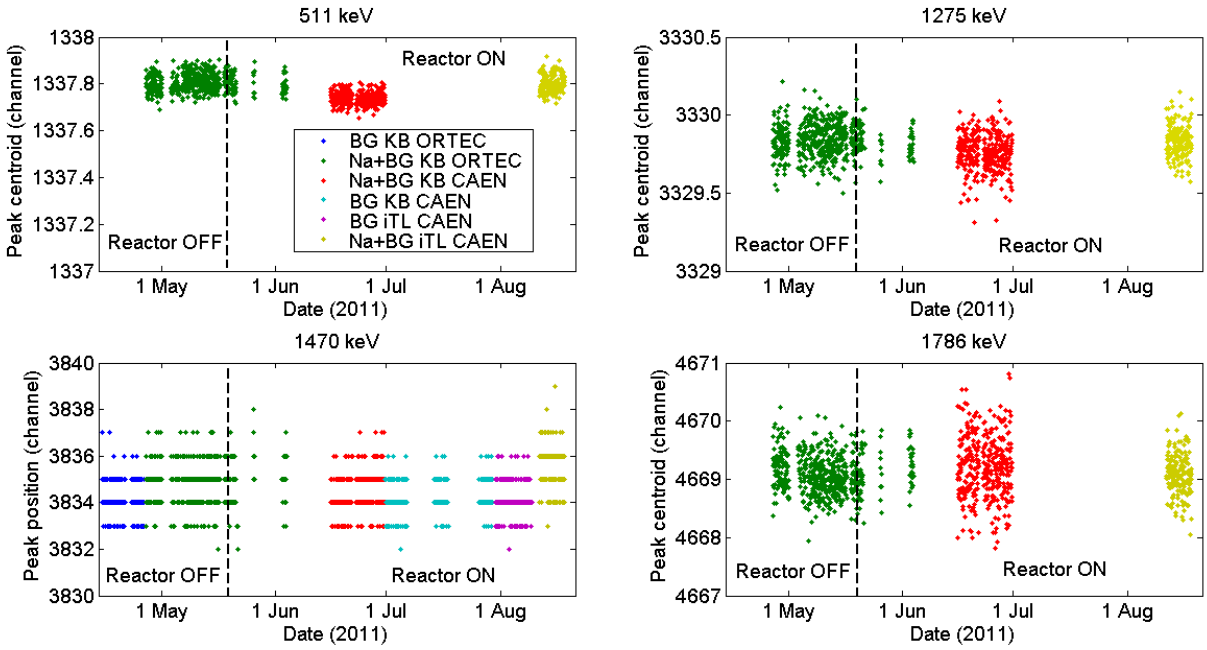

Figure 5.9: *Positions of the E_γ = 511, 1275, 1470 and 1786 keV peaks after spectrum-stabilisation of one-hour accumulated data.*

Periods where gaps in data occur are due to either spectra having to be discarded due to loss of spectral shape, or the acquisition reached its maximum number of cycles and could only be restarted by the designated person at Koeberg at a time which would not detract her from her own work. From 21 May 2011 the amplifier started to show signs of trouble via the MCA recording incomplete or empty spectra and also unrealistic spectral shapes. Fortunately short patches of usable spectra were salvaged. On 14 June 2011 the faulty ORTEC amplifier was replaced.

Figure 5.10 shows the alpha-contaminant region above E_γ = 2000 keV in the BG and Na+BG spectra measured with the ORTEC and CAEN amplifiers, after spectrum-stabilisation. A clear mismatch of α-peaks is visible in the BG as well as Na+BG spectra. The mismatch of α-peaks as well as the slight mismatch of the E_γ = 1470 keV peak can be attributed to a combination of multiplicative and additive gain experienced by these peaks. It is also known that the pulse shape of alpha particles change differently compared to γ-rays as a function of temperature/gain. Therefore, if the temperature outside the containment wall did in fact change it could explain the mismatch of α-peaks. Due to the mismatch of spectra above E_γ = 2000 keV and considering that the E_γ = 1786 keV peak is in close proximity to the α-region it was decided not to include analyses of spectra above the E_γ = 1786 keV peak. Also, because of the slight mismatch of the E_γ = 1470 keV peak in the Na+BG spectra, the accuracy of the BG subtraction in this region is reduced. Therefore, analyses of the ^{22}Na standard spectra in ROIs where the E_γ = 1470 keV peak was, were not included.

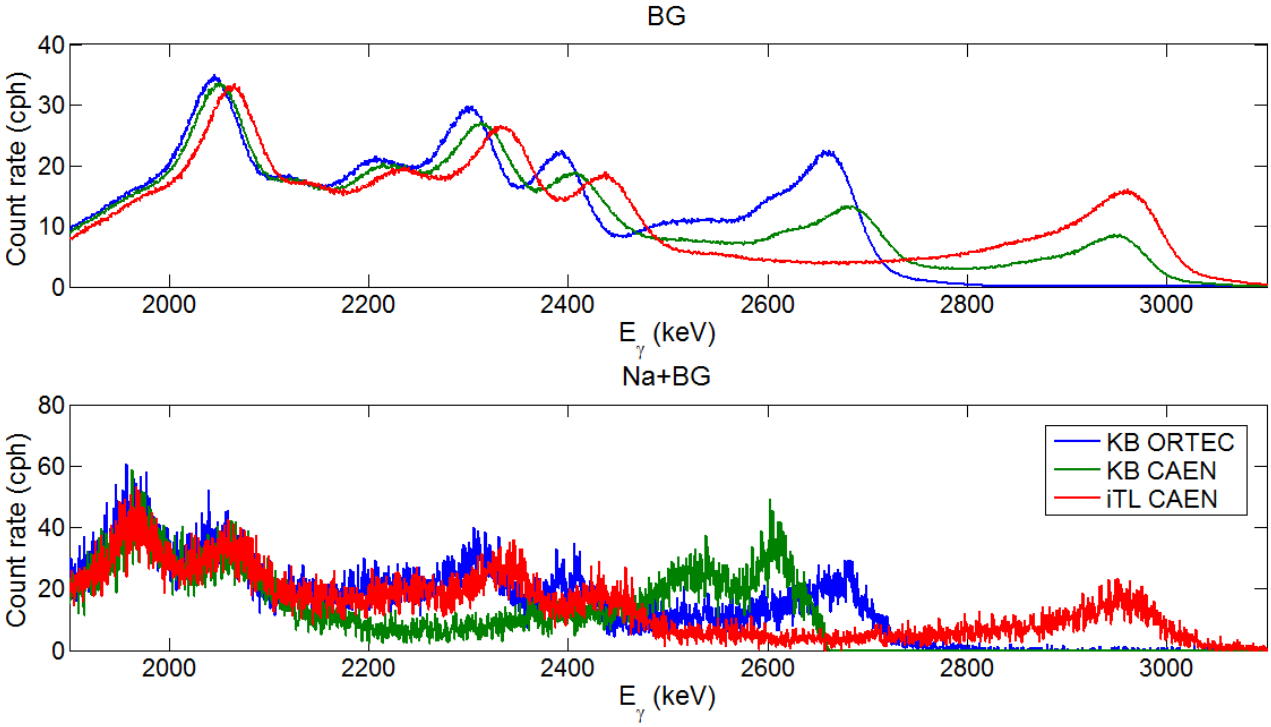

Figure 5.10: *Mismatch of α-peak region above E_γ = 1960 keV in the spectrum-stabilised BG (top panel) and Na+BG (bottom panel) spectra during reactor-off and-on and at iTL.*

Figure 5.11 shows a plot of the ratios of the peak positions R = $\frac{511\text{ keV}}{1275\text{ keV}}$, $\frac{511\text{ keV}}{1786\text{ keV}}$ and $\frac{1275\text{ keV}}{1786\text{ keV}}$ in the Na+BG spectra prior to spectrum-stabilisation, during the three measurement periods.

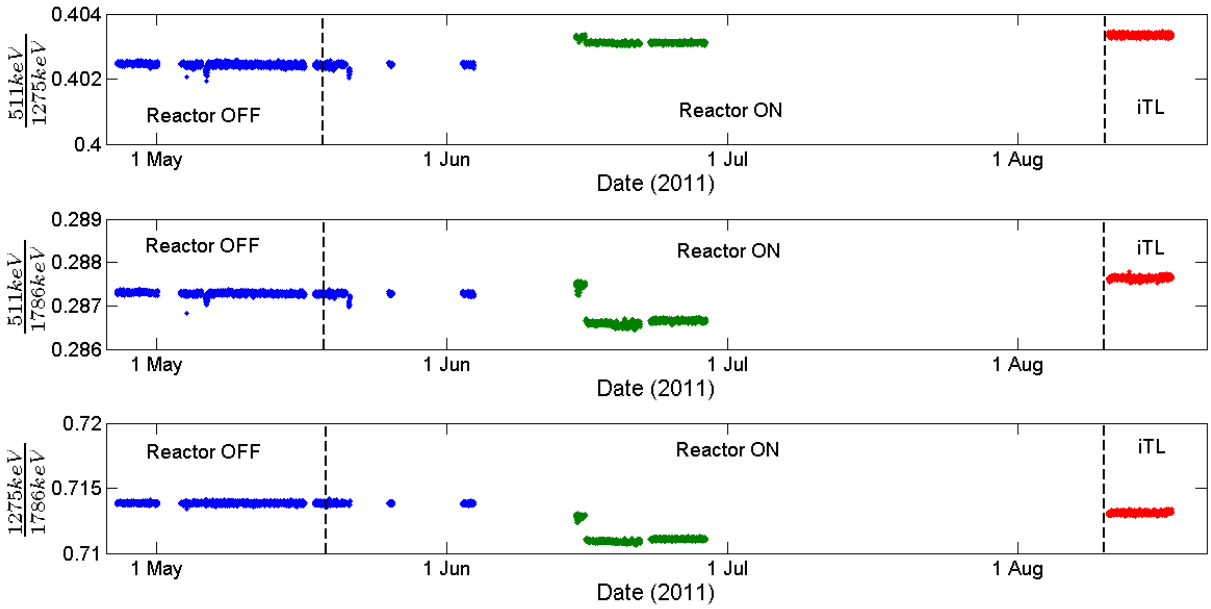

Figure 5.11: *Ratios of the peak positions* $R = \frac{511\ keV}{1275\ keV}, \frac{511\ keV}{1786\ keV}$ *and* $\frac{1275\ keV}{1786\ keV}$ *prior to spectrum-stabilisation of the Na+BG spectra, during reactor-off and-on and at iTL.*

The ratios plotted in Figure 5.11 show how the position of a peak changes relative to the other peaks during each measurement period respectively, which provides a way to observe multiplicative and additive gain changes. The sudden jump in peak ratios on 15 June 2011 during reactor-on indicates an additive gain component, after which the gain remains multiplicative. Besides the additive gain component observed on 15 June 2011 the gain remains multiplicative during each period respectively, though relative to the other, the gain during each period changes multiplicatively which causes a mismatch of the α-peaks.

After spectrum-stabilisation, the Na+BG spectra were checked for pile-up effects which most noticeably manifest as changes in peak widths. Figure 5.12 shows the standard deviations of the E_γ = 511, 1275 and 1786 keV peaks during the three periods where no significant changes in the standard deviations are observed, and it appears that the $LaBr_3$ detector is free from significant pile-up.

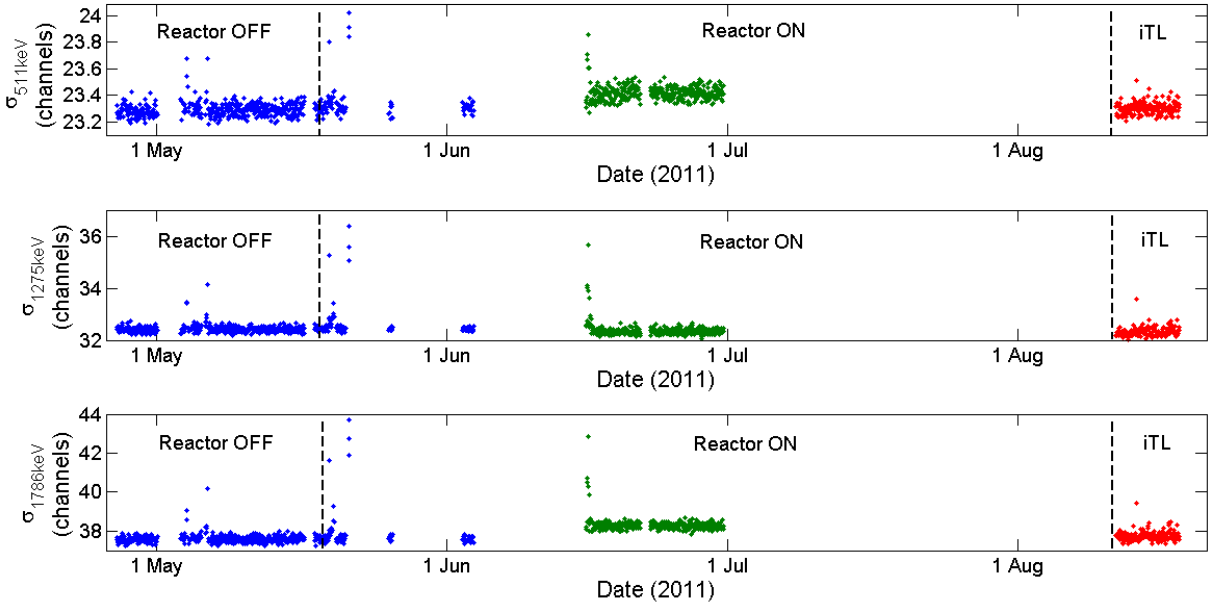

Figure 5.12: *Standard deviations of the E_γ = 511, 1275 and 1786 keV peaks after spectrum-stabilisation.*

The construction of ^{22}Na standard spectra are dependent on the subtraction of a BG standard spectrum, if the BG is not constant during the measuring period it can lead to the incorrect interpretation of results. Therefore it is important to investigate the BG as a function of time. Figure 5.13 compares the BG standard spectra measured during reactor-off, reactor-on and at iTL. Three small but distinct peaks can be seen in the BG standard spectra measured at Koeberg which are not present at all in the iTL BG standard spectra; one at E_γ = 662 keV due to the decay of ^{137}Cs and two peaks at E_γ = 1173 keV and 1333 keV due to the decay of ^{60}Co.

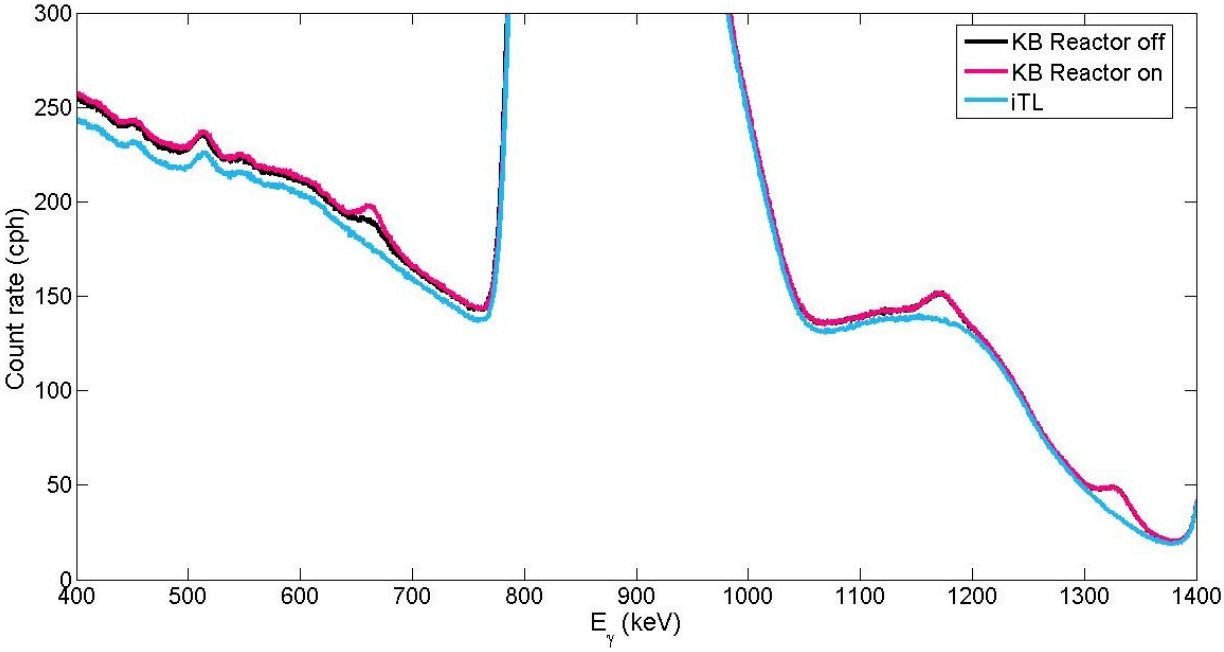

Figure 5.13: *Comparison of BG standard spectra measured during reactor-off and-on periods as well as at iTL in the energy range E_γ = 400 to 1400 keV.*

Also important is the behaviour of the total BG count rates during the three measurement periods. Figure 5.14 shows the hourly BG count rates in a wide ROI (called gate I) covering almost the full BG spectrum with 143 < E_γ < 1909 keV (excluding the α-peak region) during reactor-off and-on and at iTL, also indicated by the solid horizontal lines are the weighted means (wm) of the hourly count rates during each period respectively. From Figure 5.14 a clear increase in the count rate is observed during reactor-on and a decrease at iTL, relative to reactor-off. It is not surprising to find that the BG count rate has changed at iTL relative to Koeberg due to different room backgrounds. It is however odd that the BG count rates during reactor-off and-on are not constant since the position of the detector did not change at Koeberg. Table 5.2 provides the weighted mean (wm) of the hourly count rates during each period as well as the χ^2 relative to the weighted mean of the count rates. With χ^2-values of χ^2 = 1.08, 1.03 and 1.07 during reactor-off, -on and at iTL respectively it can be accepted that the count rate in gate I remains constant during each period respectively. During reactor-on the weighted mean count rate increases by approximately 0.6% whereas it decreases by approximately 2.7% at iTL, relative to reactor-off.

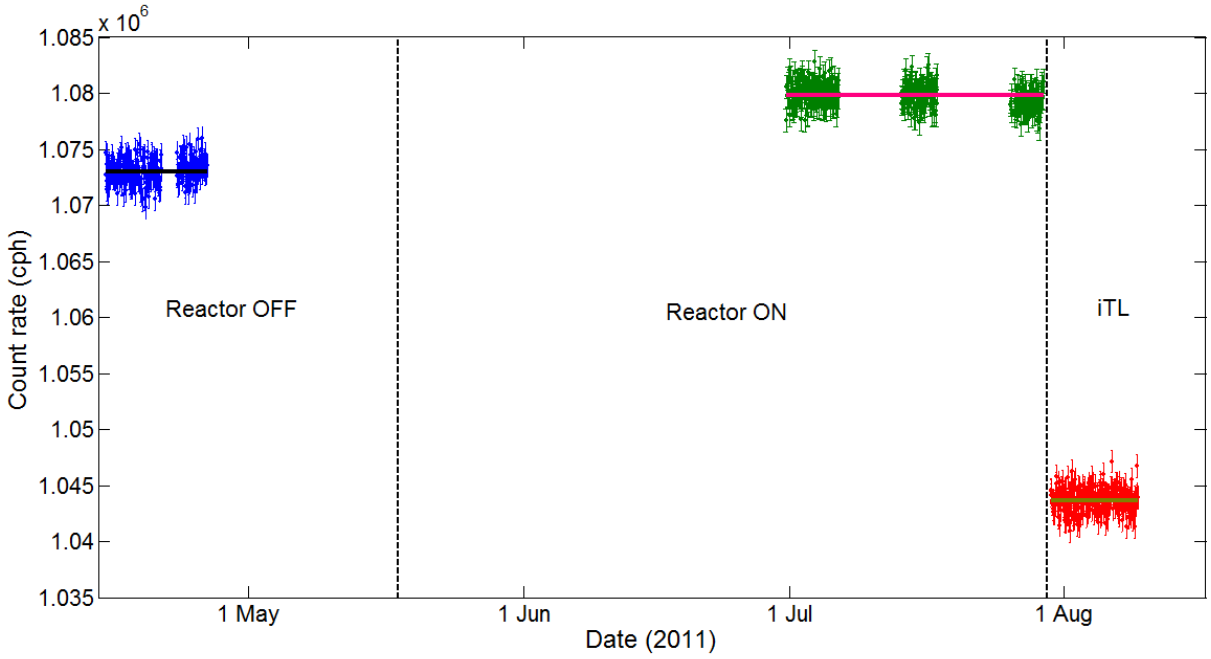

Figure 5.14: *Comparison of the hourly BG count rates in a wide ROI during reactor-off and-on as well as at iTL. The weighted mean during each period is also indicated by the solid horizontal lines.*

Table 5.2: *Counting statistics in gate I of the hourly BG spectra during reactor-off and-on as well as at iTL.*

Gate	Energy (keV)	Reactor-off		Reactor-on		iTL	
		wm (cph)	χ^2	wm (cph)	χ^2	wm (cph)	χ^2
I	$143 < E_\gamma < 1909$	1073040 (70)	1.08	1079780 (60)	1.03	1043670 (70)	1.07

By analysing the count rates in smaller ROIs in the BG standard spectra during reactor-off and-on, it was determined that the increase in the BG count rate during reactor-on was only experienced in the energy region $143 < E_\gamma < 1568$ keV (gate II). Table 5.3 provides the count rates in the BG standard spectra during reactor-off and-on in gate II as well as a third gate, gate III, with $1569 < E_\gamma < 1909$ keV. Figure 5.15 indicates the three gates in the BG spectra.

Table 5.3: *Counting statistics in gate II and III of the BG standard spectra during reactor-off and-on.*

Gate	Energy (keV)	Reactor-off	Reactor-on
II	$143 < E_\gamma < 1568$	1070060 (70)	1076800 (60)
III	$1569 < E_\gamma < 1909$	2980 (4)	2977 (3)

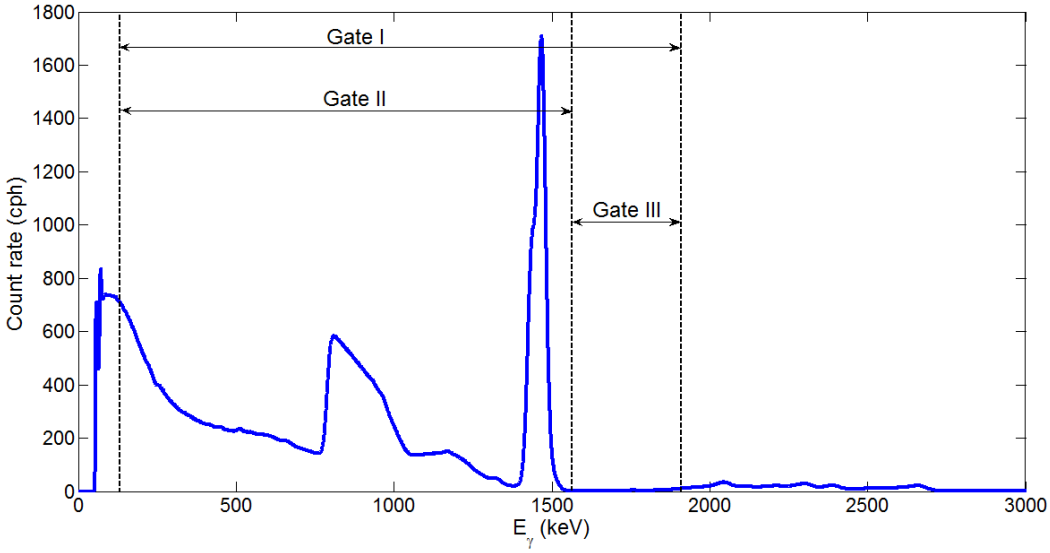

Figure 5.15: *A BG standard spectrum indicating the three gates used to investigate the BG count rates.*

From Table 5.3 an increase of approximately 0.6% in the count rate is also observed in gate II during reactor-on, confirming the 0.6% increase in gate I. The count rate in gate III remains constant to within the uncertainties during reactor-off and-on. Because the analysis employed in this work is dependent on net-peak count rates, the effect of the increased BG count rate on the net-peak count rates of the E_γ = 511, 662, 789, 1173, 1333 and 1470 keV peaks in the BG standard spectra was investigated. Table 5.4 provides the net-peak count rates of the above mentioned peaks after a linear continuum subtraction was applied.

Table 5.4: *Net-peak count rates of the E_γ = 511, 662, 1173, 1333 and 1470 keV peaks in the BG standard spectra during reactor-on and-off and at iTL.*

Energy (keV)	Reactor-off (cph)	Reactor-on (cph)	iTL (cph)
511	420 (30)	430 (20)	380 (30)
662	470 (30)	870 (20)	N/A
789	183325 (80)	183340 (70)	183390 (80)
1173	1620 (30)	1590 (20)	N/A
1333	532 (14)	518 (12)	N/A
1470	217220 (40)	217290 (30)	217780 (40)

Relative to the reactor-off phase, an increase of approximately 85% is observed in the net-peak count rate of the E_γ = 662 keV peak during reactor-on. In contrast, the net-peak count rates of the E_γ = 1173 and 1333 keV peaks remain constant within the uncertainties during reactor-on and-off periods. Naturally occurring ^{59}Co is present in Fe alloys used to reinforce buildings and structures. During reactor operation neutrons from the reactor can activate ^{60}Co through neutron absorption by ^{59}Co. ^{60}Co Has a half-life of $t_{1/2}$ = 5.271 y [1] which explains why it is present during reactor-off and-on periods. On the other hand, ^{137}Cs is a fission product with a half-life of $t_{1/2}$ = 30.9 y, but since the measurement was carried out within a radiation protection area it is unlikely that the E_γ = 662 keV peak is caused by the decay of ^{137}Cs produced in the core, therefore no straightforward explanation is available for this peak. Table 5.4 shows no significant increase in either of the net-peak count rates of the E_γ = 789 and 1470 keV peaks during reactor-on. Within the uncertainties the E_γ = 789 keV net-peak count rates are the same during all three periods, where as the E_γ = 1470 keV net-peak count rates are the same during reactor-off and-on only. The significant increase of the net-peak count rate of the E_γ = 1470 keV peak at iTL relative to reactor-off and-on is likely due to a larger amount of ^{40}K present in the concrete at iTL, the decay of which results in a E_γ = 1460 keV γ-ray which is inseparable from the E_γ = 1470 keV peak.

Table 5.4 also provides the net-peak count rate of the E_γ = 511 keV peak. Though the origin of this peak can come from many possible sources such as β^+-annihilation radiation from β^+-decays, cosmic muons that produce β^+-annihilation radiation in the detector and shielding, the pair production process caused by high energy cosmic γ-rays, nuclear decays or other nuclear reactions; it can be used to monitor BG spectra for changes in the flux of cosmic rays at the measurement location. Comparing the net-peak count rate of the E_γ = 511 keV peaks during reactor-off and-on periods in the average BG spectra, no change is observed to within the uncertainties. From these results it can be concluded that the γ-ray intensity induced by the cosmic ray flux does not change significantly between reactor-off and-on periods at the measurement location. The net-peak count rate of the E_γ = 511 keV peak at iTL decreased by approximately 11% compared with Koeberg due to the difference in room background.

According to the net-peak count rates of the E_γ = 511, 789, 1173, 1333 and 1470 keV peaks in Table 5.4, the increased BG count rate during reactor-on has no significant effect on the net-peak count rates of peaks in the BG spectra. Therefore it can be concluded that the increase in the BG count rate during reactor-on is not due to the reactor. Another possibility

is that the CAEN amplifier has different properties than the ORTEC amplifier, even though both had the same operating settings (in theory), causing an increase in the low energy count rate. It can also be concluded that the change of amplifiers as well as changes in gain have no effect on the properties of the BG spectra and especially the peaks related to the decay of ^{138}La.

5.6 Experimental Results

The goal of this project is to investigate possible changes in the decay constant of ^{22}Na induced by electron antineutrinos. Due to the intrinsic detector BG an opportunity to investigate changes in the decay constant of ^{138}La is also provided. Conventional methods for determining decay constants are by fitting an exponential through γ-ray count rates or intensity factors. Intensity factors describe the contribution of individual radionuclei to a spectrum containing a mixture a radionuclei. If the spectrum only contains contributions from one radionuclide such as ^{22}Na, the intensity factors $I_n(t)$ from BG subtracted Na+BG spectra S(t) as a function of time t can be determined relative to a BG subtracted average Na+BG spectrum $S(t_m)$ at the mean time t_m of the measurement through different methods such as the full-spectrum analysis, hybrid method or net-peak area method [84, 104, 105, 106], i.e. for the net-peak area method applied to ^{22}Na:

$$I(t) = \frac{S(t)}{S(t_m)}. \tag{5.1}$$

By correcting the intensity factors according to the literature value of the decay constant of ^{22}Na and fitting an exponential function to the intensity factors, the χ^2-minimization procedure described by equation 4.10 to 4.14 can be applied to determine the decay constant which best describes the decay of the intensity factors and radionuclide. As an example, Table 5.5 provides the decay constants calculated by applying the above mentioned procedure to the net-peak count rates of the E_γ = 511, 1275 and 1786 keV peaks in the average ^{22}Na spectra determined by a linear continuum subtraction. Also listed in Table 5.5 are the corresponding χ^2-values during reactor-off and-on and at iTL.

Table 5.5: *Calculated decay constants and corresponding χ^2-values of ^{22}Na using the net-peak count rates of the E_γ = 511, 1275 and 1786 keV peaks during reactor-off and-on and at iTL.*

Period	511 keV		1275 keV		1786 keV	
	λ ($\times 10^{-5}$ h^{-1})	χ^2	λ ($\times 10^{-5}$ h^{-1})	χ^2	λ ($\times 10^{-5}$ h^{-1})	χ^2
Reactor-off	3.05 (0.02)	1.33	3.01 (0.04)	1.17	2.96 (0.08)	1.01
Reactor-on	3.02 (0.05)	1.00	3.10 (0.11)	0.88	3.0 (0.2)	1.00
iTL	3.3 (0.2)	0.94	2.5 (0.4)	0.86	3.6 (0.6)	1.01

All the decay constants, excluding that of the E_γ = 1275 keV peak at iTL, calculated in Table 5.5 remain constant to within the uncertainties and are equal to the literature value of $\lambda(^{22}\text{Na})$ = 3.0381 (0.0012) $\times 10^{-5}$ h^{-1} [1]. This is supported by the χ^2-values which have P-values $\geq$ 0.95. It is evident from Table 5.5 that due to the low precision, this approach is not sensitive enough to detect changes in the decay constant. A relative measurement would be more suitable as the systematic uncertainties involved in calculating the decay constant are reduced. For this reason the analytical method described in section 4.3 is applied to ^{22}Na. Sections 5.6.1 and 5.6.2 present calculations for setting upper limits for the interaction of $\bar{\nu}_e$ with nuclei of ^{138}La and ^{22}Na respectively.

5.6.1 The effect of $\bar{\nu}_e$ on the decay rate of ^{138}La

In the case of ^{138}La which has a rather long half life of $t_{1/2} = 1.02\times10^{11}$ y [1] compared to the measurement time of BG during reactor-off and-on, it is expected that the count rate of the intrinsic detector BG remains constant during reactor-off and-on. Conveniently the decay of ^{138}La results in two peaks at E_γ = 789 and 1470 keV with net-peak count rate contributions coming from purely β^--decay and electron capture respectively, assuming that the contribution from the decay of ^{40}K which has a half-life of $t_{1/2} = 1.248\times10^9$ y [1] remains constant. Therefore the net-peak count rates of the E_γ = 789 and 1470 keV peaks should remain constant during reactor-off and-on and provide a direct measure of changes in the β^- and EC branching ratios P_i which are related to the partial decay constants λ_i through:

$$P_i = \frac{\lambda_i}{\lambda}, \tag{5.2}$$

where λ is the total decay constant:

$$\lambda = \sum_i \lambda_i \,, \tag{5.3}$$

and $i = \beta^-$, EC. From equations 5.2 and 5.3 it can be shown that a relative change in P_i is related to a relative change in λ_i by:

$$\frac{\Delta P_i}{P_i} = \frac{\Delta \lambda_i}{\lambda_i}, \tag{5.4}$$

from which the change in the partial decay constant $\Delta\lambda_i$ is obtained. From Table 5.4, applied to ^{138}La equation 5.4 delivers $\Delta\lambda_{\beta^-} = 6\ (4) \times 10^{-24}\ s^{-1}$ and $\Delta\lambda_{EC} = 4.5\ (0.7) \times 10^{-23}\ s^{-1}$.

The rate at which a specific reaction occurs (R) is defined as the product of the number of target particles (T), the flux of incident particles (φ) and the cross-section for the reaction (σ):

$$R = T\phi\sigma. \tag{5.5}$$

Applied to β^--decay and electron capture of ^{138}La, respectively, the reaction rate is equal to the number of target nuclei affected per second by $\bar{\nu}_e$:

$$R_i = T\Delta\lambda_i. \tag{5.6}$$

From equations 5.5 and 5.6 upper limits for the cross-sections for $\bar{\nu}_e$ interacting with nuclei of ^{138}La are obtained:

$$\sigma_i = \frac{|\Delta\lambda_i|}{\Delta\phi_{\bar{\nu}_e}}, \tag{5.7}$$

where $\Delta\phi_{\bar{\nu}_e} \sim 8 \times 10^{12} cm^{-2}s^{-1}$ is the difference in $\bar{\nu}_e$ flux between reactor-off and -on. Equation 5.7 shows that the cross-section is independent of the source strength though it is dependent on the sensitivity to which the change in the decay constant can be determined, where the change in antineutrino flux is constant within a time period. Therefore the cross section serves only as an upper limit for antineutrino interaction, bound by the statistics achievable during a measurement, which may be improved on. Applied to ^{138}La, for β^--decay equation 5.7 yields as upper limits $\sigma_{\beta^-} = 8\ (4) \times 10^{-37} cm^2$ and for electron capture $\sigma_{EC} = 5.6\ (0.3) \times 10^{-36} cm^2$. Of course these results are based on the assumption that there is no effect on the decay rate of ^{40}K. Because ^{40}K and ^{138}La have similar half-lives a similar

result could also be obtained if the assumption is made that the spectral contribution due to the decay of ^{138}La remains constant and changes in the decay constant of ^{40}K were investigated using the E_γ = 1470 keV peak. Therefore it is difficult to attribute the above results; using the E_γ = 1470 keV peak, to changes in the decay rate of ^{138}La or ^{40}K individually, if antineutrinos were the cause.

5.6.2 The effect of $\bar{\nu}_e$ on the decay rate of ^{22}Na

For ^{22}Na two cases are possible:

Case #1: Assuming both λ_1 and λ_2 change relative to the other while λ (= λ_1 + λ_2) remains constant when the reactor goes from off to on.

During reactor-off symbols are used without a prime:

$P_1, P_2, \lambda_1, \lambda_2, \lambda$.

During reactor-on symbols are used with a prime:

$P_1', P_2', \lambda_1', \lambda_2', \lambda'$,

where the subscripts 1 and 2 refer to the two decay modes of ^{22}Na; β^+ and EC.

Case #1 leads to equation 5.4:

$$\frac{\Delta P_1}{P_1} = \frac{\Delta \lambda_1}{\lambda_1}, \tag{5.8}$$

$$\frac{\Delta P_2}{P_2} = \frac{\Delta \lambda_2}{\lambda_2}, \tag{5.9}$$

from which the change in the partial decay constants from reactor-off to -on can be solved.

Case #2: Assuming λ_1 changes while λ_2 remains constant or λ_2 changes while λ_1 remains constant, in either case λ changes as well when the reactor goes from off to on.

2.1: λ_1 changes while λ_2 remains constant.

$$\frac{\Delta P_1}{P_1} = \frac{P_1' - P_1}{P_1}$$

$$= \left(\frac{\lambda_1+\Delta\lambda_1}{\lambda_1+\lambda_2+\Delta\lambda_1} - \frac{\lambda_1}{\lambda_1+\lambda_2}\right)\left(\frac{\lambda_1+\lambda_2}{\lambda_1}\right)$$

$$= \frac{\lambda_2\Delta\lambda_1}{\lambda_1(\lambda+\Delta\lambda_1)}$$

$$= \frac{\lambda_2}{\lambda_1} A, \tag{5.10}$$

where $A = \frac{\Delta\lambda_1}{\lambda+\Delta\lambda_1}$.

Similarly,

$$\frac{\Delta P_2}{P_2} = \frac{P_2' - P_2}{P_2}$$

$$= -A, \tag{5.11}$$

2.2: λ_2 changes while λ_1 remains constant.

$$\frac{\Delta P_1}{P_1} = \frac{P_1'-P_1}{P_1}$$

$$= \left(\frac{\lambda_1}{\lambda_1+\lambda_2+\Delta\lambda_2} - \frac{\lambda_1}{\lambda_1+\lambda_2}\right)\left(\frac{\lambda_1+\lambda_2}{\lambda_1}\right)$$

$$= \frac{-\Delta\lambda_2}{\lambda+\Delta\lambda_2}$$

$$= -B, \tag{5.12}$$

Similarly,

$$\frac{\Delta P_2}{P_2} = \frac{\lambda_1}{\lambda_2} B, \tag{5.13}$$

where $B = \frac{\Delta\lambda_2}{\lambda+\Delta\lambda_2}$.

From equation 5.10 to 5.13 the change in the partial decay constants from reactor-off to –on can be solved as:

$$\Delta\lambda_1 = \frac{-A\lambda}{A - 1} \qquad 5.14$$

and

$$\Delta\lambda_2 = \frac{-B\lambda}{B - 1} \qquad 5.15$$

Table 5.6 provides the net-peak count rates of the E_γ = 511, 1275 and 1786 keV peaks in the BG subtracted Na+BG spectra after a linear continuum subtraction during the various measurement periods, also indicated is the power level of unit#2 during each period.

Table 5.6: *Average net-peak count rates per hour in the E_γ = 511, 1275 and 1786 keV peaks in the ^{22}Na standard spectra during the various measuring periods in 2011.*

Location	Date	511 keV (cph)	1275 keV (cph)	1786 keV (cph)	Power level of unit#2 (% of maximum)
Koeberg	26/04 – 18/05	2174580 (110)	494750 (60)	148310 (30)	0
Koeberg	18/05 – 21/05	2151600 (200)	489630 (110)	146690 (60)	25
Koeberg	25/05 – 26/05	2142200 (600)	487300 (300)	146420 (180)	90
Koeberg	02/06 – 03/06	2130700 (400)	484850 (180)	145400 (100)	90
Koeberg	14/06 – 30/06	2096660 (110)	477330 (50)	142690 (30)	100
iTL	08/08 – 18/08	2032830 (160)	461810 (80)	139530 (40)	N/A

In Table 5.6 one notices a decrease in the count rate reflecting the decay of the ^{22}Na source. The ratios R_1 and R_2 during the various measurement periods were obtained by applying equations 4.23 and 4.24 to the net-peak count rates in 5.6 and are listed in Table 5.7 using the corresponding estimated $\phi_{\bar{\nu}_e}$.

Table 5.7: *Ratios R_1 and R_2 during the various measuring periods and corresponding $\phi_{\bar{\nu}_e}$ in 2011.*

Location	Period	$\phi_{\bar{\nu}_e}(10^{12}\text{cm}^{-2}\text{s}^{-1})$	R_1	R_2
iTL	08/08 – 18/08	10^{-6}	14.569 (0.005)	3.3097 (0.0012)
Koeberg	26/04 – 18/05	0.87	14.662 (0.003)	3.3358 (0.0008)
Koeberg	18/05 – 21/05	3	14.668 (0.007)	3.3379 (0.0016)
Koeberg	14/06 – 30/06	8	14.694 (0.003)	3.3452 (0.0008)

Table 5.7 indicates a change in R_1 between iTL and Koeberg during 26 Apr – 18 May 2011 at almost similar $\phi_{\bar{\nu}_e}$, indicating that a change in the source-detector geometry might have occurred during the move from Koeberg to iTL. During the transition of reactor unit #2 from off to on, and changing of amplifiers, the ^{22}Na source was not removed from the lead shielding, therefore the increase of R_1 of Koeberg 18 – 21 May 2011 to Koeberg 14 – 30 June 2011 could be real or a systematic effect of changing the amplifiers. Directly after the iTL measurements the $LaBr_3$(Ce) detector was sent back to the owners and testing the systematic influence of changing the amplifiers could not be performed in a more controlled manner.

The ratios R_1 of Koeberg 26 Apr – 18 May 2011, Koeberg 18 – 21 May 2011 and Koeberg 14 – 30 June 2011 are used to correct for the possible change in source-detector geometry from Koeberg to iTL. Assuming a linear relation between the ratios R_1 and $\phi_{\bar{\nu}_e}$ a best fit is made to the ratios R_1 of Koeberg 26 Apr – 18 May 2011, Koeberg 18 – 21 May 2011 and Koeberg 14 – 30 June 2011with the function $R_1^{'}$:

$$R_1^{'} = 4.61\times10^{-15}\phi_{\bar{\nu}_e} + 14.66, \tag{5.16}$$

illustrated in figure 5.16.

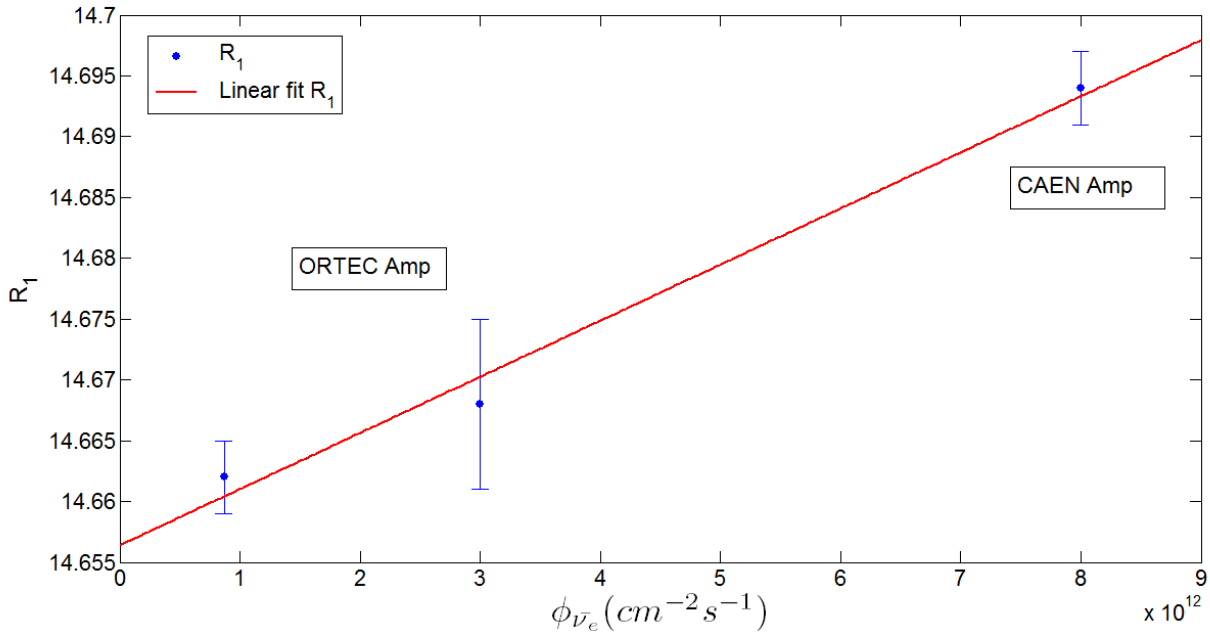

Figure 5.16: *Best fit linear function to the ratios R_1 of Koeberg 26/04 – 18/05, Koeberg 18/05 – 21/05 and Koeberg 14/06 – 30/06 in 2011.*

Applying equation 5.16 to the antineutrino flux at iTL, the corrected value for R_1 is obtained as $R_1^{'}$ = 14.66 with a correction factor (cf) of cf = 1.0062 (0.0003).This correction factor is also used to correct the ratio R_2 at iTL which delivers $R_2^{'}$ = 3.3304 (0.0017).

Assuming that the ratio R_2 has a linear behaviour as a function of $\phi_{\bar{\nu}_e}$, the corrected ratio for iTL, $R_2^{'}$, and the ratios, R_2, during the other periods can be fitted with a best fit linear function described by:

$$R_2^{fit} = 1.6 \times 10^{-15}\phi_{\bar{\nu}_e} + 3.332. \qquad (5.17)$$

By setting $\phi_{\bar{\nu}_e} = 0$ in equation 5.17 the ratio R_2 can be determined at zero antineutrino flux, $R_2(\phi_{\bar{\nu}_e}=0) = 3.332$. This value is substituted into equation 4.25 to determine the constant a = 4.62. From equation 4.27 the relative change in the branching ratio β_1 can be determined relative to $\phi_{\bar{\nu}_e} = 0$. Table 5.8 provides the relative change in the branching ratio $\frac{\Delta P_{\beta_1}}{P_{\beta_1}}$ as a function of $\phi_{\bar{\nu}_e}$ during the various measurement periods.

Table 5.8: *Relative change in the branching ratio β_1 as a function of antineutrino flux in 2011.*

Location	Period	$\phi_{\bar{\nu}_e}(10^{12}\text{cm}^{-2}\text{s}^{-1})$	$\frac{\Delta P_{\beta_1}}{P_{\beta_1}}$
iTL	08/08 – 18/08	10^{-6}	+0.0003 (0.0003)
Koeberg	26/04 – 18/05	0.87	-0.00075 (0.00016)
Koeberg	18/05 – 21/05	3	-0.0012 (0.0003)
Koeberg	14/06 – 30/06	8	-0.00259 (0.00016)

Table 5.8 indicates a relative decrease in the branching ratio β_1 with an increase of antineutrino flux. At an estimated antineutrino flux increase of $\phi_{\bar{\nu}_e} = 8 \times 10^{12}$ cm^{-2}s^{-1} the relative change in the β_1-decay branch of ^{22}Na is $\frac{\Delta P_{\beta_1}}{P_{\beta_1}}$ = -0.00259 (0.00016), an order of magnitude larger compared to reactor-off. Figure 5.17 graphically illustrates the relative change in β_1 as a function of $\phi_{\bar{\nu}_e}$.

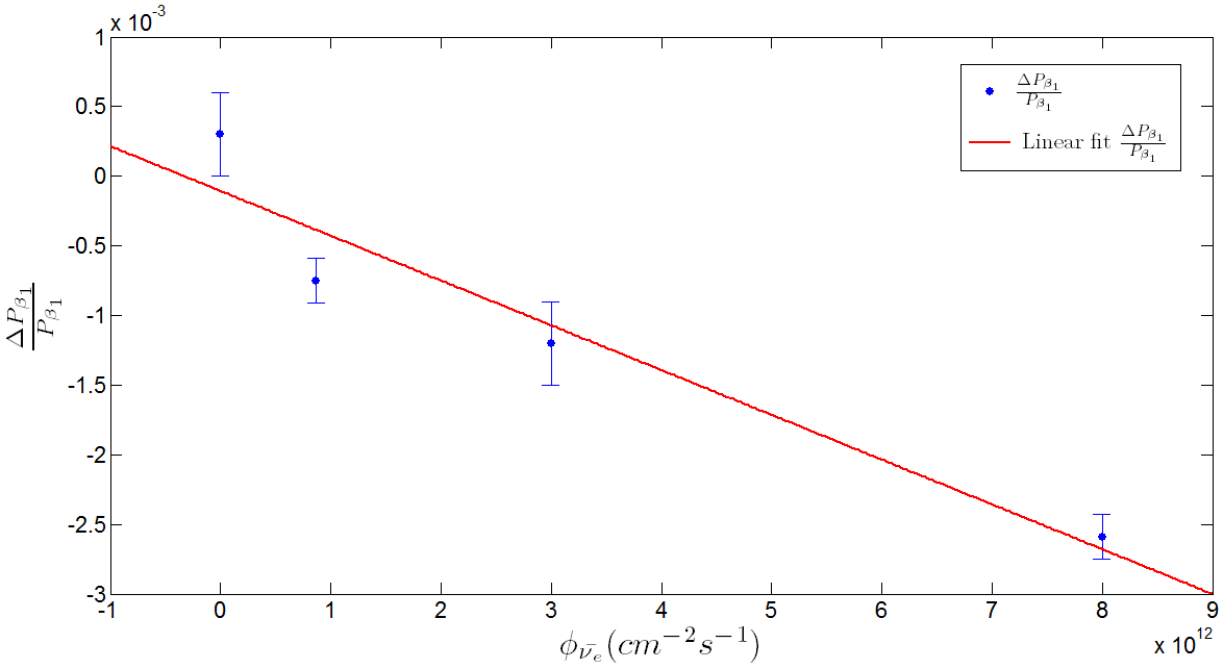

Figure 5.17: Graphical representation of $\frac{\Delta P_{\beta_1}}{P_{\beta_1}}$ as a function of $\phi_{\bar{\nu}_e}$.

If the effect is linear, a best fit to describe the relative change of β_1 as a function of antineutrino flux is:

$$\frac{\Delta P_{\beta_1}}{P_{\beta_1}} = -3.2 \times 10^{-16} \phi_{\bar{\nu}_e}. \quad (5.18)$$

Using equations 5.8 to 5.15 the change in the partial decay constants from reactor-off to –on for both cases can be determined after which equation 5.7 is applied to determine the corresponding interaction cross section for antineutrinos on the β^+ and electron capture decay branches of ^{22}Na, if antineutrinos were the cause. These results are presented in table 5.9.

Table 5.9: Change in the partial decay constants for case #1 and #2 as well as the corresponding interaction cross section for antineutrinos on the β^+ and electron capture decay branches of ^{22}Na, if antineutrinos were the cause. Also presented is the relative change in the total decay constant.

Case #	$\Delta\lambda_1$ (s^{-1})	$\sigma_{\lambda 1}$ (barn)	$\Delta\lambda_2$ (s^{-1})	$\sigma_{\lambda 2}$ (barn)	$\Delta\lambda/\lambda$ (%)
1	-1.97 (0.12)×10^{-11}	2 (5)	1.97 (0.12)×10^{-11}	2 (5)	±0.3
2.1	-20.04 (0.13)×10^{-11}	25 (2)	0	N/A	-2.6
2.2	0	N/A	2.2 (0.14)×10^{-11}	2.74 (0.09)	+2.7

For case #1 the relative change in the total decay constant is zero according to the assumption made for case #1. Thus if one decay branch decreases the other branch increases by the same magnitude. The partial decay constant for β^+ decay decreases by 1.97 (0.12) ×10^{-11} s^{-1} which corresponds to a 0.3% relative decrease in λ_1. Therefore the partial decay constant for electron capture decay has to increase with the same magnitude and the interaction cross section for both decay branches is the same at 2 barn.

For case #2.1 a decrease of 20.04 (0.13) ×10^{-11} s^{-1} in the partial decay constant for β^+ decay corresponds to a 2.6% relative decrease in λ_1 and an interaction cross section of 25 barn. For case #2.2 an increase of 2.2 (0.14) ×10^{-11} s^{-1} in the partial decay constant for electron capture decay corresponds to a 2.7% relative increase in λ_2 and an interaction cross section of 2.2 barn. For a 6 kBq ^{22}Na source ~7×10^{11} target nuclei are available where the aforementioned changes in the partial decay constants translates into ~10 to 10^2 nuclei per second being affected (speeding up decay) or not being affected (slowing down decay) if antineutrinos were the cause, compared to the expected rate of ~10^{-20} nuclei per second.

The results of cross sections are of the order of barns and 20 orders of magnitude larger than the cross section measured by Reines and Cowan for inverse β^+-decay through antineutrinos,

though the cross sections measured at Koeberg might be due to a different antineutrino interaction mechanism, if antineutrinos are indeed the cause.

5.7 Summary

This surprisingly large cross section, usually associated with nuclear reactions, prompted a confirmation measurement to eliminate the possibility of a false result that could have been caused by systematic factors such as the changing of the amplifier. Preparations for the second series of measurements at Koeberg began prior to the next scheduled outage, planned for 12/03/2012 on unit#1. Chapter 6 describes the second series of measurements at Koeberg using a NaI detector as unit#1 made the transition from on to off and back on again.

CHAPTER 6 Measurement series 2: NaI(Tl) and HPGe detector

6.1 NaI(Tl) detector properties

Due to the unavailability of the $LaBr_3(Ce)$ detector for the second series of measurements a NaI(Tl) detector (manufactured by BICRON, model number: 3XMS/3H-LED-X) with a crystal length of l = 127 mm and diameter of $\emptyset$ = 101.6 mm was used. This was the only option available at the time for a follow-up measurement, which was dictated by the reactor outage schedule. The NaI(Tl) detector provides a larger solid angle and has a considerably lower intrinsic background compared to the $LaBr_3(Ce)$ detector. NaI(Tl) crystals have a density of ρ = 3.7 g/cm^3 and $\Delta E/E$ ~ 7% energy resolution at E_γ = 662 keV with a time resolution of the order of nano seconds and a light decay time constant of τ = 230 ns [107] which is an order of magnitude slower than a $LaBr_3(Ce)$ detector. Since Compton scattering is the main interaction mechanism for γ-rays with energies up from several hundred keV to a few MeV, the NaI(Tl) detector has a poorer efficiency than the $LaBr_3$ detector due to its lower crystal density, for these energies.

The NaI(Tl) detector used during this measurement has been used previously as a charged particle detector in cyclotron experiments and showed some signs of deterioration. At the time it was the best NaI detector available at iTL. Radiation damage creates colour-centres which are impurities or defects in the crystal that cause electron traps or metastable states with long lifetimes [108, 109, 110]. Colour-centres have absorption bands that reduce the crystal's light attenuation length and thus light output. Another consequence is increased afterglow causing an increase in readout noise. The overall effect on the detector is deteriorating efficiency, energy resolution and time resolution. The full effects on the measurement only became clear during the data analysis.

6.2 HPGe detector properties

It was also decided to separately measure γ-rays from another ^{22}Na source with a HPGe detector due to its higher energy resolution and better peak-to-compton ratio, in parallel to the NaI(Tl) detector measurement. The HPGe detector was manufactured by ORTEC, model number: GMX-10200 with a crystal length of l = 127 mm and diameter of $\emptyset$ = 101.6 mm. The detector has a $\Delta E/E$~0.2% energy resolution at E_γ = 662 keV and was cooled with liquid nitrogen. The detector has a time resolution comparable to that of NaI(Tl). A disadvantage of

this detector is that the Ge crystal is thin and planar, consequently its γ-ray detection efficiency is several times smaller than NaI(Tl) [80]. Also, the detector has to be operated at low temperatures to reduce thermally generated leakage current [80]. Figure 6.1 compares Na+BG spectra measured with the NaI(Tl) and HPGe detector, respectively.

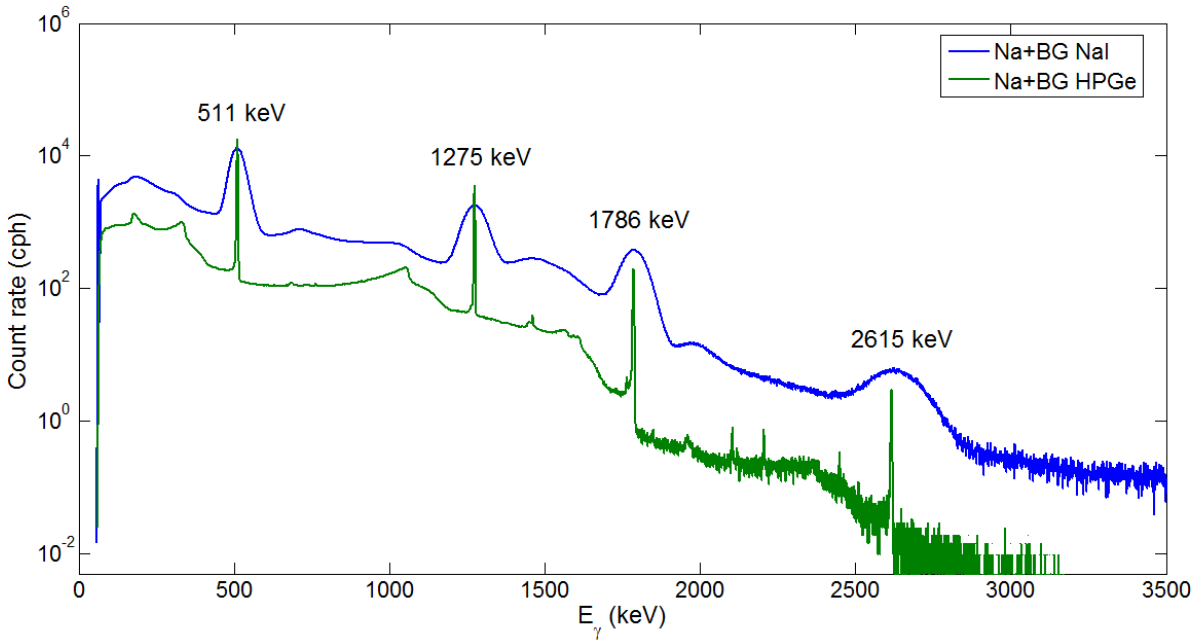

Figure 6.1: *Comparison of Na+BG spectra measured with the NaI(Tl) (blue) and HPGe detector (green) on a log scale.*

Indicated are the E_γ = 511, 1275 and 1786 keV peaks resulting from the decay of ^{22}Na, also shown is the E_γ = 2615 keV peak resulting from the decay of ^{208}Tl, present in the room background. Noticeable is the several orders of magnitude lower count rate of the E_γ = 1786 keV peak measured with the HPGe detector compared to that of the NaI(Tl) detector, indicating that this specific HPGe detector does not suffice in terms of the precision required from the peak ratios.

From Figure 6.1 it is clear that the NaI(Tl) and HPGe detectors exhibit the same major features of the γ-ray spectra. In Figure 6.2 BG spectra measured with the NaI(Tl) and HPGe detectors are compared.

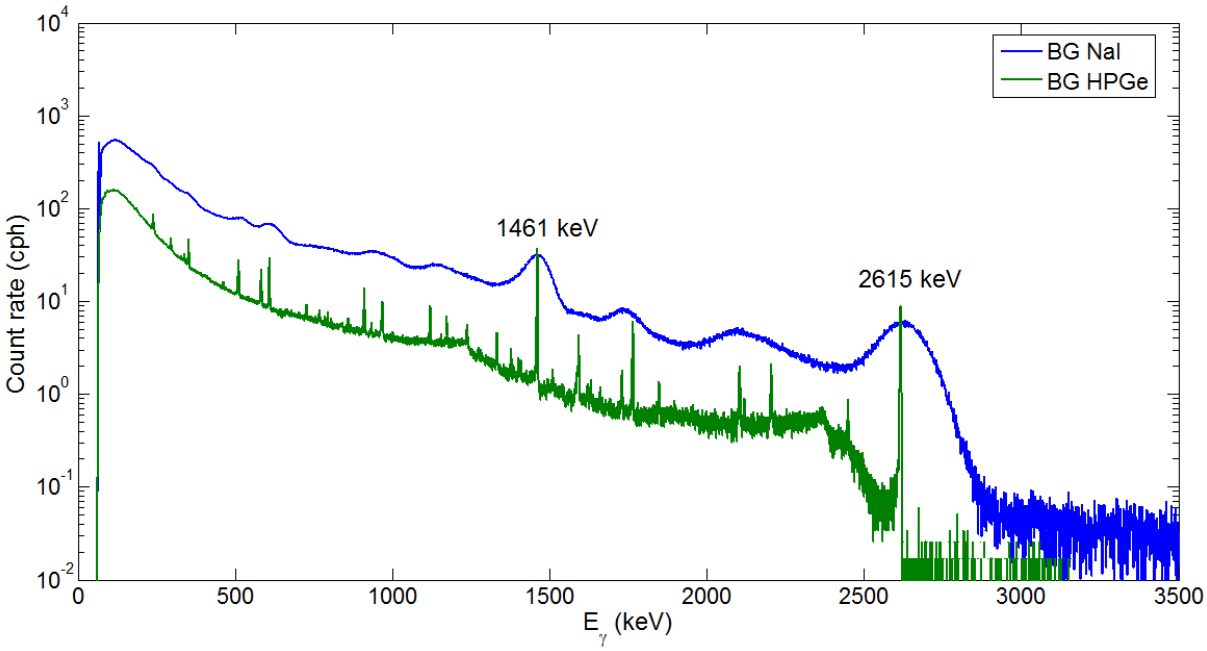

Figure 6.2: *Comparison of BG spectra measured with the NaI(Tl) (blue) and HPGe detector (green) on a log scale.*

Indicated are the most prominent E_γ = 1461 keV and 2615 keV peaks in the BG. Clearly noticeable are many peaks resolved by the HPGe detector compared to the NaI(Tl) detector as well as the higher peak-to-Compton ratio, but again the major features of the background show up in both detectors.

6.3 Experimental set-up

6.3.1 NaI(Tl) detector set-up

For the second series of measurement the NaI(Tl) detector was installed at the Koeberg Nuclear Power Station unit#1 in the seismic vault approximately l = 17 m and 88 m from the centre of the cores of unit#1 and unit#2, respectively. From the top, the detector was shielded from the reactor core by approximately d = 7.5 m of concrete, indicated in Figure 2.7. The vault is naturally ventilated by a small gap of width approximately w = 0.5 m all along the sides of the vault. Together with the large surface and volume of the concrete structures, this location is a more stable and benign environment for an experimental set-up. Moreover this location is outside the radiation protection zone. To further stabilise the conditions around the detector set-up, and to prevent dust deposition on the equipment, the measurement area was enclosed with plastic sheets. The local air temperature and humidity was measured continuously for approximately two months and remained more or less constant at T ~ 21°C

and RH ~ 60%, respectively. The humidity was lowered by silica beads placed inside the measuring area.

The cylindrical lead shielding and ^{22}Na sources which were used for the first measurement series were also used for the second measurement series with the NaI(Tl) detector. To accommodate the larger housing of the NaI(Tl) detector the opening in the lead for the detector was machined somewhat wider. The detector was powered by an ORTEC 556 high-voltage power supply at V_{bias} = +1260 V. The positive signal from the detector was fed to an ORTEC 113 pre-amplifier and subsequently amplified by a Canberra 2020 spectroscopy amplifier with a shaping time of τ_s = 1 μs. The amplifier was powered by a NIM-bin. The data-acquisition system consisted of an ATOMKI palmtop MCA (8k-01) and a laptop which recorded γ-ray spectra every twenty minutes without pile-up rejection. The BLR was set to "auto".

6.3.2 HPGe detector set-up

The HPGe detector was installed approximately l = 1.3 m from the NaI(Tl) detector. The detector was placed inside a lead cylinder with similar dimensions as the shielding for the NaI(Tl) detector and accommodating a source holder containing a 2 kBq ^{22}Na source. A SILENA 7716/LN high-voltage power supply was used to power the detector at V_{bias} = 1500 V. The unipolar signal from the built-in pre-amplifier was fed through a Canberra 2020 spectroscopy amplifier, powered by a NIM-bin, into the MCA with a shaping time of τ_s =1 μs. The data-acquisition system consisted of a seperate ATOMKI palmtop MCA (8k-01) and a desktop PC which recorded γ-ray spectra every twenty minutes without pile-up rejection. The BLR was set to "auto". Figure 6.3 shows a photograph of the HPGe detector set-up at the measuring site at Koeberg.

Figure 6.3: *Photograph of the HPGe detector set-up at Koeberg.*

6.4 Measurement description

6.4.1 NaI(Tl) detector

The measurement started on 16/02/2012 while both reactor units were operating at full-power. Background was measured first until 21/02/2012 and then followed by Na+BG measurements. The Na+BG measurements continued until 27/06/2012 after which a final BG measurement was made until 01/08/2012. During this period unit#1 was shut down on 12/03/2012 for refuelling and maintenance and was started up again on 22/05/2012, while unit#2 was operating at full-power. Table 6.1 provides a summary of the number of one-hour spectra recorded during the second measurement series with the NaI(Tl) detector which lasted approximately five and a half months.

Table 6.1: *Summary of the quantity of data recorded with the NaI(Tl) detector during various phases of reactor operation of unit#1 in 2012.*

Date	Number of one-hour spectra	Type of spectrum	Power level of unit#1 (% of maximum)
16/02 – 21/02	116	BG	100
21/02 – 12/03	468	Na+BG	100
12/03 – 22/05	1594	Na+BG	0
22/05 – 27/06	960	Na+BG	100
27/06 – 01/08	808	BG	100

Fortunately no equipment malfunction was experienced during the second series of measurements with the NaI(Tl) detector. A total of 924 one-hour BG spectra and 1428 Na+BG spectra were obtained while unit#1 was on. While unit#1 was in outage, 1594 Na+BG spectra were obtained. It was decided best not to remove the source during outage, but to measure Na+BG as unit#1 started up again, which would provide a second opportunity to investigate any possible change in the decay rate of ^{22}Na. Therefore, a BG measurement was not made while unit#1 was in outage.

6.4.2 HPGe detector

This measurement was also started on 16/02/2012 with BG until 21/02/2012 when the Na+BG measurement started. Unfortunately, a few days before reactor unit#1 was shut-down, during the refilling of the liquid nitrogen Dewar, the HPGe detector was inadvertently bumped causing a change in the source-detector geometry, rendering a quantitative comparison of Na+BG spectra between reactor-on and-off periods unfeasible. On 29/03/2012 while unit#1 was off, a BG measurement was started until 02/04/2012. Table 6.2 provides a summary of the number of one-hour BG spectra recorded with the HPGe detector.

Table 6.2: *Summary of the quantity of BG data recorded with the HPGe detector during reactor-on and -of phases of unit#1.*

Date	Number of one-hour spectra	Type of spectrum	Power level of unit#1 (% of maximum)
16/02 – 21/02	117	BG	100
29/03 – 02/04	99	BG	0

Most importantly, from the HPGe detector measurement, a comparison of the BG during reactor-on and -off phases can be made. A total of 117 and 99 one-hour BG spectra were obtained during reactor on- and -off periods, respectively.

6.5 Reliability of the data acquisition systems

6.5.1 NaI(Tl) detector

As with the $LaBr_3(Ce)$ detector, the spectra measured with the NaI(Tl) detector were first checked for peak drift. Illustrated in Figure 6.4 is the peak drift of the E_γ = 1461 keV peak in the BG spectra (selected since it is the most prominent peak in the BG) and the E_γ = 1275 keV peak in the Na+BG spectra. Also indicated by the dashed lines are the on and off periods of unit#1.

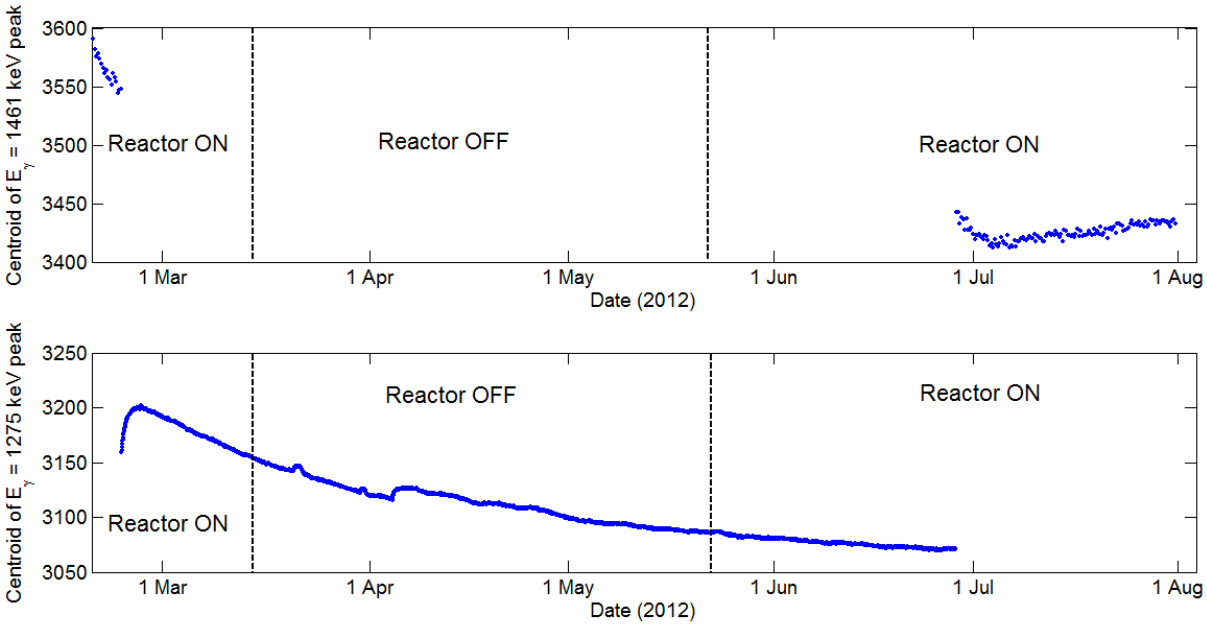

Figure 6.4: *Peak centroid drift of the E_γ = 1461 keV peak in the BG spectra and E_γ = 1275 keV peak in the Na+BG spectra. On and off periods of unit#1 are indicated by the dashed lines.*

During BG measurement of 16 to 21 February the E_γ = 1461 keV peak drifts toward the low-energy side, the same trend is seen at the beginning of the BG measurement of 29 March to 2 April, after which the peak drifts toward the high-energy side but slower than the initial drift toward the low-energy side. This initial drift toward the low-energy side, lasting for t = 110 hours, during both BG measurement periods can be seen as a possible stabilisation period of the detector and electronics, though this stabilisation period is almost five times longer than what is usually observed. After the BG measurement during period A, the source is inserted and the E_γ = 1275 keV peak initially drifts quickly toward the high-energy side where a cusp is formed on approximately 26 February. After the cusp, the peak drift seems to follow an exponential decay containing a few prominent kinks along the way on approximately 19 and 28 March and also 5 April, with less noticeable ones following afterward. It can be argued that with an almost constant air temperature, the most straight forward explanation for the exponential peak drift is due to the decay of the source and that the drift is dependent on the source count rate, though the exact cause of the drift and the kinks is unknown.

The decaying source also affects the live-time of the detection system. In Figure 6.5 the live-time while γ-rays from the source were being measured is shown in green. Also shown in blue is the peak drift of the E_γ = 1275 keV peak in the Na+BG spectra.

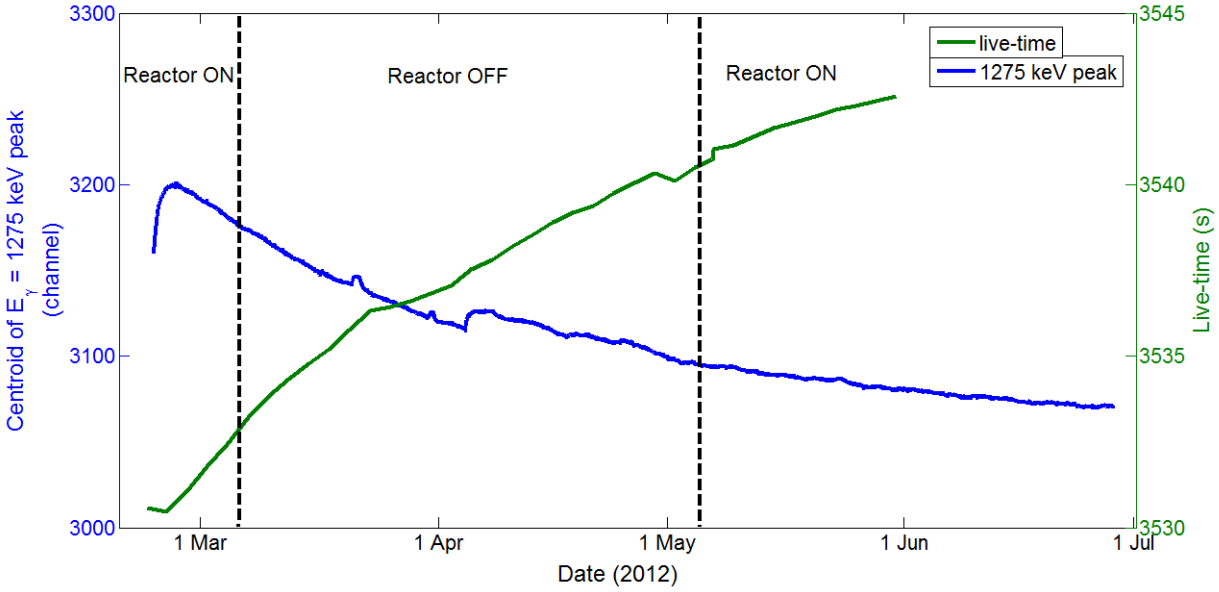

Figure 6.5: *Correlation between gain drift and live-time in the NaI(Tl) detector.*

As the source decays, the count rate in the detector decreases therefore it is expected that the live-time of the system increases, this is confirmed in Figure 6.5 which shows a 0.3% increase in the live-time while γ-rays from the source were measured. Another possible factor that could have an effect on the live-time is the gain-drift. Drift toward the low-energy side, past the energy threshold, causes a loss of counts leading to a decrease in the total count rate thus decreasing the dead-time and increasing the live-time of the detection system. This effect was also observed during measurement series 1. The correlation between the gain drift and the live-time of the detection system is shown in Figure 6.5. Figure 6.5 indicates that peak drift of approximately 4% corresponds to an increase of the live-time of approximately 0.3%. As the live-time increases during the ^{22}Na measurement, it is possible that the BG contribution to the spectrum increases, which could result in inaccurate creation of BG corrected average ^{22}Na spectra. This of course increases the systematic uncertainty in determining net-peak areas and can affect the interpretation of results. The effect of BG changes is investigated.

Due to the low statistics in the BG spectra, off-line spectrum stabilisation was applied to six-hour BG spectra to obtain a more accurate stabilisation. For Na+BG data, spectrum stabilisation was applied on an hourly basis. After spectrum stabilisation the one hour Na+BG spectra were summed over seventy two hours to obtain a precision comparable to that of measurement series 1. The seventy two-hour average spectra were then checked for pile-up in terms of peak width changes, expressed by the standard deviations of the peaks.

Figure 6.6 illustrates the peak widths of the E_γ = 511, 1275 and 1786 keV peaks in the seventy two-hour average Na+BG spectra as a function of time.

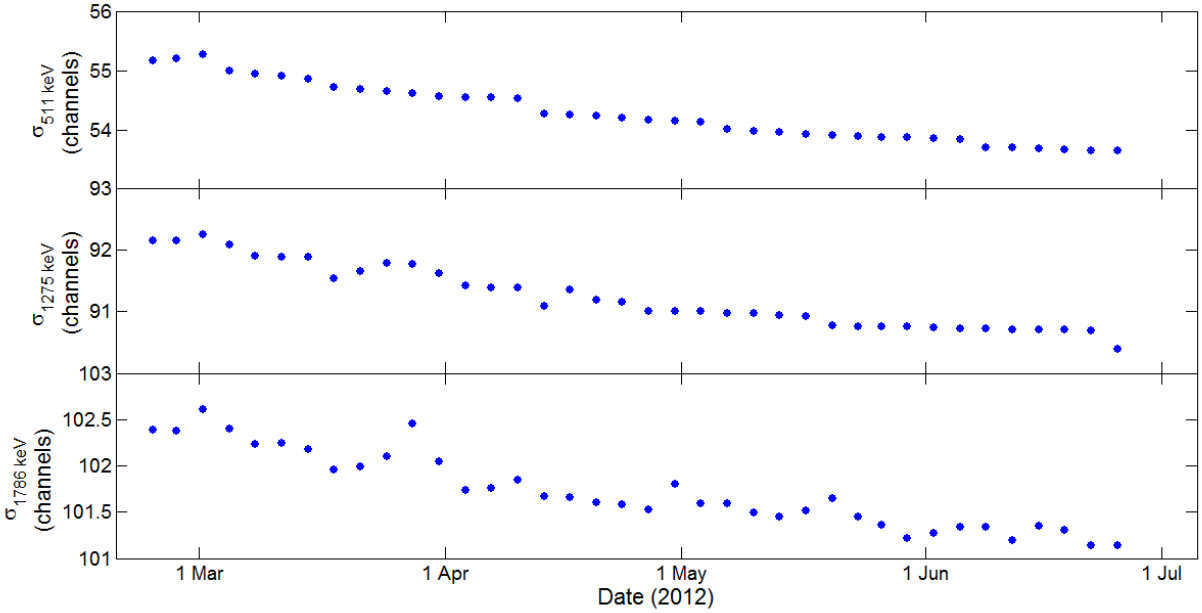

Figure 6.6: *Standard deviation of the E_γ = 511, 1275 and 1786 keV peaks in the seventy two-hour average Na+BG spectra as a function of time.*

All three peaks show an approximately 1 channel narrowing from the beginning to the end of the ^{22}Na measurement as the effect of pile-up decreases, as the total count rate decreases. Evidence of pile-up becomes clearest when comparing the E_γ = 2615 keV peak in the Na+BG spectra which is wider compared to that of the BG as shown in Figure 6.7. Also evident is the increase in the continuum of the E_γ = 2615 keV peak in the Na+BG spectra relative to that of the BG spectra; due to pile-up events from E_γ = 511 and 1275 keV photons with the E_γ = 2615 keV peak continuum.

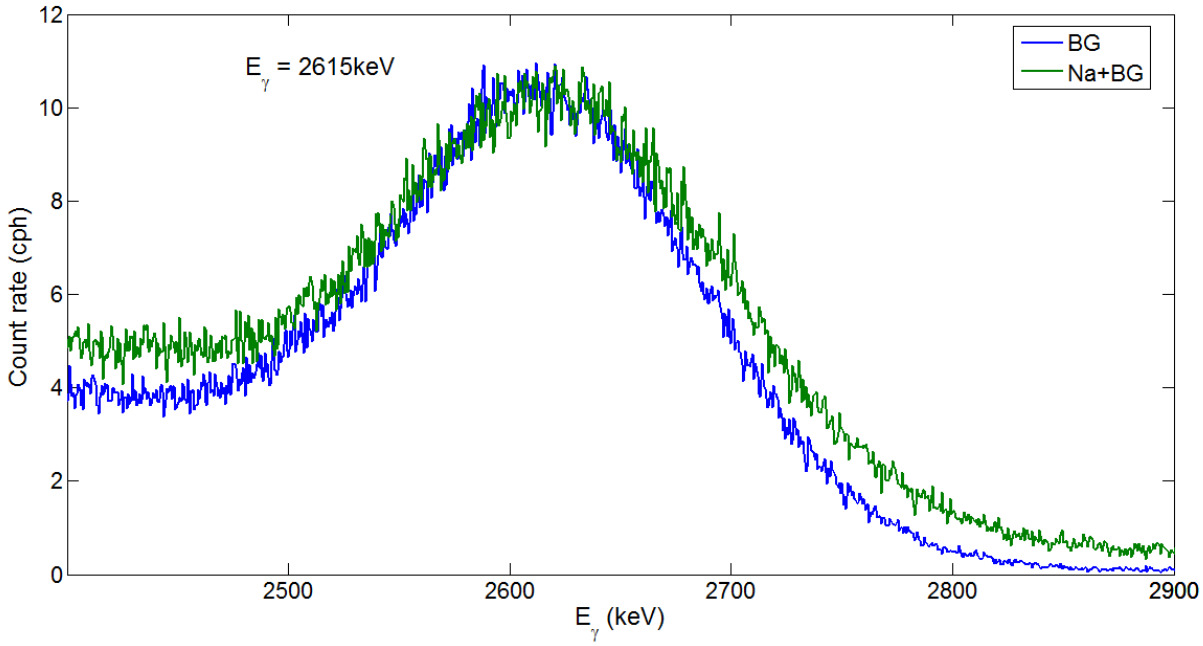

Figure 6.7: *Comparison of the E_γ = 2615 keV peak in the BG and Na+BG spectra where peak broadening is observed when measuring ^{22}Na.*

To simulate and investigate the effect of pile-up on net-peak count rates, a linear continuum is subtracted from the E_γ = 511, 1275 and 1786 keV peaks of a one-hour BG corrected Na+BG spectrum using the average BG from 16 – 21 February, after which the net-peak count rates are recomputed using linear continua that are extended by one channel to the low- and high-energy side, respectively. The results are provided in Table 6.3.

Table 6.3: *Net-peak count rates of the E_γ = 511, 1275 and 1786 keV peaks before and after extending the linear continua by two channels.*

	control	two channel increase
Energy (keV)	Count rate (cph)	Count rate (cph)
511	1522000 (3000)	1521000 (3000)
1275	312000 (2000)	312000 (2000)
1786	71400 (1000)	72000 (1000)

The results in Table 6.3 show that the net-peak count rates remain the same before and after a two channel change in peak width. Therefore the effect of pile-up is not significant.

Because the net-peak count rate calculation is dependent on subtraction of a constant BG, changes in the BG can lead to inaccurate results. To investigate BG changes the six-hour average BG count rates in the energy region 143 keV < E_γ < 1909 keV are plotted as a function of time in Figure 6.8. Also indicated by the solid horizontal lines are the weighted mean during each BG period.

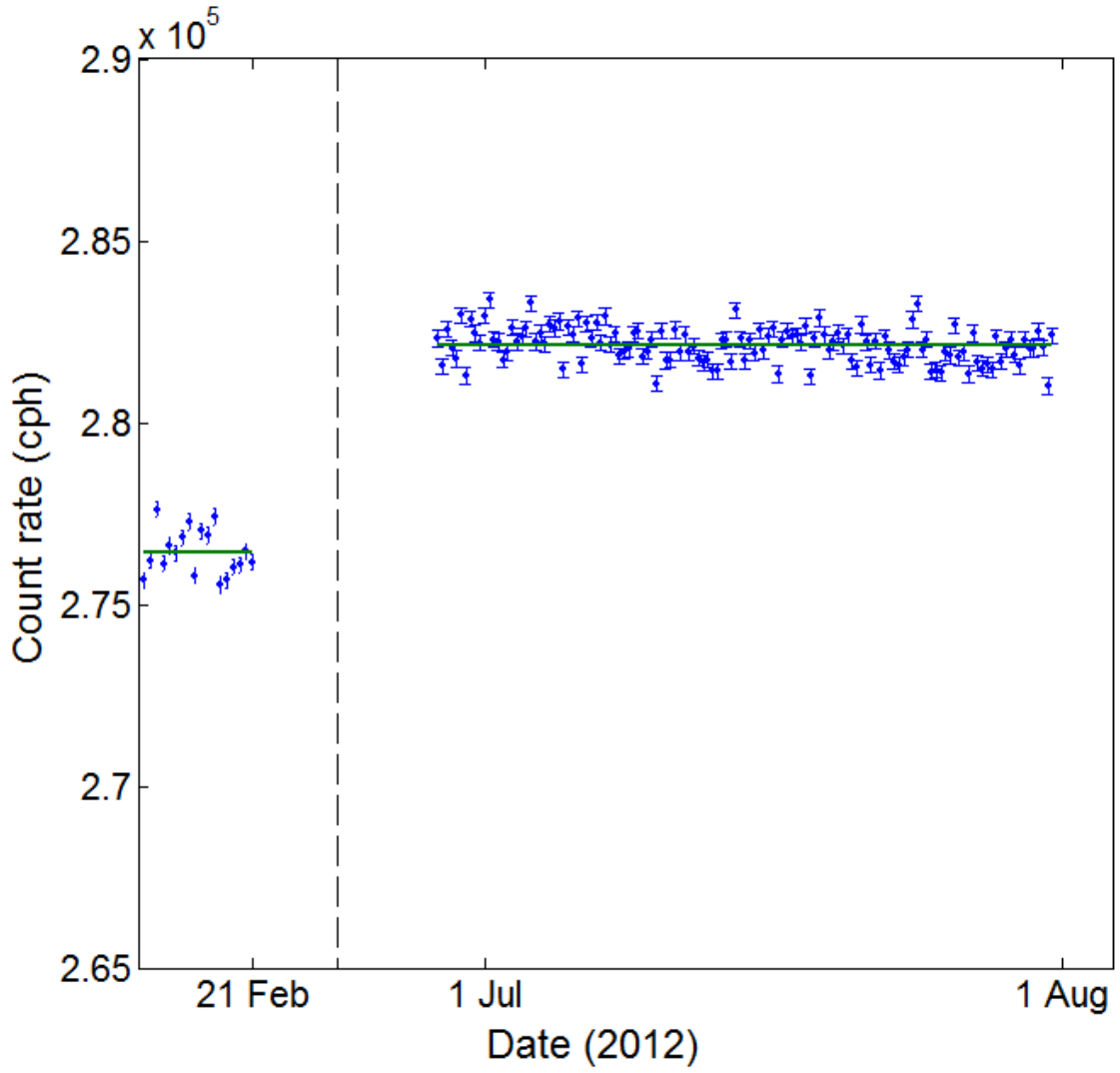

Figure 6.8: *Comparison of the six-hour average BG count rates in the energy region 143 keV < E_γ < 1909 keV while unit#1 was on. The weighted mean during each period is also indicated by the solid horizontal lines. For better comparison the months where BG was not measured were "cut out" of the figure.*

Table 6.4 provides the weighted mean of the hourly count rates during each period as well as the χ^2 relative to the weighted mean of the count rates.

Table 6.4: *Counting statistics of the six-hour average BG spectra in the energy region 143 < E_γ < 1909 keV during the various periods while unit#1 is on.*

Energy (keV)	16 – 21 Feb		27 June – 1 Aug	
	wm (cph)	χ^2	wm (cph)	χ^2
143 < E_γ < 1909	276430 (50)	8.5	282130 (20)	4.9

With χ^2-values of χ^2 = 8.5 and 4.9, respectively, it indicates that the BG count rate during the periods 16 to 21 February and 27 June to 1 August does not remain constant. The mean of the BG count rate increases by approximately 2% from February to August.

In an attempt to isolate the energy regions affected by changes in the BG count rate, the count rate in smaller energy regions is investigated. Table 6.5 provides the net-peak count rates of the E_γ = 511, 1173, 1333, 1461 and 2615 keV peaks during the two BG measurement periods. Also included are the count rates in the energy regions 143 keV < E_γ < 1568 keV and 1569 keV < E_γ < 1909 keV.

Table 6.5: *Net-peak count rates of the E_γ = 511, 1173, 1333, 1461 and 2615 keV peaks in the average BG spectra as well as the count rate in the energy regions 143 < E_γ < 1568 keV and 1569 < E_γ < 1909 keV.*

Energy (keV)	16/02 – 21/02	27/06 – 01/08
511	720 (30)	726 (11)
1461	4730 (40)	4822 (14)
2615	1176 (11)	1190 (4)
143 < E_γ < 1568	271100 (50)	276840 (20)
1569 < E_γ < 1909	5330 (7)	5401 (3)

Table 6.5 indicates that the net-peak count rate of the E_γ = 511 and 2615 keV peaks remain constant. The count rate in the energy region 143 keV < E_γ < 1568 keV as well as the E_γ = 1461 keV peak increases by approximately 2% from February to August. The count rate in the energy region 1569 keV < E_γ < 1909 keV increases by approximately 1.3%. Further investigation of the count rate in smaller energy regions below E_γ = 1568 keV showed that

the 2% increase in the BG count rate is not isolated to a specific energy region. The change in BG count rate during the two periods is most likely due to room BG variations caused by Radon level variations caused by changing ventilation over time. More specifically, the cause of the increase in the count rate of the E_γ = 1461 keV peak is unknown.

Investigation of the 24 h average BG count rate in the energy region 143 < E_γ < 1909 keV reveals that oscillations occur, illustrated in Figure 6.9.

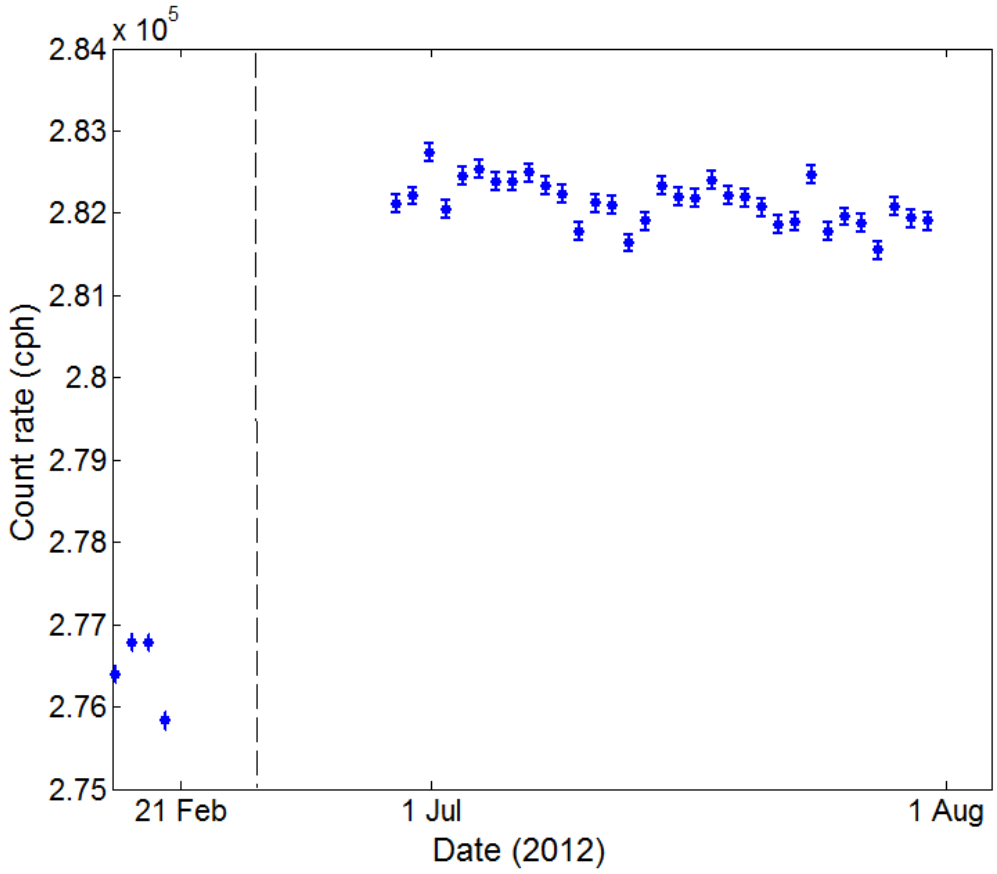

Figure 6.9: *24 h Average BG count rates during the two BG measurement periods in the energy region 143 < E_γ < 1909 keV while unit#1 was on. For better comparison the months where BG was not measured were "cut out" of the figure.*

Figure 6.9 indicates that oscillations with a period of approximately 15 days occur in the average BG count rate from July to August. Sufficient BG data is not available to observe if any oscillations are also present during February. Further investigation in smaller energy regions revealed that the oscillations only occur in the region 143 < E_γ < 1568 keV. The cause of the oscillations in the BG count rate is unknown at this time.

From Table 6.4 it was concluded that the BG count rate increases by approximately 2% from February to August. Table 6.6 provides the net-peak count rates of the E_γ = 511, 1275 and 1786 keV peaks determined from a one-hour BG corrected Na+BG spectrum using average BG from 16 to 21 February and from 27 June to 1 August, respectively, to illustrate the effect of the changing BG on net-peak count rates as well as the gross count rate in the energy region $1380 < E_\gamma < 1925$ keV.

Table 6.6: *Net-peak count rates of the E_γ = 511, 1275 and 1786 keV peaks as well as the gross count rate in the energy region $1380 < E_\gamma < 1925$ keV, determined from a one-hour BG corrected Na+BG spectrum using average BG from 16 to 21 February and from 27 June to 1 August, respectively.*

	ave BG 16- 21 Feb	ave BG 27 June - 1 Aug
Energy (keV)	Count rate (cph)	Count rate (cph)
511	1522000 (3000)	1522000 (3000)
1275	312000 (2000)	312000 (2000)
1786	71400 (1000)	71400 (1000)
$1380 < E_\gamma < 2156$	240500 (500)	240300 (500)

Table 6.6 shows that the net-peak count rates of the E_γ = 511, 1275 and 1786 keV peaks as well as the gross count rate in the energy region $1380 < E_\gamma < 1925$ keV are not affected by a changing BG count rate of approximately 2%. Typical count rates in a one-hour Na+BG and BG spectrum are approximately N(Na+BG) = 0.6×10^7 cph and N(BG) = 0.3×10^5 cph, respectively. Therefore the BG count rate represents approximately 5% of the count rate in the Na+BG spectrum. From the above results it can be concluded that the changing BG count rate does not significantly affect net-peak count rates and to a lesser extent the gross count rates, since the systematic effect of a linear continuum subtraction is eliminated. In conclusion, pile-up leading to a maximum peak width change of two channels and a changing BG of approximately 2% do not affect the net-peak count rates nor the gross count rates in the Na+BG spectra.

Figure 6.10 shows the regions of interest used to determine the ratio of count rates in the BG subtracted Na+BG spectra. Gate I: 1380 < E_γ < 2156 keV.

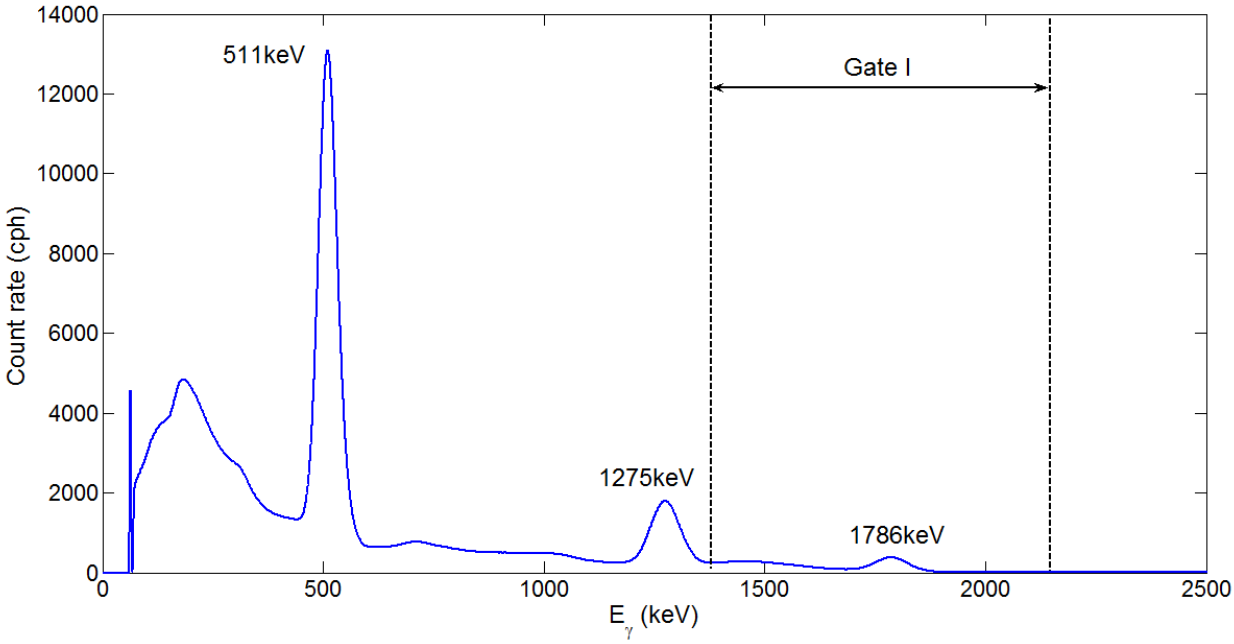

Figure 6.10: *Regions of interest used to determine the ratio of count rates in the BG corrected Na+BG spectra.The spike on the low energy side at approximately E_γ = 70 keV is an artifact of the MCA.*

The E_γ = 1275 keV peak contains contributions from β^+-decay as well as EC. The net E_γ = 511 keV peak and Gate I contain contributions resulting from β^+-decay only. If either of the β^+ or EC decay branches are affected, the ratio of the gross count rate of the E_γ = 1275 keV (1137 < E < 1379 keV) peak and Gate I should also be affected while the ratio of the net count rate of the E_γ = 511 keV peak and Gate I remains constant. The above gates are chosen to provide the best statistics for detecting changes in the ratios.

Figure 6.11 shows the ratios of net-peak count rate of the E_γ = 511 keV peak, the gross count rate of the E_γ = 1275 peak and Gate I as a function of time.

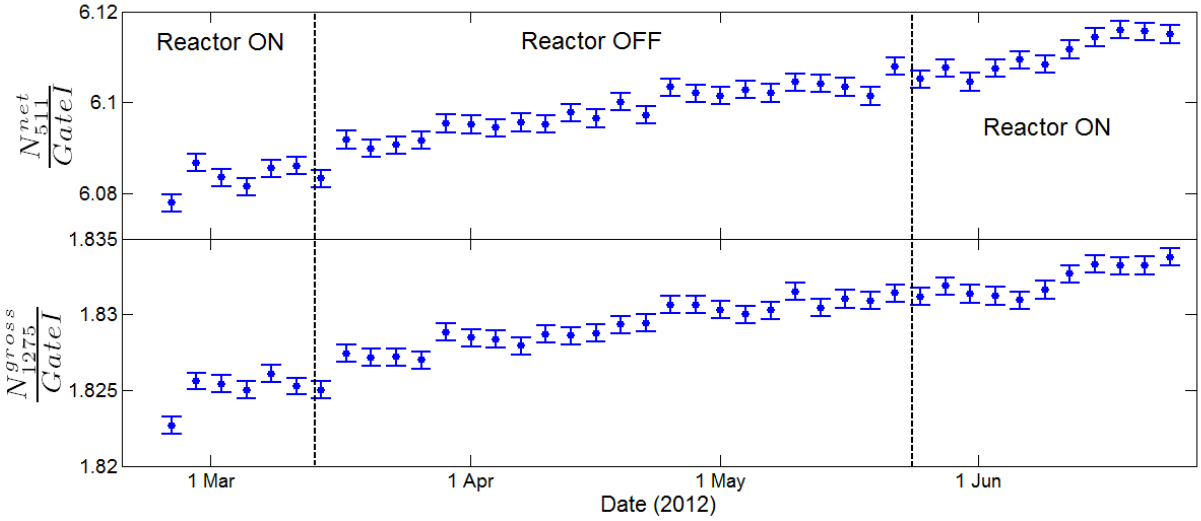

Figure 6.11: *72 h Average ratio of the net-peak count rate of the E_γ = 511 keV peak, gross count rate of the E_γ = 1275 keV peak and Gate I as function of time, while unit#1 makes the transition from on to off and back on again.*

From Figure 6.11 it is evident that none of the ratios remain constant and exhibit a general increase as a function of time, which appears not to be related to the reactor status. To investigate the count rate in the numerator and denominator in the ratios, the net-peak count rate of the E_γ = 511 keV peak and gross count rate of the E_γ = 1275 keV peak and Gate I are, after BG subtraction, corrected for decay and normalised, presented in Figure 6.12. Also indicated by the solid horizontal lines is the weighted mean.

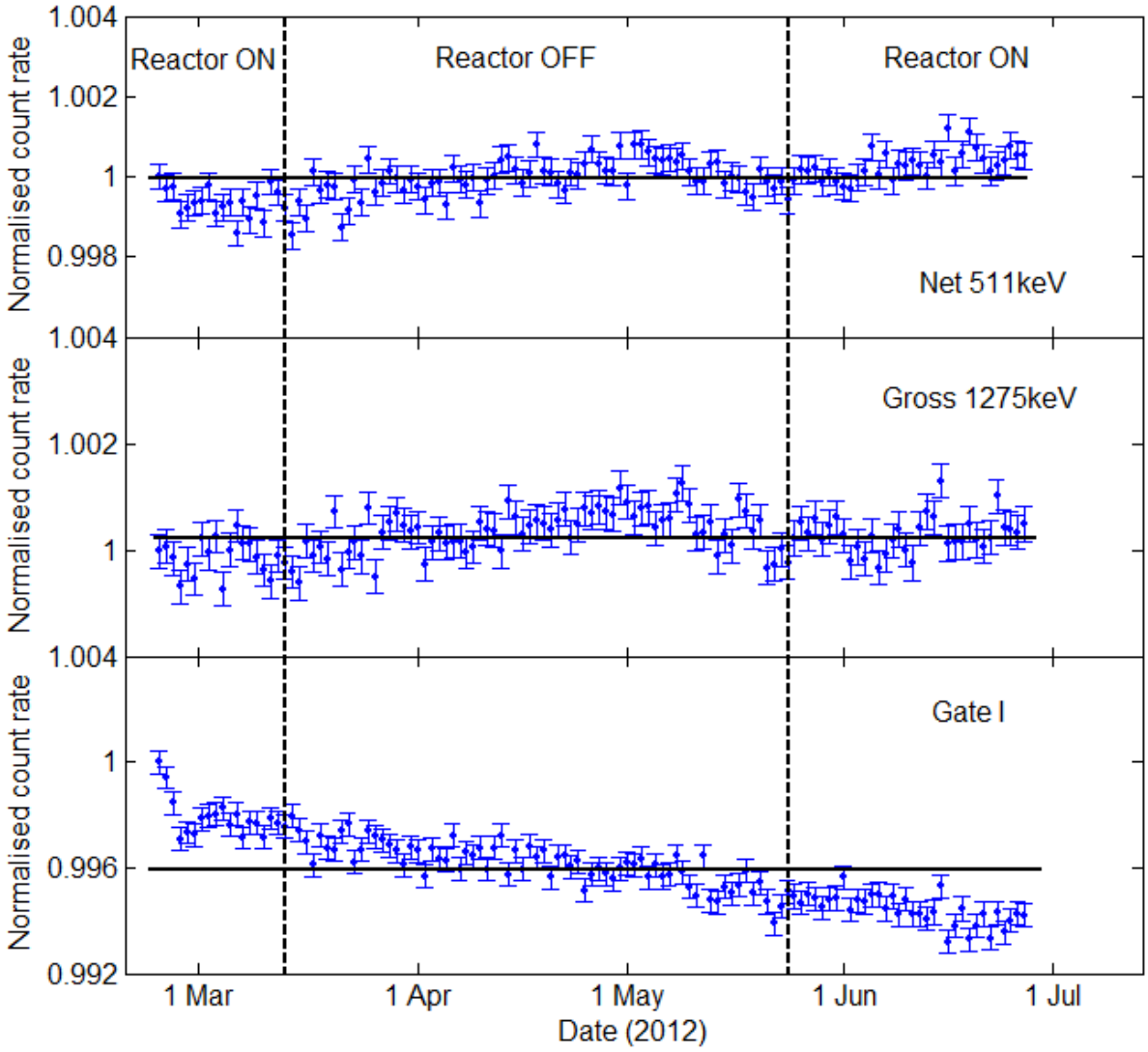

Figure 6.12: *24 h Average BG subtracted, decay corrected, and normalised count rate of the E_γ = 511 keV peak and gross count rate of the E_γ = 1275 keV peak and Gate I. The solid horizontal lines represent the weighted mean.*

The decreasing normalised count rate in Gate I explains why the ratio of of $\frac{N_{511}^{Net}}{Gate\ I}$ and $\frac{N_{1275}^{Gross}}{Gate\ I}$ increases. Table 6.7 provides the weighted mean of the 24 h average BG subtracted, decay corrected, and normalised count rate of the E_γ = 511 keV peak and gross count rate of the E_γ = 1275 keV peak and Gate I as well as the χ^2-values relative to the weighted mean.

Table 6.7: *Weighted mean of the 24 h average BG subtracted, decay corrected, and normalised count rate of the E_γ = 511 keV peak and gross count rate of the E_γ = 1275 keV peak and Gate I as well as the χ^2-value relative to the weighted mean.*

	wm	χ^2
Net 511	0.99995 (0.00003)	2.36
Gross 1275	1.00029 (0.00003)	1.73
Gate I	0.99596 (0.00004)	9.51

With χ^2-values of χ^2 = 2.36, 1.73 and 9.25 respectively, it indicates that the average BG subtracted, decay corrected, and normalised count rate of the E_γ = 511 keV peak and gross count rate of the E_γ = 1275 keV peak and Gate I does not remain constant as a function of time and appear not to be related to the reactor status.

To obtain better statistics the 24 h average gross count rate in the energy region 130 keV < E_γ < 1896 keV of the Na+BG spectra is BG subtracted, decay corrected and normalised, presented in Figure 6.13.

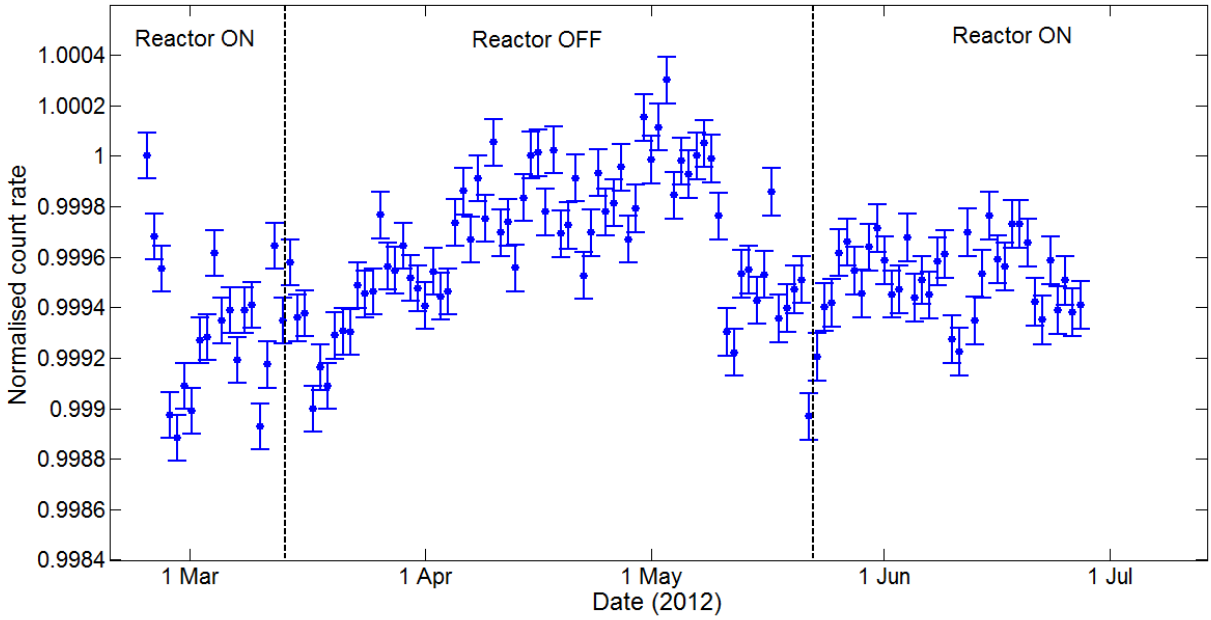

Figure 6.13: *24 h Average BG subtracted, decay corrected, and normalised count rate in the energy region 130 < E_γ < 1896 keV.*

From Figure 6.13 it is observed that the 24 h Average BG subtracted, decay corrected, and normalised count rate in the energy region 130 keV < E_γ < 1896 keV does not remain constant. The normalised count rate decreases until approximately 1 March, then increases

until approximately 8 May after which an abrupt downward shift is observed. The Normalised count rate does not appear to be related to the reactor status. The inverse of the normalised count rate shows suspiciously similar behaviour to the gain drift observed in Figure 6.5 until approximately 8 May. The downward shift of the normalised count rate does not appear to be related to the gain drift and the cause is unknown. The behaviour of the ratios is not as expected and is most likely an instrumental effect.

6.5.2 HPGe detector

The spectra measured with the HPGe detector showed no effects of gain drift, indicating that the electronics of the HPGe detector system was more stable than the electronics of the NaI(Tl) detector system.

Figure 6.14 illustrates the excellent resolution of the HPGe detector but also the poor efficiency and low count rate in terms of the E_γ = 511, 1275 and 1786 keV peaks. The tiny E_γ = 1786 keV peak due to coincidence summing is indicated with an arrow.

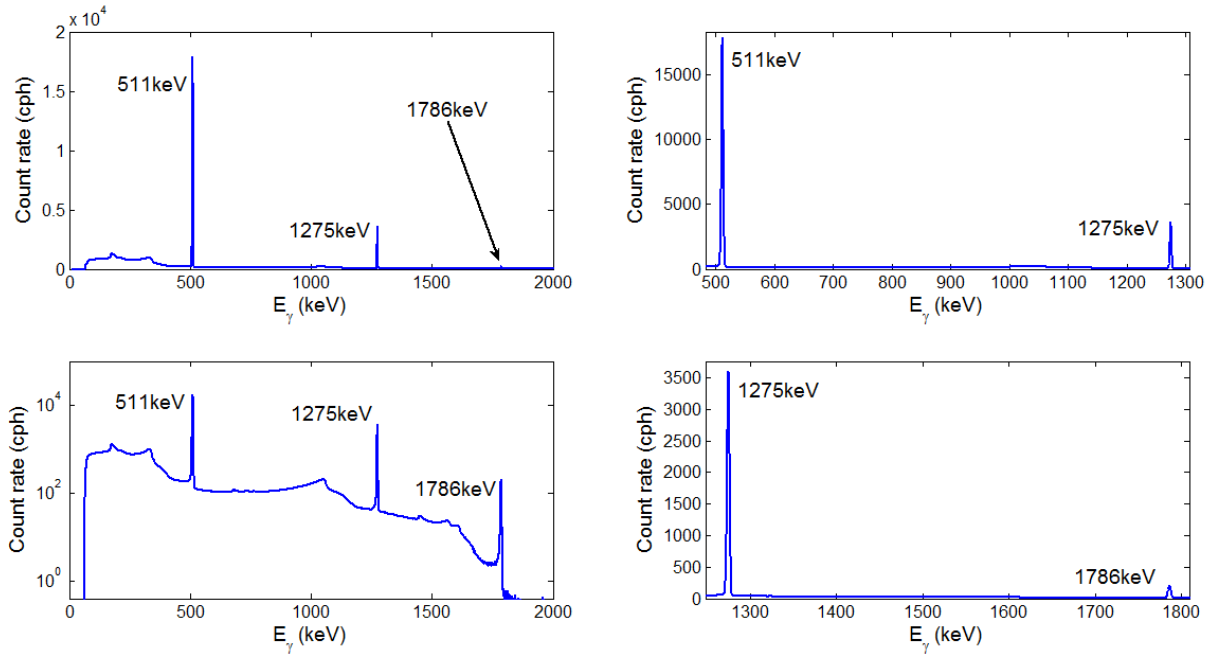

Figure 6.14: *A one-hour ^{22}Na spectrum measured with the HPGe detector. The top left and bottom left spectra are with linear and log scales respectively, the top right and bottom right spectra compare the size of the E_γ = 511, 1275 and 1786 keV peaks on a linear scale.*

Table 6.8 provides the net-peak count rates in a one-hour BG subtracted Na+BG spectrum measured with the HPGe detector.

Table 6.8: *Net-peak count rates in the E_γ = 511, 1275 and 1786 keV peaks of a one-hour BG subtracted Na+BG spectrum measured with the HPGe detector.*

	511 keV	1275 keV	1786 keV
Count rate (cph)	193500 (400)	33190 (180)	2370 (50)

Compared to the net-peak count rates obtained with the $LaBr_3$ detector, the count rate in the E_γ = 511, 1275 and 1786 keV peak is five times, fourteen times and fifty times smaller respectively with the HPGe detector. Even if Na+BG spectra were successfully measured during reactor-off, the low statistics in the full-energy peaks would not provide high enough precision to investigate changes in the net-peak ratios.

To investigate changes in the BG count rate the average BG count rate during the two BG measurement periods are determined in the energy regions $143 < E_\gamma < 1909$ keV, $143 < E_\gamma < 1568$ keV and $1569 < E_\gamma < 1909$ keV. Table 6.9 provides these count rates.

Table 6.9: *Average BG count rate during the two BG measurement periods in the energy regions $143 < E_\gamma < 1909$ keV, $143 < E_\gamma < 1568$ keV and $1569 < E_\gamma < 1909$ keV.*

Energy (keV)	16 – 21 Feb	29 Mar – 2 Apr
$143 < E_\gamma < 1909$	56310 (20)	57460 (20)
$143 < E_\gamma < 1568$	55580 (20)	56720 (20)
$1569 < E_\gamma < 1909$	727 (2)	739 (3)

Table 6.9 indicates an approximately 2% increase in the count rate in the energy regions $143 < E_\gamma < 1909$ keV and $143 < E_\gamma < 1568$ keV from February to April, confirming the 2% increase in the average BG count rate observed with the NaI(Tl) detector. The count rate in the energy region $1569 < E_\gamma < 1909$ keV increases by approximately 1.6%, slightly higher than observed with the NaI(Tl) detector. The measurement with the HPGe detector also confirms that the increase in the BG count rate is not related to the status of unit#1 since the increase is present during reactor-off as well as reactor-on periods. Sufficient BG data were not acquired to observe if the oscillations observed with the NaI(Tl) detector were also present in the BG measurement with the HPGe detector.

The excellent energy resolution of the HPGe detector allows for the identification of BG peaks under or close to the E_γ = 511, 1275 and 1786 keV peaks that could affect the net-peak count rates if BG changes are large enough, but as seen with the NaI(Tl) detector it was concluded that a 2% change in BG count rate does not affect the net-peak count rate in the BG subtracted Na+BG specta. Also, if the BG remains constant, subtraction of an average BG spectrum would get rid of these peaks and would not affect the net-peak count rates. Figure 6.15 shows an average BG spectrum measured with the HPGe detector.

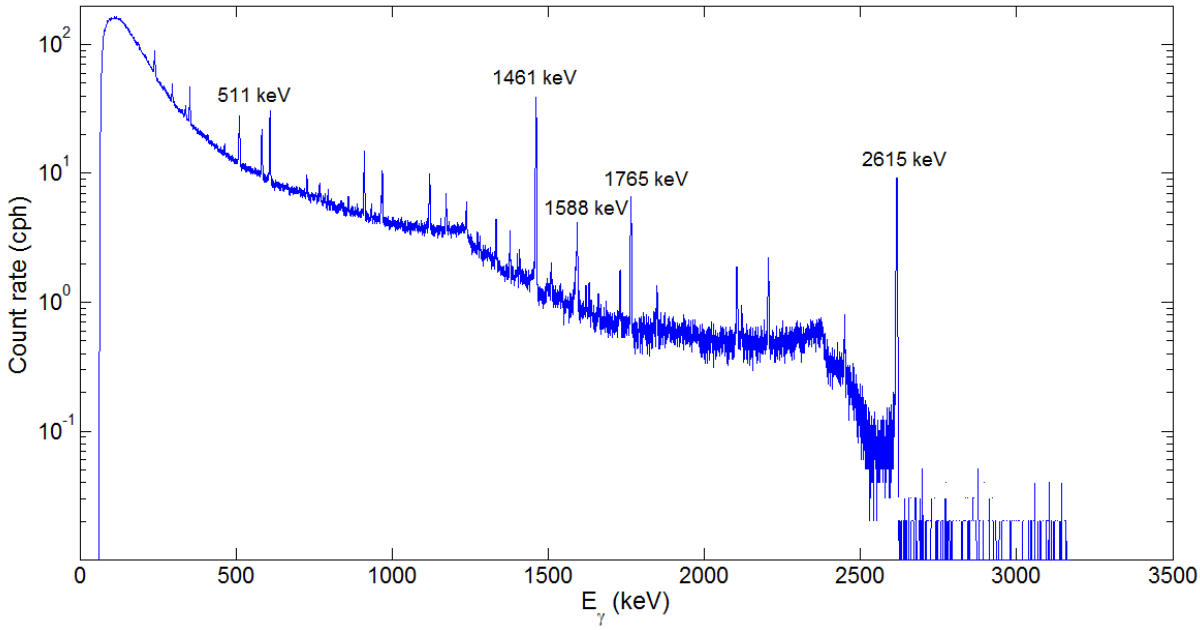

Figure 6.15: *Average BG spectrum measured with the HPGe detector. Indicated on a log scale are some of the most prominent peaks in the BG; E_γ = 511, 1461, 1588, 1786 and 2615 keV.*

Figure 6.15 contains many peaks resulting from the decay chains of the naturally occurring ^{235}U, ^{238}U and ^{232}Th. For an extensive list of peaks from natural BG radiation see reference [26] Handbook of radioactivity analysis p. 273. Indicated in Figure 6.16 is the E_γ = 511 keV peak resulting from β^+-annihilation, the E_γ = 1461 keV peak resulting from β^-decay of ^{40}K, the E_γ = 1588 keV peak resulting from β^-decay of ^{228}Ac, the E_γ = 1765 keV peak resulting from β^-decay of ^{214}Bi and the E_γ = 2615 keV resulting from β^-decay of ^{208}Tl.

6.6 Summary

Both measurement series 1 and 2 with the $LaBr_3$(Ce), NaI(Tl) and HPGe detectors have shown that the BG count rate increases by 2% and is not related to the status of the reactor. It was shown that the changing BG does not affect net-peak nor gross count rates in the BG subtracted Na+BG spectra. With the NaI(Tl) detector it was observed that oscillations in the BG count rate with a period of approximately 15 days occur, the cause of which is unknown. No correlation between the ratios and the reactor status was observed, though it appears that gain-drift has an effect on the count rates, even after spectrum stabilisation. Due to pile-up, reliable BG subtraction and energy calibration could not be achieved and the data were judged not to be of sufficient quality.

At Koeberg II an order of magnitude was gained in the antineutrino flux, $\phi_{\bar{\nu}_e} \sim 10^{13}$ $cm^{-2}s^{-1}$. According to equation 5.10, the relative change in the β^+ decay branch during measurement series 2 should increase by an order of magnitude (also assuming the uncertainty scales by an order of magnitude); $\frac{\Delta P_{\beta_1}}{P_{\beta_1}} = -0.0259$, if antineutrinos have an effect, with slightly less precision than obtained with the $LaBr_3$ detector due to the lower efficiency of the NaI(Tl) detector. Using this result, the exercise carried out in section 5.6.2 is repeated for investigating changes in the partial decay constants of ^{22}Na for case #1 and #2 at during measurement series 2, giving an indication of what could be expected. The results are presented in table 6.10.

Table 6.10: Change in the partial decay constants for case #1 and #2 as well as the corresponding interaction cross section for antineutrinos on the β^+ and electron capture decay branches of ^{22}Na, if antineutrinos were the cause. Also presented is the relative change in the decay constant.

Case #	$\Delta\lambda_1$ (s^{-1})	$\sigma_{\lambda 1}$ (barn)	$\Delta\lambda_2$ (s^{-1})	$\sigma_{\lambda 2}$ (barn)	$\Delta\lambda/\lambda$ (%)
1	-1.97×10^{-10}	20	1.97×10^{-10}	20	±2.6
2.1	-1.65×10^{-9}	206	0	N/A	-21.7
2.2	0	N/A	2.24×10^{-10}	28	+27.6

From table 6.10 it can be concluded that with an order of magnitude increase in the antineutrino flux at Koeberg II, changes in the partial decay constants and cross section upper

limits should decrease by an order of magnitude relative to Koeberg I, if antineutrinos are the cause. Since measurement series 3 was carried out in the same location as measurement series 2 (equivalent antineutrino flux), this order of magnitude increase in the cross section is also expected at Koeberg III using a NaI(Tl) well-counter where the efficiency has approximately doubled relative to the NaI(Tl) cylindrical crystal used at Koeberg II, therefore it is also expected that the sensitivity will increase and further reduce the cross section, if antineutrinos are the cause, this will be investigated in chapter 7.

CHAPTER 7 Measurement series 3: NaI(Tl) well-counter

7.1 NaI(Tl) well-counter properties

Measurement series 1 demonstrated that coincidence summing provides an improved method to measure the possible changes in the β^+-branching ratio of ^{22}Na. Compared to a typical cylindrical crystal, a well-counter provides an almost 4π solid angle ($\Omega \sim 4\pi$) which increases the absolute efficiency and effectively enhances coincidence summing and thereby the sensitivity to which changes in the β^+-branching ratio can be determined. For this reason, a third measurement series was carried out using a NaI(Tl) well-counter. The detector was specially manufactured for this measurement series and had the same properties as described in section 6.1. The detector was manufactured by SCIONIX Holland BV, model number BP102/3M-X. The crystal has a length of l = 102 mm and diameter of $\varnothing$ = 102 mm with an axial well having an inner diameter of $\varnothing_i$ = 12 mm and depth of d = 51 mm.

7.2 Experimental set-up

The well-counter was installed in the seismic vault, at the same location as the second measurement series; approximately l = 17m straight under the core of unit#1. The well-counter was enclosed with lead shielding consisting of three $\varnothing_i$ = 7.5 cm thick rings with dovetailed profiles and a dovetailed lid, resting on a steel tripod. The bottom ring has an opening with a diameter of $\varnothing_i$ = 85 mm allowing the PMT, its base and associated cables to be unobstructed. To further reduce background radiation, two $\varnothing$ = 50 mm thick lead discs were placed on top of each other 20 cm directly below the opening of the bottom ring.

Integrated into the base is a VENUS universal digital multichannel analyser which allows one to directly connect the base to a laptop/desktop via a USB cable. The DC voltage supplied via the USB cable allows the VENUS base to generate the high voltage for the detector. The USB cable also serves as a transfer of the digitised MCA output to the software running on the laptop. Detector settings are controlled by InterWinner nuclear spectroscopy software version 0.39 according to the software properties. The user has control over the high-voltage setting, course gain, fine gain, rise time and decay time via the InterWinner software. The following settings were recommended by SCIONIX Holland BV; high-voltage: +760 V, trigger filter rise time: 0.8 µs, energy filter rise time: 1 µs, fine gain: 0.6, decay time: 0.3 µs, baseline method: moving average, and baseline time: 3.2 µs. Applying a moving average to

the baseline allows real-time correction for baseline shifts. The software manual does not contain any information describing how settings such as trigger filter rise and energy filter rise time affect spectra, nor how the spectrum is stabilised.

An advantage and convenience of the VENUS base is that spectra are accumulated with real-time linear spectrum-stabilisation carried out by the software. Different spectrum-stabilisation settings were used for Na+BG and BG measurements because of the difference in spectral shape and count rate. For Na+BG measurements the $E_\gamma = 1275$ keV peak was chosen to serve as the reference peak since it is used during the analysis. The count rate of the $E_\gamma = 1275$ keV peak was integrated from $E_\gamma = 1240$ to 1310 keV ($\Delta E_\gamma = 70$ keV) with an uncertainty of 0.5 channels. The spectrum was stabilised when a minimum net area of 1000 counts was reached, corresponding to a stabilisation approximately every couple of seconds. For BG measurements the sharp peak at $E_\gamma \sim 1430$ keV, shown in Figure 7.3, provided the highest statistics to be used as a reference peak. The sharp peak was integrated from $E_\gamma = 1420$ to 1440 keV ($\Delta E_\gamma = 70$ keV) with a 0.5 channel uncertainty. The BG spectrum was stabilised when a minimum net area of 100 counts was reached, corresponding to a stabilisation approximately every 60 minutes. The 0.5 channel uncertainty was recommended by the InterWinner software creator, ITECH INSTRUMENTS, as well as the fine gain on the stabiliser which remained 0.5050 for Na+BG and BG measurements.

Figure 7.1: *The more compact set-up used for measurement series 3.*

The software also provides a real-time measure of the DC voltage, board temperature and high-voltage. The DC voltage and board temperature remained almost constant at DC = 4.73 V and $T_b = 41$ °C, respectively. The VENUS base provides a much more compact and simple set-up compared to the first two measurement series as shown in the photograph of Figure 7.1. Figure 7.1 shows the components of the set-up consisting of a laptop and lead shielding with the VENUS MCA base integrated well-counter inside.

A 2 kBq ^{22}Na source, manufactured in November 2012 at the Radionuclide Division of NRF iThemba LABS, is embedded in 3 mm thick aluminium to stop the positrons, wrapped with 1

mm lead to stop Bremsstrahlung and placed at the end of a plastic source holder that can be inserted and removed from the well.

Figure 7.2 shows a Na+BG spectrum measured with the well counter with the source inside the well (green) compared to a spectrum measured with the source outside, at the top of the well (blue).

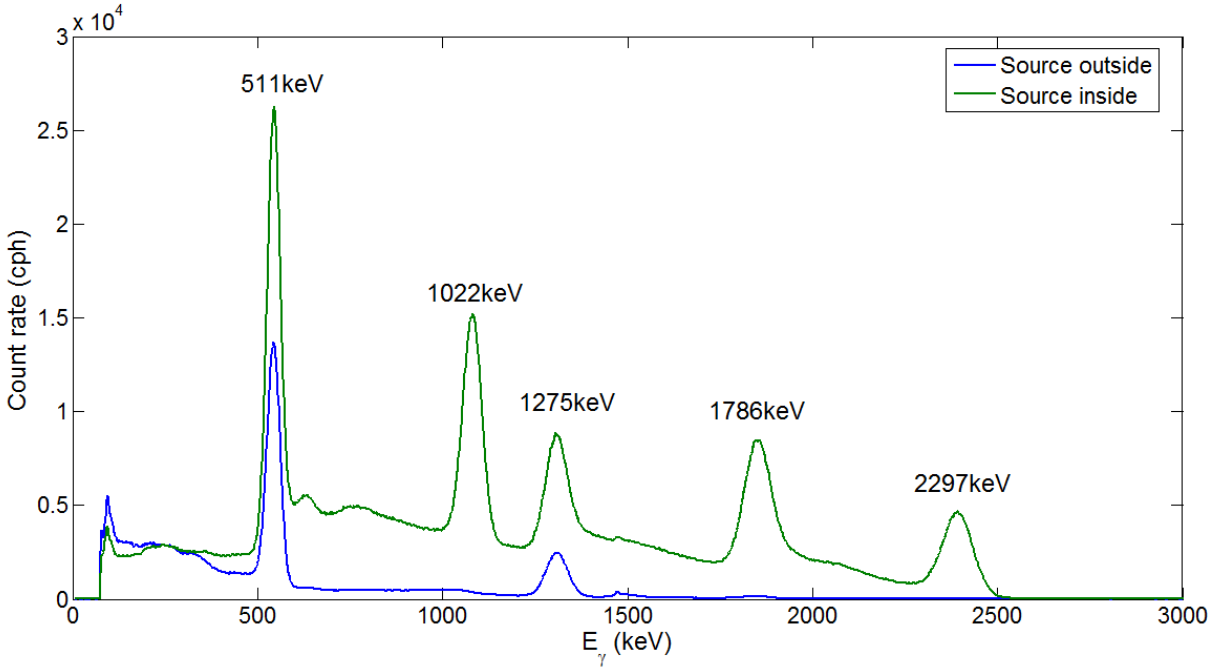

Figure 7.2: *The difference in coincidence summing with the well-counter with the source inside (green) and outside (blue) the well, respectively.*

The effect of coincidence summing inside the well-counter is clearly illustrated in Figure 7.2. β^+-decay results in the emission of a E_γ = 1275 keV γ-ray as well as two counter propagating E_γ = 511 keV photons following annihilation of the positron-electron pair. Electron capture also results in the emission of a E_γ = 1275 keV γ-ray. Each of the above mentioned photons resulting from β^+-decay is summed in coincidence with a combination of the other photons. Two E_γ = 511 keV photons are summed in coincidence resulting in a E_γ = 1022 keV peak if the E_γ = 1275 keV γ-ray escapes from the crystal. A E_γ = 1275 keV γ-ray is summed in coincidence with a E_γ = 511 keV photon resulting in a E_γ = 1786keV peak if the other E_γ = 511 keV photon remains undetected. A E_γ = 1275 keV γ-ray is summed in coincidence with two E_γ = 511 keV photons resulting in a E_γ = 2297 keV peak. The continuum parts occur if one or more of these photons deposits part of its energy via Compton scattering inside the crystal.

It is also interesting to note the repetition of the continuum shapes as continuum events are also added in coincidence. The E_γ = 1275 keV peak contains a mixture of E_γ = 1275 keV γ-rays from the β^+- and EC branches, while the region above the E_γ = 1275 keV peak is due to purely β^+-events feeding the E = 1275 keV level in ^{22}Ne.

In Figure 7.3 a Na+BG (source was inside the well) and BG spectra measured at Koeberg are compared. In the BG spectrum a E_γ = 511 keV peak is present which could result from the processes described in section 5.5. At E_γ = 1765 keV and 2615 keV the peaks resulting from the decay of ^{214}Bi and ^{208}Tl are observed in the BG spectrum. In the Na+BG spectrum the E_γ = 2615 keV peak is under the tail of the E_γ = 2297 keV triple coincidence peak.

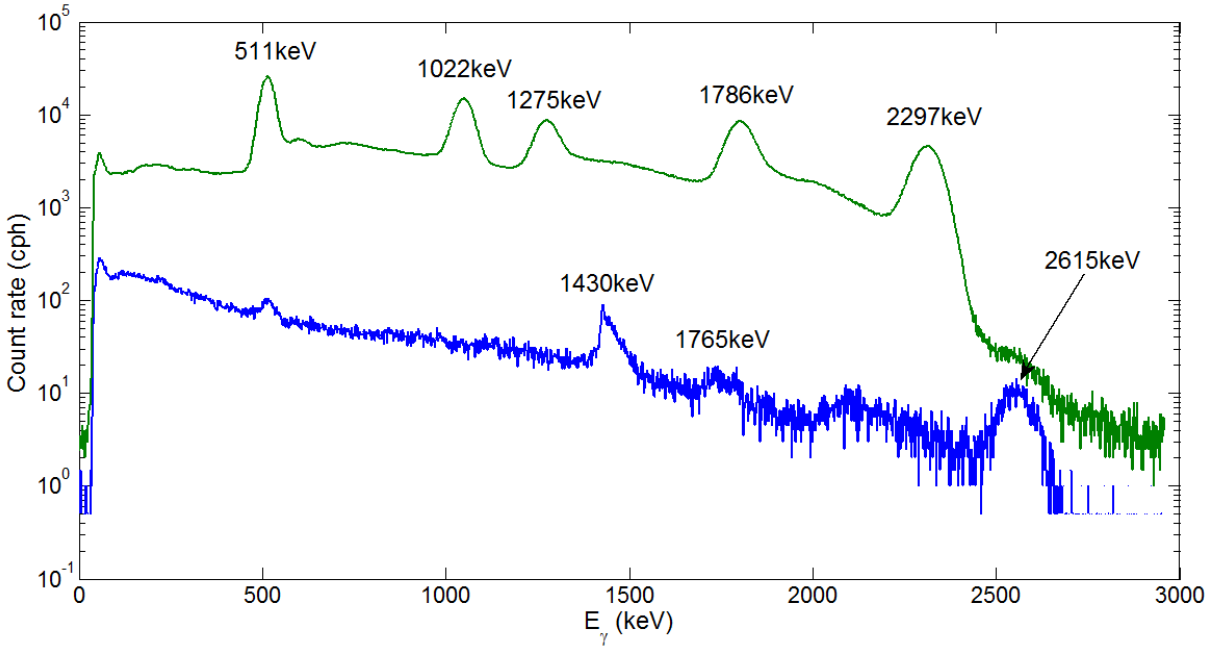

Figure 7.3: *A Na+BG (source inside the well) and BG spectrum measured at Koeberg plotted on a log scale.*

The high energy tail of the E_γ = 2297 keV peak extends past the E_γ = 2615 keV peak causing an increase in the count rate above the E_γ = 2615 keV peak in the Na+BG spectrum. Also observed in the BG spectrum is a sharp peak at E_γ ~ 1430 keV tailing towards the high energy side, covering the E_γ = 1461 keV peak resulting from the decay of ^{40}K. This unusually shaped peak is investigated in section 7.4. From Figure 7.3 it is also evident that BG only accounts for approximately 1% of the detector Na+BG count rate.

7.3 Measurement description

The well-counter arrived at NRF iThemba LABS on 02/11/2012 after which a period of detector and software testing and optimising commenced. Even though the next scheduled outage would only take place in November 2013 on unit#2, it was decided to install the detector at Koeberg power station in December 2012, for measurements of BG and Na+BG and wait for a possible unplanned outage. The most suitable date for the Koeberg collaborators to accommodate the detector installation at Koeberg was 11/12/2012. By this date the cause of the sharp peak at E ~ 1430 keV had not been identified.

The measurement started with Na+BG, while both units were operating at full power. On 14/12/2012 a BG measurement was started which lasted until 31/12/2012. Another Na+BG measurement was started on 03/01/2013 which lasted until 12/02/2013 when another BG measurement was started. On 21/02/2013 Koeberg communicated that unit#1 had gone into an unplanned shut down on 20/02/2013. The BG measurement was stopped on 21/02/2013 and a Na+BG measurement was started while unit#1 was off. Unit#1 was started up again on 17/04/2013 while Na+BG was still being measured. The Na+BG measurement concluded on 20/05/2013 when a third BG measurement was started. The BG measurement inadvertently stopped on 28/05/2013 and the laptop went into hibernation mode for a yet unknown reason. The BG measurement could only be restarted on 20/08/2013, lasting until 08/10/2013. Spectra were recorded in two-hour intervals and stored as InterWinner.SPE files on the hard drive of the laptop. These files can only be read with the InterWinner software installed on that specific laptop and were converted at the measuring location to more user friendly IAEA.SPE files which can be read with a wide range of programs. Table 7.1 provides a summary of the number of two-hour spectra recorded during the third measurement series which lasted approximately six months.

Table 7.1: *Summary of the quantity of data recorded with the NaI(Tl) well-counter during various phases of reactor operation of unit#1.*

Location	Date	Number of two-hour spectra	Type of spectrum	Power level of unit#1 (% of maximum)
Koeberg	11 – 14 Dec	34	Na+BG	100
Koeberg	14 – 31 Dec	200	BG	100
Koeberg	3 Jan – 12 Feb	478	Na+BG	100
Koeberg	12 – 21 Feb	109	BG	100
Koeberg	21 Feb – 17 Apr	658	Na+BG	0
Koeberg	17 Apr – 20 May	393	Na+BG	100
Koeberg	20 – 28 May	98	BG	100
Koeberg	20 Aug – 8 Oct	587	BG	100

A total of 731 two-hour BG spectra and 905 Na+BG spectra were obtained while unit#1 was operating at full power. While unit#1 was off, 658 two-hour Na+BG spectra were obtained.

7.4 Reliability of the data acquisition system

The InterWinner software provides real-time gain stabilisation and the gain correction factors can be retrieved as a function of time in a text file. Figure 7.4 shows the gain correction factor as a function of time applied to the BG and Na+BG spectra.

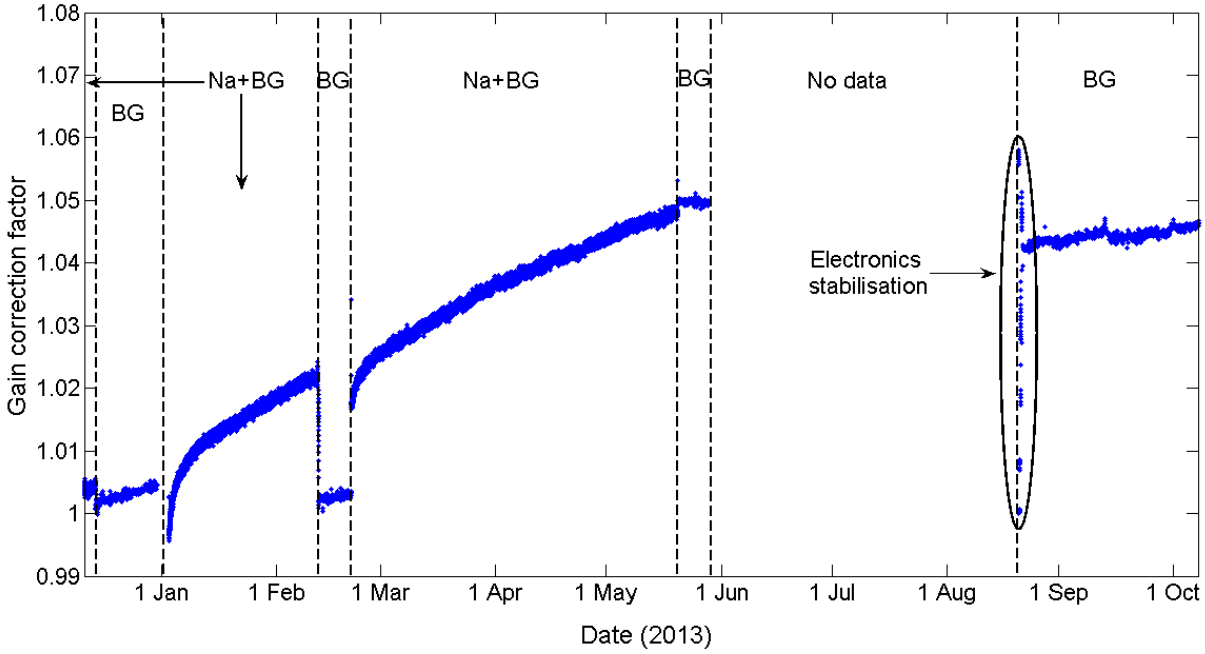

Figure 7.4: *Gain correction factors as a function of time, applied to the BG and Na+BG spectra.*

From Figure 7.4 it is observed that the gain correction factor has a general increasing tendency as a function of time when γ-rays resulting from the decay off ^{22}Na are measured. This means that the Na+BG spectra drift toward the low energy side as a function of time. Figure 7.4 also illustrates an exponential component in the spectrum drift, similar to what is observed in the peak drift experienced with the NaI(Tl) detector, illustrated in Figure 6.4. Considering that measurement series 2 and 3 were performed with the same type of crystal, at the same location and exhibit similar peak/spectrum drift behaviour, it seems that this type of exponential drift is inherent to the NaI(Tl) detectors, compared to the $LaBr_3$(Ce) and HPGe detectors. When γ-rays from ^{22}Na are measured, general exponential drift occurs, though after approximately 150 hours the drift appears to behave linearly. The drift of the BG spectra appears to be more stable, further supporting the claim that the drift is count rate dependent [81, 95], though the exponential drift observed when γ-rays from ^{22}Na are measured does not correspond to the 2.6 y half-life of ^{22}Na. For the BG spectra measured between 20 August

and 8 October, there is an initial period of erratic drift indicated by the ellipsoid, during which the electronics stabilise (warm up) after the period when the detector was not active. As such, the data collected during the warm up period is not reliable and not used during the analysis. The duration of electronics stabilisation is approximately 28 h. The initial Na+BG measurement from 11 to 14 December is not long enough to determine if the gain correction factor has similar behaviour to that of the following Na+BG measurements.

To investigate BG changes the hourly BG count rates in the energy region 143 < E_γ < 2958 keV are plotted as a function of time in Figure 7.5. Also indicated is the weighted mean during each BG period.

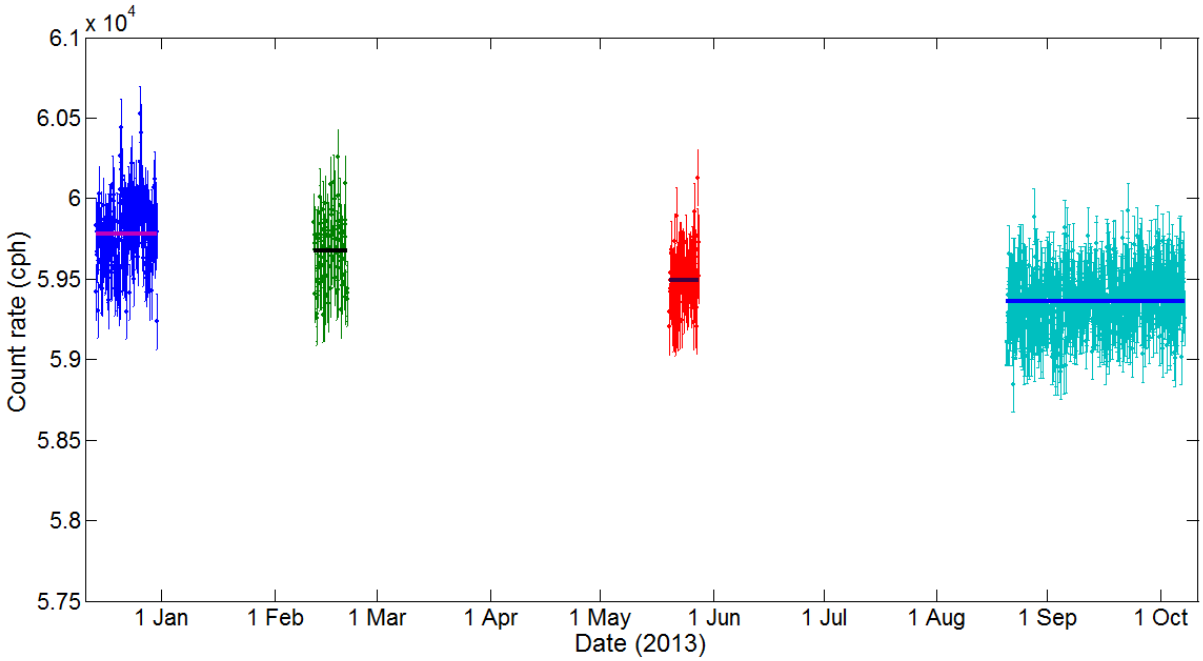

Figure 7.5: *Comparison of the hourly BG count rates in the energy region 143 < E_γ < 2958 keV while unit#1 was on. The weighted mean during each period is also indicated by the solid horizontal lines.*

Table 7.2 provides the weighted mean of the hourly count rates during each period as well as the χ^2-value relative to the weighted mean of the count rates.

Table 7.2: *Counting statistics of the hourly BG spectra in the energy region 143 < E_γ < 2958 keV during various periods while unit#1 is on.*

Date	wm (cph)	χ^2
14 – 31 Dec 2013	59777 (12)	1.54
12 – 21 Feb 2014	59676 (17)	1.34
20 – 28 May 2014	59493 (17)	0.97
20 Aug – 8 Oct 2014	59358 (7)	1.17

With χ^2-values of χ^2 = 1.54, 1.34, 0.97 and 1.17, respectively, it indicates that the BG count rates during the periods of 14 to 31 December, 12 to 21 February and 20 August to 8 October do not remain constant, whereas the BG during the period of 20 to 28 May does. The changes in BG during the various periods are most likely due to room BG variations caused by Radon level variations caused by changing ventilation over time. The mean of the count rates decreases by approximately 0.7% from December 2012 to October 2013. The BG changes are not related to the status of the reactor.

To determine the cause of the decrease in the mean count rate in the energy region 143 < E_γ < 2958 keV, the BG count rate in smaller energy regions is investigated. Firstly the effect of the sharp spurious BG peak on the BG count rate in the energy range 1352 < Eγ < 1914 keV is investigated. In Figure 7.6 the average BG spectra measured during the periods 14 to 31 December, 12 to 21 February, 20 – 28 May and 20 August to 8 October are compared.

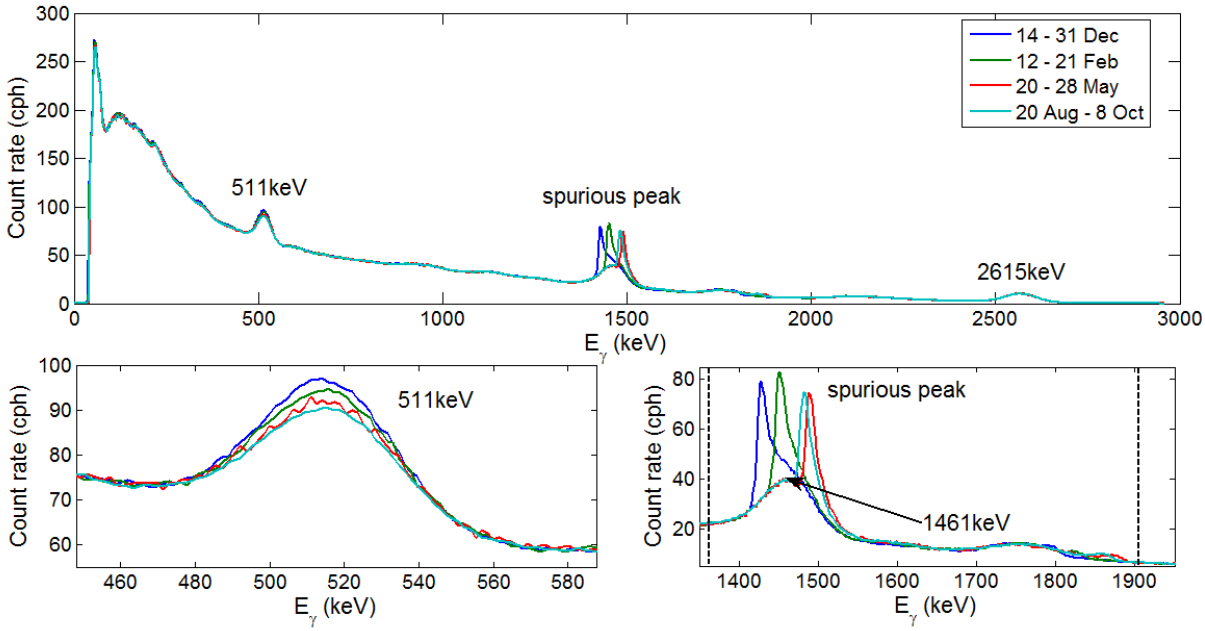

Figure 7.6: *Comparison of the average BG spectra during the four BG measurement periods. Indicated are the most prominent peaks at E_γ = 511 and 2615 keV, and also the spurious peak.*

The top panel in Figure 7.6 shows the full energy spectrum of the average BG spectra. Clearly seen is the shift of the spurious peak toward the high energy side until more than half of the E_γ = 1461 keV peak becomes uncovered during periods 20 to 28 May and 20 August to 8 October, indicated by the figure in the bottom right panel. The origin of the spurious peak is not clear, though it could be speculated that it is due to some setting on the InterWinner software and/or changes in cosmic-ray flux. Also noticed is what seems to be a tail toward the high energy side that shifts with the spurious peak, reaching approximately E_γ = 1900 keV. Zooming in on the E_γ = 511 keV peak as shown by the figure in the bottom left panel, it is observed that the intensity of the peak decreases from December 2012 to October 2013. Table 7.3 provides the count rates in the energy range 1352 < Eγ < 1909 keV as well as the net-peak count rates of the E_γ = 511, 1173, 1333 and 2615 keV peaks during the four BG measurement periods in an attempt to isolate the energy regions most affected by BG changes. Also included are the count rates in the energy regions 143 < Eγ < 467 keV and 574 < Eγ < 1352 keV (between the Eγ = 511 and 1461 keV peaks), respectively.

Table 7.3: *Net-peak count rates of Eγ = 511, 1173, 1333 and 2615 keV peaks in the average BG spectra as well as the count rate in the energy regions 143 < Eγ < 467 keV, 574 < Eγ < 1352 keV and 1352 < Eγ < 1909.*

Energy (keV)	14 - 31 Dec	12 – 21 Feb	20 – 28 May	20 Aug – 8Oct
511	769 (6)	723 (8)	656 (9)	632 (5)
1173	146 (8)	184 (11)	170 (11)	181 (7)
1333	105 (5)	94 (6)	110 (7)	98 (4)
2615	602 (3)	607(4)	611 (4)	604 (3)
143 < Eγ < 467	24931 (8)	24830 (11)	24760 (11)	24695 (7)
574 < Eγ < 1352	19372 (7)	19330 (9)	19348 (10)	19323 (6)
1352 < Eγ < 1909	7258 (4)	7269 (6)	7263 (6)	7260 (4)

Table 7.3 indicates that the net-peak count rate of the E_γ = 511 keV peak decreases by approximately 15% from December 2012 to October 2013. The count rate in the energy range 143 < Eγ < 467 decreases by approximately 1% from December 2012 to October 2013 and is most likely related to the decrease in count rate of E_γ = 511 keV peak. The net-peak count rate of the E_γ = 1173, 1333, 2615 keV peaks as well as the count rate in the energy regions 574 < Eγ < 1352 keV and 1352 < Eγ < 1909 keV remain constant.

In Figure 7.7 an attempt is made to observe if any oscillations in the BG count rate, similar to that seen with the NaI(Tl) detector, during measurement series 2, occur. Figure 7.7 shows the 24 h average BG count rates during the various BG measurement periods in the energy region 143 < E_γ < 2958 keV.

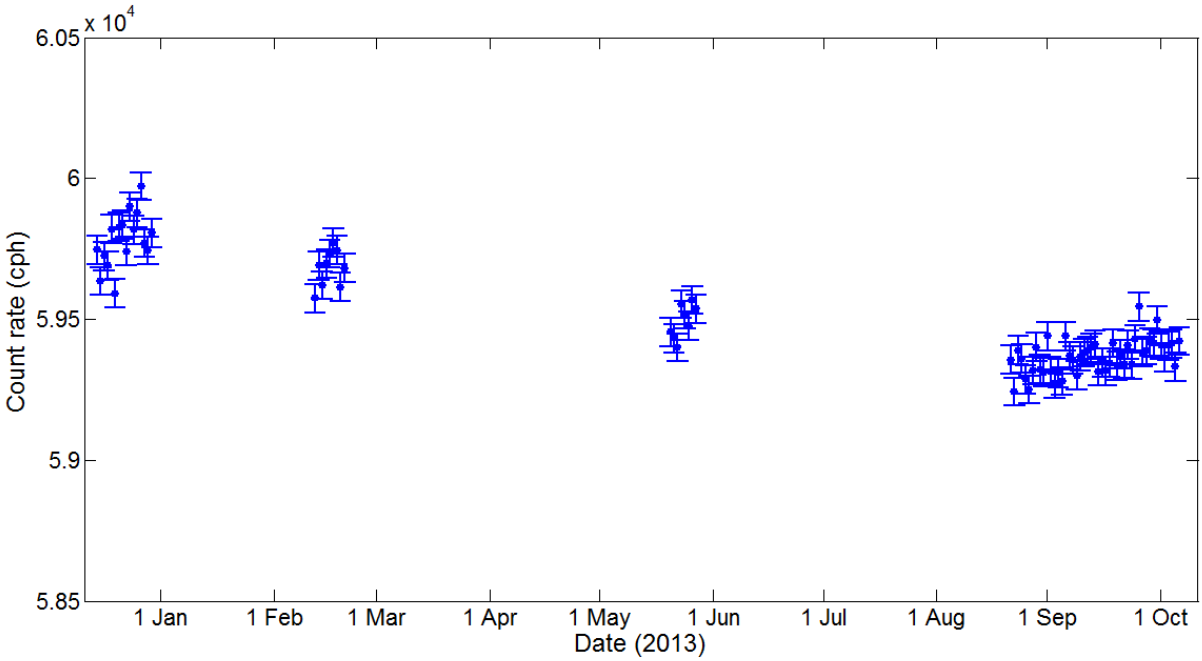

Figure 7.7: *24 h Average average BG count rates during the various BG measurement periods in the energy region 143 < E_γ < 2958 keV.*

The first three BG periods are less than twenty days long, while the period from 20 August to 8 October is more than a month long and no clear oscillations are observed.

From Table 7.2 it was concluded that the BG count rate does not remain constant and that the change in total average BG count rate from December 2012 to October 2013 is less than 1%. Table 7.4 provides the net peak count rate of the E_γ = 511, 1022, 1275, 1786 and 2297 keV peaks determined from a one-hour BG corrected Na+BG spectrum using average BG from 14 to 31 December 2012 and 20 August to 8 October 2013, respectively, to illustrate the effect of applying a BG subtraction on net-peak count rates as well as the gross count rate in the energy region 143 < E_γ < 2958 keV. The results from these two BG periods are compared since they show the largest difference in BG count rate.

Table 7.4: *Net-peak count rates of the E_γ = 511, 1022, 1275, 1786 and 2297 keV peaks as well as the gross count rate in the energy region 143 < E_γ < 2958 keV, determined from a one-hour BG corrected Na+BG spectrum using average BG from 14 to 31 December 2012 and 20 August to 8 October 2013, respectively.*

	ave BG 14 – 31 Dec	ave BG 20 Aug – 8 Oct
Energy (keV)	Count rate (cph)	Count rate (cph)
511	554800 (800)	554800 (800)
1022	448300 (800)	448200 (800)
1275	280300 (800)	280000 (800)
1786	385600 (800)	385600 (800)
2297	258500 (700)	258400 (700)
143 < E_γ < 2958	6060500 (1700)	6000800 (1700)

Table 7.4 shows that the net-peak count rates of the E_γ = 511, 1022, 1275, 1786 and 2297 keV peaks as well as the gross count rate in the energy region 143 < E_γ < 2958 keV are not affected by a changing BG count rate of approximately 1%. The average BG during each period delivers the same net-peak count rates within uncertainties. Typical count rates in a one-hour Na+BG and BG spectrum are approximately N(Na+BG) = 0.6×10^7 cph and N(BG) = 0.6×10^5 cph, respectively. Therefore the BG count rate represents approximately 1% of the count rate in a Na+BG spectra. From the above results it can be concluded that applying a BG subtraction using BG spectra differing by approximately 1% in count rate does not significantly affect net-peak count rates and even to a lesser extent the gross count rates, since the systematic effect of a linear continuum subtraction is eliminated. The BG measured during the various periods are therefore summed and averaged into an average BG spectrum which is subtracted from the Na+BG spectra.

7.5 Experimental results

Figure 7.8 shows the regions of interest used to determine the ratio of count rates in the BG subtracted Na+BG spectra. Gate I: 1366 < E_γ < 1931 keV and Gate II: 1931 < E_γ < 2475 keV. Gate I and II contain contributions resulting from β^+-decay only, therefore the ratio of the count rates in Gate I and II should remain constant as a function of time and independent of antineutrino flux.

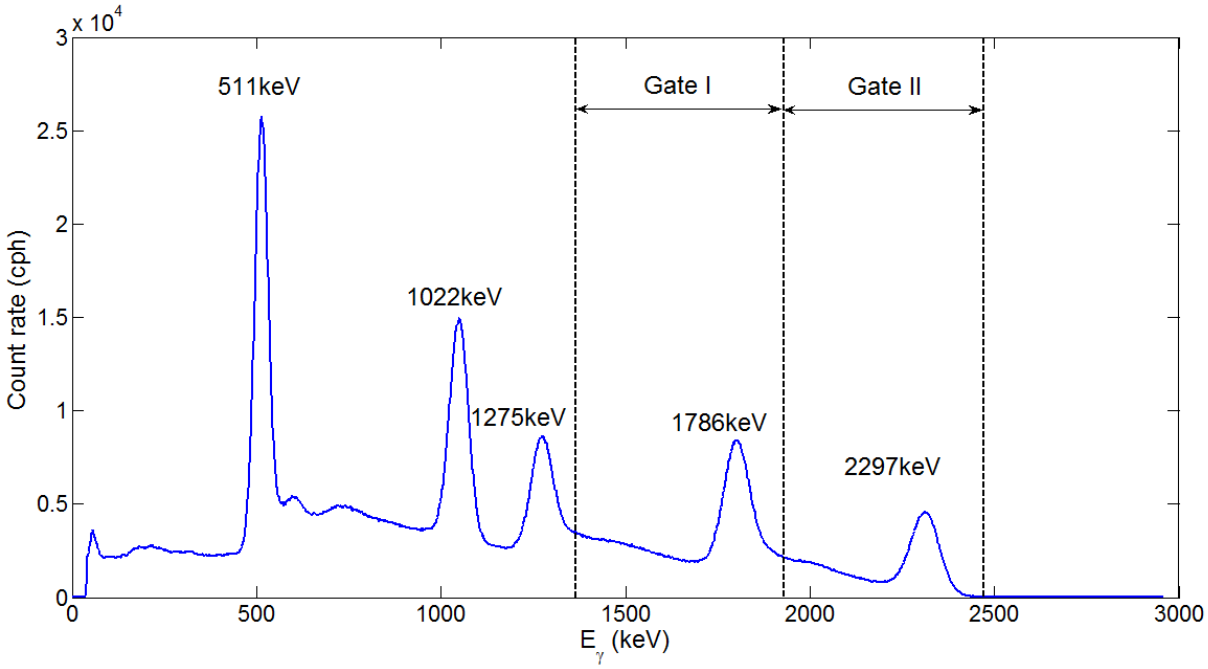

Figure 7.8: *Regions of interest used to determine the ratio of count rates in the BG corrected Na+BG spectra.*

The E_γ = 1275 keV peak contains contributions from β^+-decay as well as EC. If either of the β^+ or EC decay branches are affected, the ratio of the gross count rate of the E_γ = 1275 keV (166 < E_γ < 1366 keV) peak and Gate I and II should also be affected. Gate I and II are chosen to avoid the systematic uncertainty in applying a linear continuum subtraction to the E_γ = 1786 and 2297 keV peaks, and also provide higher statistics which allow a more sensitive measurement of the ratios. The same holds for the gross count rate of the E_γ = 1275 keV peak which contains contributions from EC and β^+-decay. In summary, the gross count rate of the E_γ = 1275 keV peak and Gate I and II are used since they provide the most sensitive measure for changes in the ratios by avoiding the systematic uncertainty of a linear continuum subtraction.

Figure 7.9 shows the ratio of the gross count rates in Gate I, Gate II and the E_γ = 1275 keV peak as a function of time.

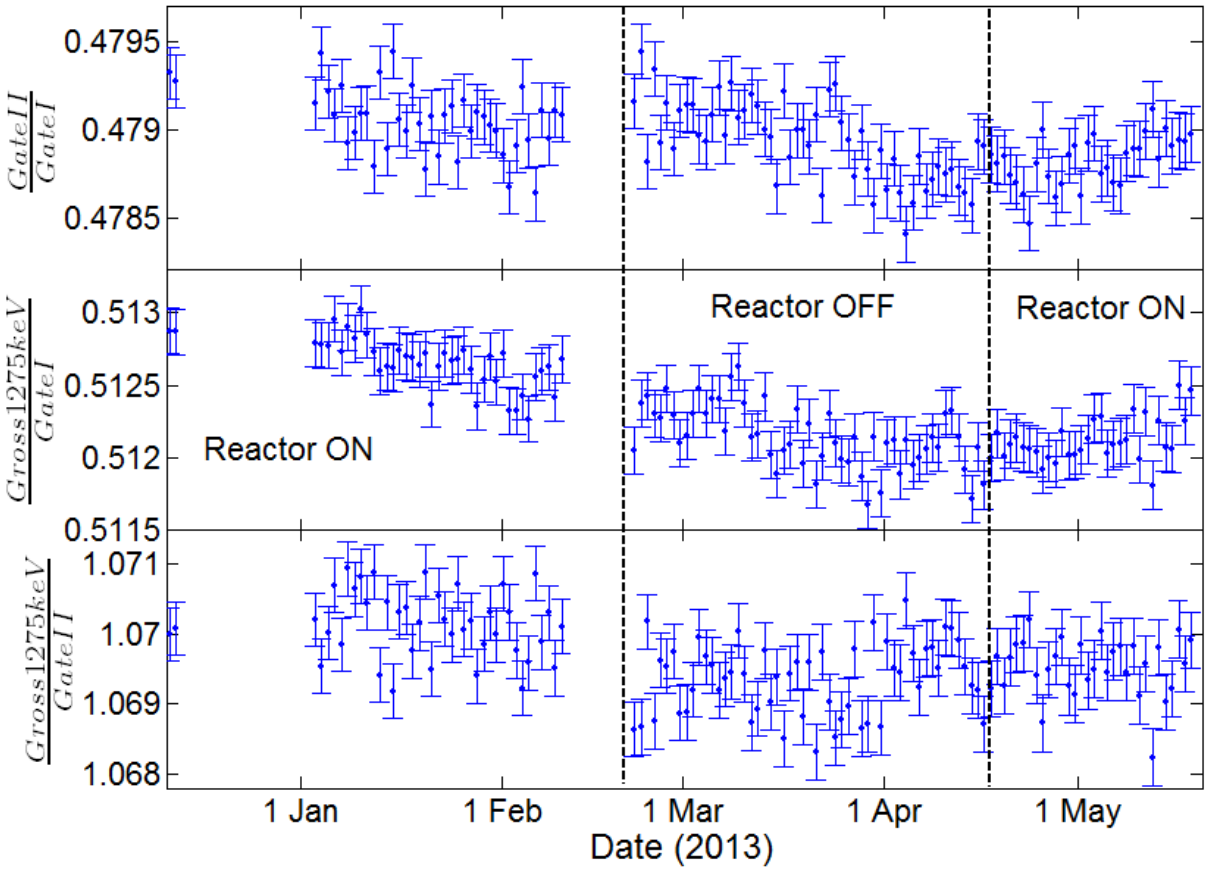

Figure 7.9: *24 h Average ratio of the gross count rates in Gate I, Gate II and the E_γ = 1275 keV peak as a function of time, while unit#1 makes the transition from on to off and back on again.*

From Figure 7.9 it is evident that none of the ratios remain constant and appear not to be related to the reactor status. On approximately 10 April the ratios of $\frac{\text{Gross 1275 keV}}{\text{Gate I}}$ and $\frac{\text{Gross 1275 keV}}{\text{Gate II}}$ show a slight hump. If the ratios are not affected by changes in antineutrino flux, it could be that the count rate in the numerator and/or denominator of the ratios is affected by some other mechanism. To explore this possibility, the gross-count rates in Gate I and II and the E_γ = 1275 keV peak are corrected for decay and normalised, presented in Figure 7.10.

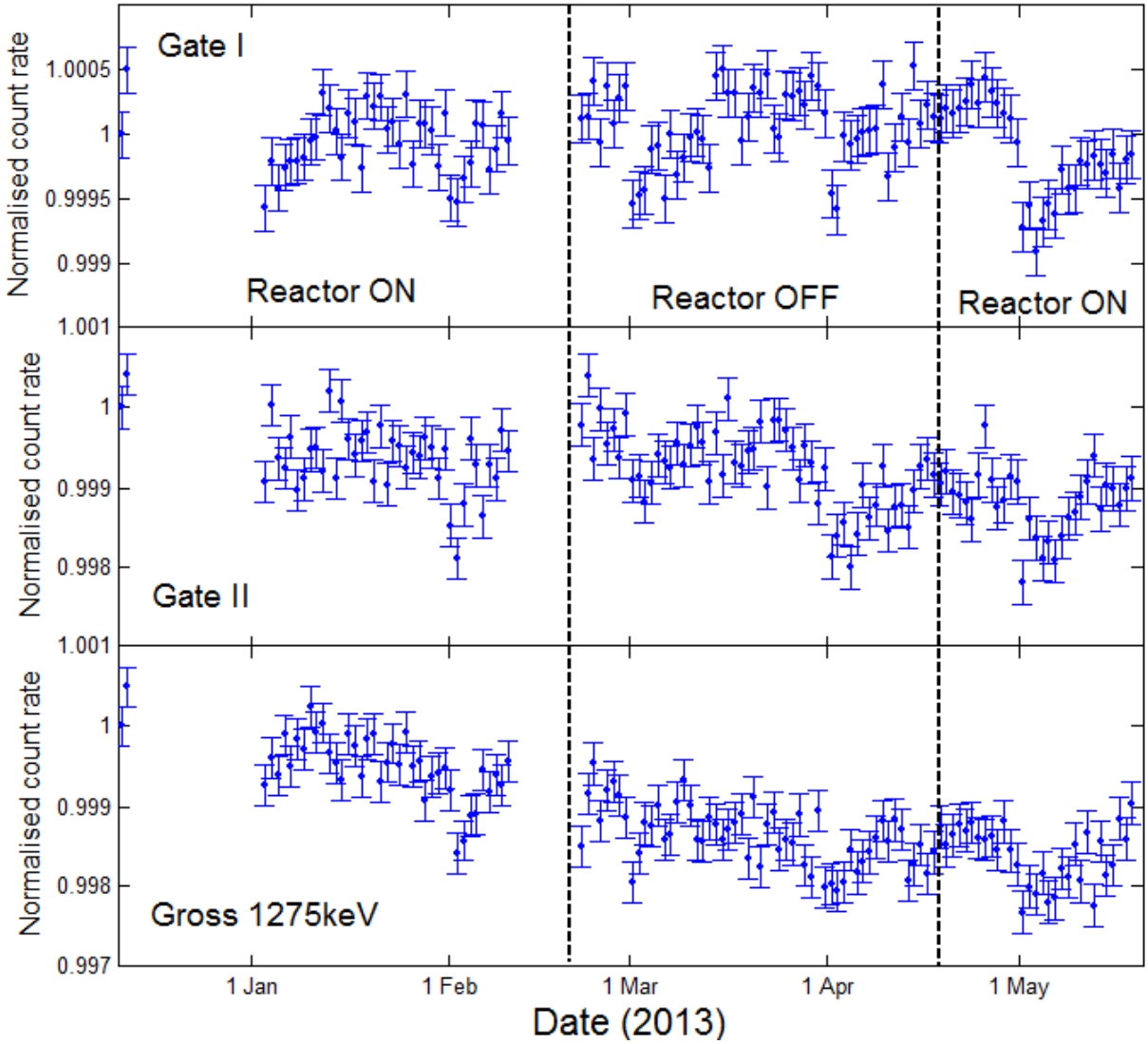

Figure 7.10: *Decay corrected and normalised count rates in Gate I and II and the E_γ = 1275 keV peak.*

Figure 7.10 shows that at approximately the beginning of each month dips occur in the count rate in Gate I and II as well as the E_γ = 1275 keV peak. The dips have a period which is equal to the length of the specific month. In Gate I the dip structure is repeated monthly, though on approximately 1 May the dip structure exhibits a slight downward shift that lowers the count rate. In Gate II the dip structure exhibits a slight downward shift on 1 April. The dip structure in the E_γ = 1275 keV peak is repeated without any shift, though it exhibits a generally decreasing trend. Because the dips in the count rates occur at approximately the same dates, the ratio of the count rates will not show any dip structure, though the effect of the shifts of the dip structures is visible in the ratio of the count rates. Most noticeably the effect is seen in

the ratios containing the count rate in Gate II, at approximately 1 April, where shifts in the ratios of $\frac{\text{Gross 1275 keV}}{\text{Gate II}}$ and $\frac{\text{Gate II}}{\text{Gate I}}$ are observed.

Further investigation of the decay corrected and normalised count rates in smaller energy regions in the Na+BG spectra revealed that the dip structure is present in the entire spectrum, only that the amplitude of the dips changes. Therefore, to obtain better statistics, the count rate in the energy region $143 < E_\gamma < 2475$ keV in the Na+BG spectra are decay corrected and normalised, shown in Figure 7.11.

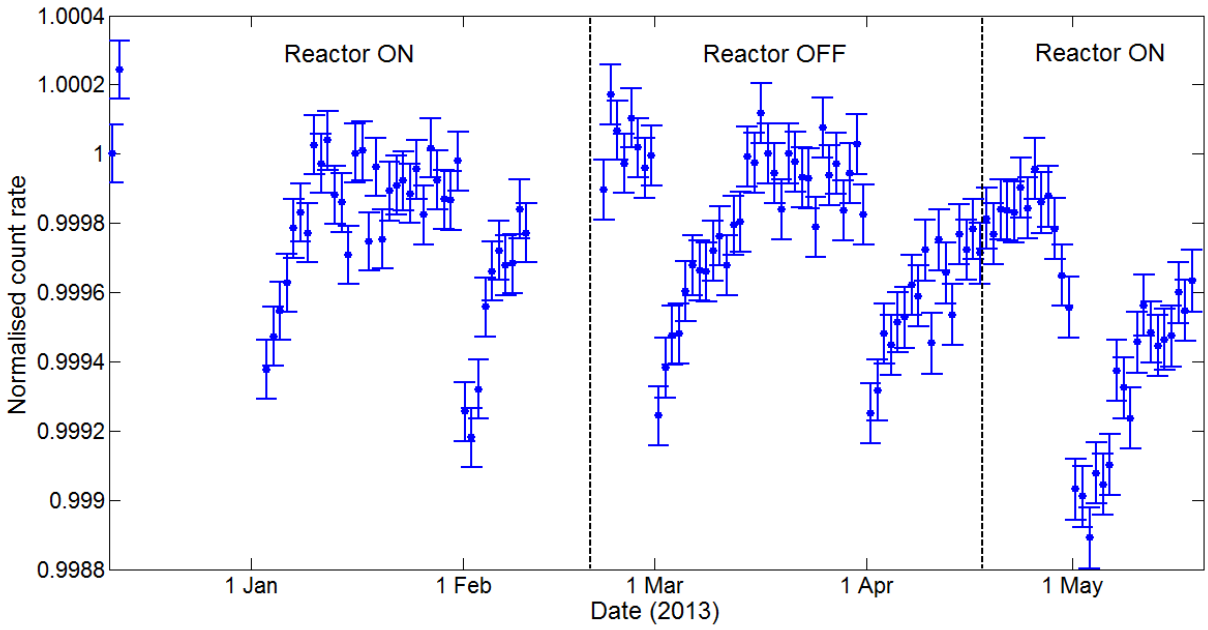

Figure 7.11: *Decay corrected and normalised count rate in the energy region 143 < E_γ < 2475 keV.*

From Figure 7.12 it is observed that the downward shift of the dip structure on 1 May is also present in the energy region $143 < E_\gamma < 2475$ keV. The relative size of the shift is approximately 0.04%, while the amplitude of the dips is approximately 0.1%. A 0.1% change in the Na+BG count rate requires a 10% change in the BG count rate, if the dips are caused by BG changes. Table 7.5 provides the count rate in the energy region $143 < E_\gamma < 2475$ keV in the average BG spectra during the various BG measurement periods.

Table 7.5: *Count rate in the energy region 143 < E_γ < 2475 keV in the average BG spectra during the various BG measurement periods.*

Period	14 – 31 Dec	12 – 21 Feb	20 – 28 May	20 Aug – 8 Oct
Count rate (cph)	58860 (12)	58681 (16)	58570 (17)	58428 (11)

Table 7.5 indicates that the average BG count rate decreases from December 2012 to October 2013 by approximately 0.7%, well below the 10% required to cause a 0.1% change in the Na+BG count rate. Therefore changes in BG are not the cause of the dips. The dips are not observed in the BG count rate due to the low statistics, but it is present when measuring ^{22}Na; which provides better statistics and sensitivity.

Figure 7.12 shows the half-life of ^{22}Na corresponding to the changes in count rate in the energy region 143 < E_γ < 2475 keV. Also indicated by the solid horizontal line is the literature value of the half-life of ^{22}Na (2.6027 (0.0010) y) [1].

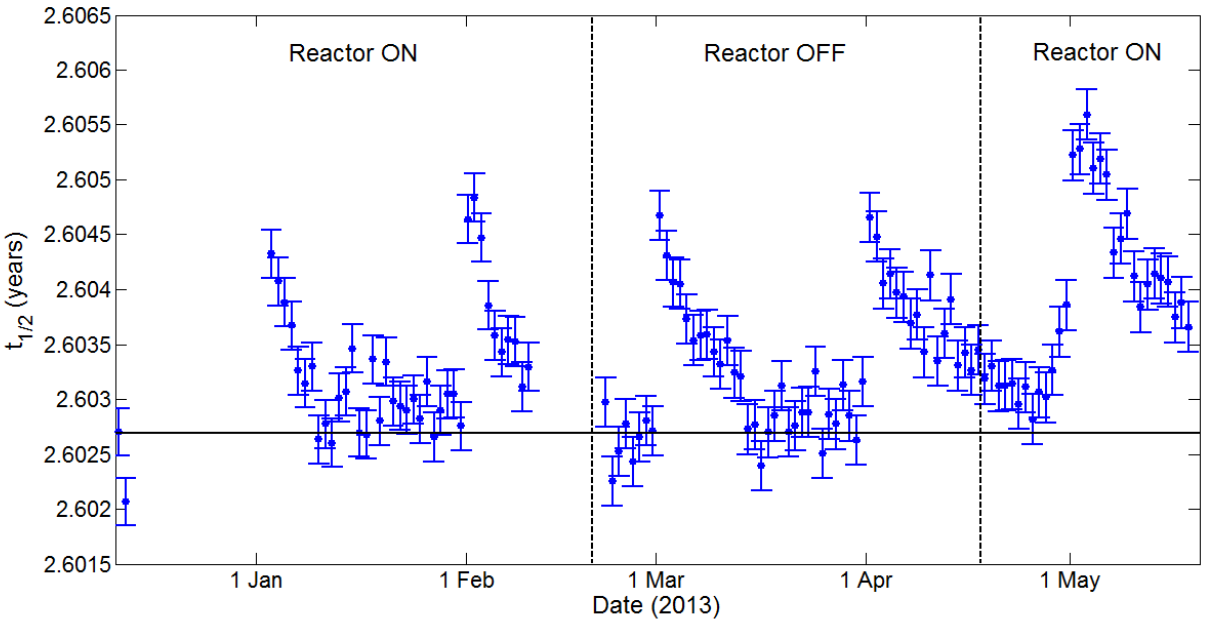

Figure 7.12: *Half-life of ^{22}Na corresponding to the changes in count rate observed in the energy region 143 < E_γ < 2475 keV. The literature value of the half-life of ^{22}Na (2.6027 (0.0010) y)[1] is indicated by the solid horizontal line.*

From Figure 7.12 it appears as though ^{22}Na is decaying with a variable half-life which is not correlated with the reactor status or changes in BG count rate. As the count rate increases, the half-life decreases and the maximum change in half-life is approximately 0.1%.

The dips occur on the first of each month. In an attempt to isolate the cause of the dips, the gain correction factor is investigated for similar dip structures which could affect the count rate in a spectrum. Figure 7.13 shows the 24 h average gain correction factor applied to the Na+BG spectra as a function of time.

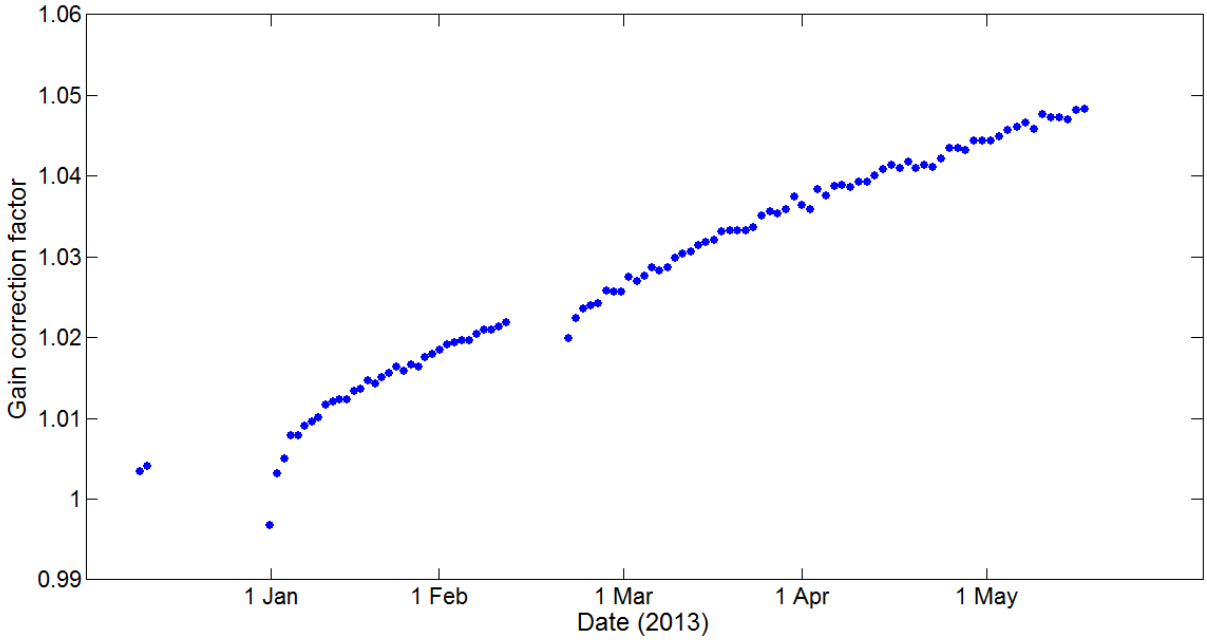

Figure 7.13: *24 h Average gain correction factor applied to the Na+BG spectra as a function of time.*

From Figure 7.13 it is clear that no dip structures similar to what is seen in the count rates are observed. The gain correction factor shows many increases and decreases throughout the Na+BG measurement periods, not only at the beginning of each month. Na+BG spectra have been compared before, during and after a dip and no off-set between the spectra has been observed. Therefore, gain changes or inaccurate gain stabilisation can be eliminated as a cause of the dip structures.

Another factor that could change count rates is changes in the dead time of the detection system. Figure 7.14 shows the 24 h average dead time during the Na+BG measurement periods as a function of time.

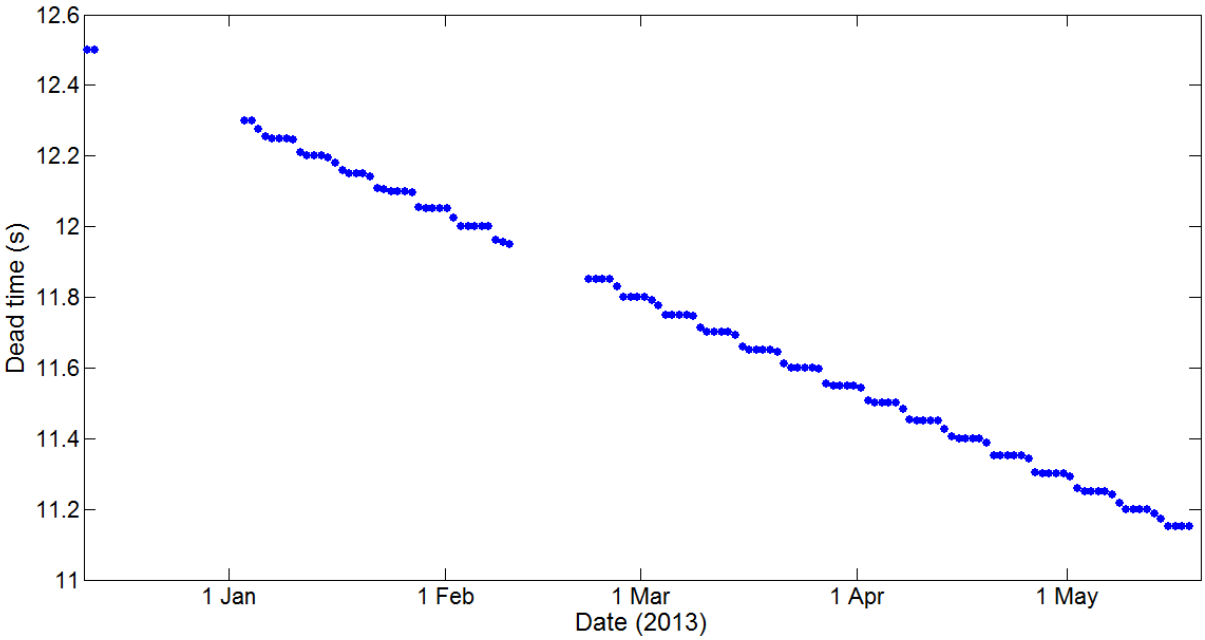

Figure 7.14: *24h Average dead time during the Na+BG measurement periods.*

Figure 7.14 indicates that the average dead time decreases by approximately 1.3 s from December 2012 to May 2013. The decrease in dead time is expected since the source is decaying; therefore the count rate in the detector is always decreasing. Also observed from Figure 7.14 are steps in the dead time with a period of approximately 6 days. These oscillations are due to the rounding off of the dead time to two decimals by the InterWinner software. From Figure 7.14 it can be concluded that changes in the dead time of the detection system is not the cause of the dips in the count rate.

It is suspicious that the dips always occur abruptly on the first of each month, indicating that the dips are somehow related to the timing system used by the InterWinner software or operating system of the laptop, though this still has to be proven. Recently it has been established that a certain back-up and recovery program is scheduled in Microsoft's Windows 7 task scheduler to start at 12h00 PM on the first of each month, coinciding with the start of a dip. This is the only process scheduled to start on the first of each month and it could be that this program affects the InterWinner time keeping i.e. slowing the clock down therefore increasing the γ-ray measurement time. The next logical step would be to disable this task and check if the dips disappear, though the result of this check will not be covered in this thesis.

Comparing the ratios in figure 7.9 with the normalised and decay corrected count rates in figure 7.10, it appears that the effect of the dip structures is reduced when the ratio is taken, but not completely eliminated because of the varying amplitude and shape of the monthly dip structures. To obtain an estimate of the systematic effect of the dip structures or any instrumental effect, the ratio of $\frac{\text{Gate II}}{\text{Gate I}}$ is investigated. This ratio contains events due to β^+-decay only, therefore it is expected that this ratio remains constant and independent of antineutrino flux. Figure 7.9 shows that this ratio starts to decrease around 23/03/2013, weeks before reactor start-up. The period 21/02/2013 to 20/05/2013 represents a period of continuous measurement of Na+BG as the reactor went from off to on, during which the ratio $\frac{\text{Gate II}}{\text{Gate I}}$ should remain constant. The unexpected decrease could be due to a systematic effect. The size of the systematic effect is estimated by comparing the mean of the ratio $\frac{\text{Gate II}}{\text{Gate I}}$ before and after the start of the decrease during this period of continuous Na+BG measurement. Table 7.6 presents the mean of the ratio $\frac{\text{Gate II}}{\text{Gate I}}$ between 21/02/2013 and 23/03/2013 and the mean between 24/03/2014 and 20/05/2013.

Table 7.6: *Mean of the ratio $\frac{Gate\ II}{Gate\ I}$ before and after the start of the decrease in this ratio.*

Period	Mean
21/02/2013 - 23/03/2013	0.47905 (0.00003)
24/03/2013 - 20/05/2013	0.47879 (0.00002)

From table 7.6 a 0.05% statistical difference is observed between the mean before and after the start of the decrease in the ratio. From this an estimate for the size of a systematic effect on the ratios is set as at least 0.05%. From this result the ratio $\frac{\text{Gross 1275 keV}}{\text{Gate I}}$ is corrected by 0.05% from 24/03/2013 to 20/05/2013. Table 7.7 presents the mean of the ratio $\frac{\text{Gross 1275 keV}}{\text{Gate I}}$ between 21/02/2013 and 23/03/2013 and the corrected mean between 24/03/2013 to 20/05/2013.

Table 7.7: *Mean of the ratio* $\frac{\text{Gross 1275 keV}}{\text{Gate I}}$ *before and after a correction of 0.05% for the period between 24/03/2013 and 20/05/2013.*

Period	mean (before)	mean (after)
21/02/2013 - 23/03/2013	0.51225 (0.00004)	N/A
24/03/2013 - 20/05/2013	0.51208 (0.00002)	0.51233 (0.00002)
% difference before and after	0.03	0.02

Table 7.7 shows that the mean increases by 0.01% after applying a 0.05% correction in the period 24/03/2013 to 20/05/2013. Now the corrected mean is used to determine the difference in the mean ratio $\frac{\text{Gross 1275 keV}}{\text{Gate I}}$ between reactor-off and-on. Results are presented in table 7.8.

Table 7.8: *Mean of the corrected ratio* $\frac{\text{Gross 1275 keV}}{\text{Gate I}}$ *during reactor-off and-on.*

Period	Mean
Reactor-off	
21/02/2013 - 17/04/2013	0.51225 (0.00003)
Reactor-on	
17/04/2013 - 20/05/2013	0.51235 (0.00003)

Table 7.8 shows a 0.02 (0.0005)% statistical difference in $\left|\frac{\Delta\lambda}{\lambda}\right|$, corresponding to 4σ, in the mean of the ratio $\frac{\text{Gross 1275 keV}}{\text{Gate I}}$ between reactor-off and-on, though as deduced from figure 7.12 a maximum 0.1% change in the half-life of ^{22}Na due to the dip structures is expected.

The corresponding cross section for a 0.02% change in the decay constant is estimated from equation 5.7; $\sigma_i = \frac{|\Delta\lambda_i|}{\Delta\phi_{\bar{\nu}_e}}$ at an antineutrino flux increase of $\Delta\phi_{\bar{\nu}_e} = 10^{13}$ cm^{-2}s^{-1}, resulting in σ = 0.2 (0.4) barn as an upper limit. The uncertainty was determined through propagation of uncertainties consisting of counting statistics, a 10% uncertainty in the antineutrino flux, a 0.03% uncertainty in the literature value of the decay constant of ^{22}Na [1] and a minimum 0.05% uncertainty in the decay constant due to systematic effects. From this it can be concluded that the 0.02% change in the decay constant of ^{22}Na between reactor-off and-on is most likely due to systematic effects.

Table 7.9 provides a summary of the results obtained during the three measurements at Koeberg relative to the objective of improving the sensitivity obtained by de Meijer *et al*. at Delft [21].

Table 7.9: *Comparison of results obtained at Koeberg relative to that obtained by de Meijer et al.[21].*

Measurement	σ (barn = 10^{-24} cm^2)
de Meijer *et al*.	30 (30)
Koeberg 1	2 (5)
Koeberg 2	20 (50)
Koeberg 3	0.2 (0.4)

Table 7.9 shows that measurement series 1 increased the sensitivity obtained by de Meijer *et al*. by an order of magnitude, whereas measurement series 2 increased the sensitivity by a factor 1.5. Through measurement series 3 the goal of lowering the upper limit by at least two orders of magnitude was achieved. Measurement series 3 proved to be the most sensitive measurement resulting in an upper limit of 0.2 barn. This upper limit is also an order of magnitude smaller than that obtained by Jenkins *et al.* and supports the findings of Norman *et al*. for no significant influence of antineutrinos affecting β^+-decay [4, 7].

7.6 Summary

Measurements with the well-counter revealed that none of the ratios remain constant and that dips in the count rate occur on the first of each month when measuring Na+BG. The behaviour of the dips determines how the ratios are affected. The BG measurements do not show the monthly dips due to the low statistics in the BG. The maximum size of a systematic effect of the dip structures on the decay rate of ^{22}Na was deduced as 0.1% and a lower bound of 0.05%. It was also shown that the BG count rate changes at most by 1% which is not large enough to explain the dips in the BG subtracted and decay corrected, normalised Na+BG count rates. The changes in the ratios and the dips are not related to the status of the reactor. It has also been shown that the dips are not related to changes in the BG count rate, gain changes or inaccurate gain stabilisation and also not changes in the dead time of the detection system.

Measurement series 3 also shows the danger of analysing data at face value, without being involved in the particular measurement and without any knowledge of the experimental settings, conditions and processes that affect collection. Without access to in-depth information such an artifact could be wrongly interpreted as an effect of 0.1% on the decay rate of ^{22}Na.

Measurement series 3 proved to be the most sensitive of the three measurements series increasing the sensitivity obtained by de Meijer *et al.* by two orders of magnitude. The effect observed during measurement series 1 was not reproduced. An upper limit for the cross section was determined as 0.2 barn.

CHAPTER 8 Conclusions and outlook

The goal of this project was to investigate reports of neutrinos influencing decay rates by exposing a ^{22}Na source to a changing reactor antineutrino flux and measuring certain ratios of γ-ray count rates resulting from the decay of the source.

8.1 The learning curve

From measurement series 1 an upper limit for the cross section of antineutrino interaction with ^{22}Na was determined as the order of barns, similar to the effect reported by Jenkins *et al*. An attempt was made to confirm and/or lower this upper limit with two follow-up measurements. For measurement series 2 an increased effect by an order of magnitude was expected (due to the poor quality of data caused by pile-up and radiation damage, making a BG subtraction unreliable) and an upper limit of the order of 20 barn was determined for the cross section. Measurement series 3 showed the best sensitivity (due to higher precision and order of magnitude increase in antineutrino flux for detecting changes in the ratios from which an upper limit for the cross section was set at 0.2 barn, an order of magnitude smaller than the Jenkins effect and two orders of magnitude smaller than observed by de Meijer *et al*. at the Delft reactor [4, 21]. During all three measurement series instrumental obstacles were encountered. Table 8.1 provides the pros and cons of each measurement series.

Table 8.1: *Pros and cons of measurement series 1 to 3.*

Measurement series 1		Measurement series 2		Measurement series 3	
Pros	Cons	Pros	Cons	Pros	Cons
$LaBr_3$ fast detector	Intrinsic BG		NaI slow detector	High efficiency	NaI slow detector
High count rates	Faulty AMP		Low count rates	Compact set-up	Low count rates
Reduced pile-up	Bulky		Pile-up	No NIM electronics	Pile-up
Reduced dead-time			Dead-time		Dead-time
Gain stability			Sensitive to unstable gain caused by temperature and count rate changes		Sensitive to unstable gain caused by temperature and count rate changes
			Radiation damage		Inaccurate time keeping
			Bulky		
	No temperature and humidity control or record		No temperature and humidity control or record		No temperature and humidity control or record

From table 8.1 and the experience gained during the three measurement series as well as working at the National Metrology Institute of South Africa, recommendations for improvements on future measurements of the type employed in this work can be made. The detector should have a fast response, short decay time, minimal intrinsic BG, not be affected by count rate, temperature and humidity changes and have a high efficiency. In addition, constant environmental conditions are preferred and should be monitored for the duration of the measurement. Moreover, stable electronics is required and should also be monitored i.e. high voltage, gain, pole-zero and BLR. Continuous BG measurements should be made during

reactor-off and-on periods using a second detector in order to accurately assess the influence of BG changes while source count rates are measured. Seasonal atmospheric density changes are known to cause cosmic-ray related BG changes at ground level [111]. High statistics measurements are sensitive to small count rate changes, which would otherwise have gone unnoticed. Realistically it is difficult to meet all these criteria and compromises have to be made. These measures should be employed for the purpose of quality assurance, reproducibility and traceability. To further ensure accurate measurements, systematic uncertainties should be taken into account, not only statistical. For this purpose an uncertainty budget should be set-up where the contribution of systematic uncertainty components are investigated and quantified and added in quadrature to the statistical uncertainty. Systematic factors during the Koeberg measurements were addressed in chapters 5 to 7 and can generally lead to the wrong interpretation of results.

The above mentioned procedures for quality assurance, reproducibility and traceability are employed by accredited metrology institutes where accuracy determines excellence. Investigations into systematic components can occur as separate measurements, before or after real measurements are made or by introducing a small change in the parameters going into a calculation and recalculating the desired quantity.

8.2 2014 PTB results

Recent results of measurements on the activity of ^{36}Cl performed at the Physikalisch-Technische Bundesanstalt (PTB) metrology institute of Germany show an order of magnitude smaller effect on the decay rate of ^{36}Cl compared to what Jenkins *et al.* observed and conclude that there is no solar influence on the decay rate of ^{36}Cl [112]. The measurements performed at PTB coincidentally overlap in time with the data set analysed by Jenkins *et al.* and no oscillations were observed either [112]. The measurement technique employed is known as the Triple to Double Coincident Ratio (TDCR) method and is an absolute primary method for determining activity. The TDCR system consisted of three photomultiplier tubes which surround a liquid scintillation vial containing ^{36}Cl, measuring triple and double coincidences, the ratio of which can be used to determine the activity [112]. It is also concluded in Ref. [112] that the Jenkins effect is due to the experimental set-up in that a Geiger-Müller counter (used to collect the data analysed by Jenkins *et al.*) shows instability to measuring low-energy radiation such as that resulting from the electron capture and β^- decay of ^{36}Cl [112]. The electronic components are also sensitive to environmental

conditions that could cause gain changes and therefore cause changes in the detector response. Instability in the high voltage supply could also cause changes in the detection efficiency [112]. Other factors such as self-absorption within the source also depend on environmental conditions [112]. The paper also highlights the fact that a GM counter is not designed for high precision decay rate measurements and that there was a lack of control environmental parameters during the data collected by Jenkins *et al*. [112].

8.4 Conclusions and outlook

The experience gained from the Koeberg measurements as well as the results from PTB show that one cannot simply use and interpret data blindly without knowing the conditions under which the data were collected and not take systematic effects into consideration, especially when performing high precision measurements. Low counting statistics can mask effects such as the dip structures seen during measurement series 3 that can lead to the wrong interpretation of results. The appropriate equipment and measurement technique have to be selected depending on what the objective of the measurement is.

Considering the results from PTB showing no effect on the decay rate of ^{36}Cl which decays by β^- decay as well as electron capture, which is also a decay mode of ^{22}Na, it is highly unlikely that the effect observed during measurement series 1 is related to an antineutrino effect. A more probable cause is the replacing of the amplifier or changes in BG while the γ-rays from ^{22}Na were being measured. The 0.2 barn upper limit obtained during measurement series 3 supports the findings of Norman *et al*. for no significant influence of antineutrinos affecting β^+-decay.

Many articles reporting contradicting decay rate results have become available and no final answer has been reached [3, 4, 5, 6, 7, 8, 9, 10, 11, 12, 13, 14, 15, 16, 17, 18, 19, 20, 113]. It is clear that further investigation is needed. In working towards Weinberg's suggestion and testing the influence of antineutrinos on decay rates, the best place for measurements is at a reactor but under controlled conditions employing possible alternative absolute methods such as TDCR and $4\pi\beta\gamma$ or improved spectral analytical methods. If Weinberg's suggested method for measuring the cosmic neutrino background is ever to be realised, many more measurements such as these need to be made at reactors to work towards the levels of accuracy and precision required for such measurements to be made in space, the same holds for reactor monitoring and investigating the existence of so-called sterile neutrinos. Typical

cross sections involved in weak interactions are of the order of 10^{-43} cm^2, although more sensitive measurements are needed, the upper limit achieved in this work still needs to be improved on by sixteen orders of magnitude to be comparable to weak interaction cross sections. To improve on cross section measurements, measurements could be made at higher antineutrino flux, using more efficient detectors, increasing the number of detectors, increasing the measuring time and also by using longer lived radionuclides such as ^{26}Al which has a half-life of 7.17×10^5 years [1]. The longer half-life allows a measurement where the number of nuclei available for antineutrino interaction can be increased without increasing the count rate in the detector. Using a radionuclide with such a slow decay rate, where over the course of a year the activity would not change significantly, external influences on the decay rate should become more apparent. Future measurements could also test the effect of antineutrinos on other decay modes.

Absolute primary measurements have now been proven to be reliable and controlled and provides an alternative to spectral analyses and should be investigated. The NMISA has facilities to perform absolute measurements which can be undertaken to investigate changes in the decay rate of various radionuclides if a solar neutrino influence is to be investigated. Furthermore, international comparisons between metrology institutes measuring sources made up from a common master solution can be made parallel in time using the same or different electronics, software, analytical methods and environmental conditions to investigate long term decay rate variations. Through this process instrumental effects can be tested.

In conclusion, we find no significant evidence for an effect of antineutrinos on the decay rate of ^{22}Na, considering the instrumental obstacles encountered during each measurement. Further investigation into decay rate variations is needed. The research carried out over the past 3 – 4 years was definitely scintillating, although not by coincidence.

REFERENCES

[1] National Nuclear Data Center: http://www.nndc.bnl.gov/chart/

[2] Philip J. Aston, "*Is radioactive decay really exponential?*", *Europhysics Letters 97*, 52001 (2012).

[3] Alburger, D.E. *et al.*, 1986, "*Half-life of ^{32}Si*", Earth and Planetary Science Letters 78, p168-176.

[4] Jenkins, J.H. *et al.*, "*Evidence for correlations between nuclear decay rates and earth-sun distance*", Astroparticle Physics 32, 42 (2009).

[5] Peter S. Cooper, "*Searching for modifications to the exponential radioactive decay law with the Cassini spacecraft*", Astroparticle Physics 31, 267 (2009).

[6] A.G. Parkhomov, Journal of Modern Physics, 2011, 2, 1310-1317.

[7] Norman, E.B. *et al.*, "*Evidence against correlations between nuclear decay rates and Earth-Sun distance*", Astroparticle Physics 31, 135 (2009).

[8] Semkow, T.M. *et al.*, "*Oscillations in radioactive exponential decay*", Physics Letters B 675 (5), p415-419.

[9] Jenkins, J.H. *et al.*, "*Analysis of environmental influences in nuclear half-life measurements exhibiting time-dependent decay rates*", 2010, Nucl. Instr. and Meth. A620, 332.

[10] Fischbach, E. *et al.*, "*Evidence for solar influences on nuclear decay rates*", CPT AND Lorentz Symmetry. Edited by V Alan Kostelecký (Indiana University, USA). Published by World Scientific Publishing Co. Pte. Ltd., 2011. ISBN #9789814327688, pp. 168-173.

[11] Jenkins, J.H., Additional experimental evidence for a solar influence on nuclear decay rates, Astroparticle Physics, Volume 37, September 2012, Pages 81-88.

[12] Jenkins, J.H. *et al.*, "*Additional experimental evidence for a solar influence on nuclear decay rates*", *Astroparticle Physics* ***37,*** 81 (2012).

[13] O'Keefe, D. *et al.*, "*Spectral Content of 22Na/44Ti Decay Data: Implications for a Solar Influence*", Astrophysics and Space Science April 2013, Volume 344, Issue 2, pp 297.

[14] Sturrock, P.A., et al., "*Comparative study of beta-decay data for eight nuclides measured at the Physikalisch-Technische Bundesanstalt*", Astropart.Phys. 59 (2014) 47-58 (2014).

[15] Sturrock, P.A., et al., "*A Possible Role of Neutrinos in Stimulating Beta Decays and its Significance for Solar Physics*", American Astronomical Society, AAS Meeting #224, #211.02.

[16] O'Keefe, D., "*Spectral Content of $^{22}Na/^{44}Ti$ Decay Data: Implications for a Solar Influence*", *et al.* Astrophys.Space Sci. 344 (2013) 297-303.

[17] Sturrock, P.A., et al., "*An analysis of apparent r-mode oscillations in solar activity, the solar diameter, the solar neutrino flux, and nuclear decay rates, with implications concerning the Sun's internal structure and rotation, and neutrino processes*", Astroparticle Physics, Volume 42, p. 62-69.

[18] Sturrock, P.A., et al., "*Analysis of Gamma Radiation from a Radon Source: Indications of a Solar Influence*", Astropart.Phys. 36 (2012) 18-25.

[19] Krausse, D.E., et al., "*Searches for solar-influenced radioactive decay anomalies using Spacecraft RTGs*", Astropart.Phys. 36 (2012) 51-56.

[20] H. Siegert, H. Schrader, U. Schotzig, Appl. Radiat. Isot. 49 (1998) 1397.

[21] de Meijer, R.J., Blaauw, M., Smit, F.D., "*No evidence for antineutrinos significantly influencing exponential β^+-decay*", Applied Radiation and Isotopes, 69 (2), p320-326.

[22] Weinberg, S., 1962, Phys. Rev. 128, p1457.

[23] Cocco, A.G., *et al*., "*Probing Low Energy Neutrino Backgrounds with Neutrino Capture on Beta Decaying Nuclei*", J. Phys. Conf. Ser. 110 (2008).

[24] Zuber, K., 2004, Neutrino Physics, 1st Edition, Taylor & Francis, Inc, New York.

[25] Martin, B., 2009, "*Nuclear and Particle Physics: An Introduction*", 2nd Edition, John Wiley & Sons, Inc. New York.

[26] Annunziata, M.F., 2003, "*Handbook of Radioactivity Analysis*", 2nd Edition, Academic Press.

[27] Bilenky, S.M., The European Physical Journal H, April 2013, Volume 38, Issue 3, pp 345-404.

[28] Das, A and Ferbel, T., 2003, *"Introduction to nuclear and particle physics"*, 2nd edition, World Scientific.

[29] Povh, B., Rith, K., Scholz, C., Zetsche., F., 2008, "*Particles and nuclei: An Introduction to the Physical Concepts*", 6th edition, Springer-Verlag Berlin Heidelberg.

[30] Braibant, S., Giacomelli, G., Spurio., M., 2012, "*Particles and Fundamental Interactions: An Introduction to Particle Physics*", Springer Dordrecht Heidelberg London New York.

[31] Goldhaber, M., Grodzins, L., Sunyar, A.W., Helicity of Neutrinos, 1958, *Phys. Rev.* 109 1015.

[32] Kaufman, L.J., "*Recent results in neutrinoless double beta decay*", Proceedings, 32nd International Symposium on Physics in Collision (PIC 2012), Strbske Pleso, Slovakia, September 12-15, 2012, p 180-189.

[33] Doi, M. and Kotani, T., 1992, *Prog. Theor. Phys.* 87 1207 .

[34] Doi, M. and Kotani, T., 1993, *Prog. Theor. Phys.* 89 139.

[35] Proceedings of the Carolina Symposium on Neutrino Physics: Its Impact on Particle Physics, Astrophysics and Cosmology, 2000.

[36] Close, F., 2010, "*Neutrino*", Oxford University Press Inc., New York.

[37] Europhysics news, Vol 43, number 4, p 23, 2012.

[38] Maltoni, M, Schwetz, T, T´ortola, M, Valle, Jos´e W. F, "*Status of global fits to neutrino oscillations*", *New J. Phys.* 6 122 (2004).

[39] Smirnov, A. Yu, "*The MSW effect and Solar Neutrinos*", 2005 *Phys. Scr.* 2005 57.

[40] Eguchi, K, *et al.*, "*First Results from KamLAND: Evidence for Reactor Anti-Neutrino Disappearance*", Phys.Rev.Lett. 90 (2003).

[41] Gando, A., "*Constraints on θ_{13} from A Three-Flavor Oscillation Analysis of Reactor Antineutrinos at KamLAND*", Phys. Rev. D 83 (2011).

[42] Ahn, J.K., *et al*., "*Observation of Reactor Electron Antineutrinos Disappearance in the RENO Experiment*", PRL 108, 191802 (2012).

[43] An, F.P., *et al*., "*Observation of Electron-Antineutrino Disappearance at Daya Bay*", PRL 108, 171803 (2012).

[44] Mention, G., *et al*., "*The Reactor Antineutrino Anomaly*", Phys. Rev. D 83 (2011).

[45] Bahcall, J. N. and Pinsonneault, M. H., Phys. Rev. Lett. 92, 121301 (2004).

[46] Scholberg, K., "*Supernova Neutrino Detection*", *J. Phys. Conf. Ser.* 375 (2012).

[47] Lunardini, C, "*The Diffuse Supernova Neutrino Flux*", The Proceedings of the 22nd International Conference on Neutrino Physics and Astrophysics, 2011.

[48] Villaescusa-Navarro, F., *et al*., Journal of Cosmology and Astroparticle Physics, 1303 (2013).

[49] Faessler, A., *et al*., Rom.J.Phys. 58 (2013) 9-10.

[50] Coan, T.E. and Ye, J., Muon Physics, sacarter.soe.ucsc.edu/sites/default/files/Muon%20physics_0.pdf, 20/12/2013, 15h30.

[51] Gaisser, T.K., Stanev, T., and Tilav, S., Front.Phys.China 8 (2013) 748-758.

[52] Cecchini, S., and Spurio, M., Geoscientific Instrumentation, Methods & Data Systems (GI);2012, Vol. 1 Issue 2, p185.

[53] Huang, Y., Chubakov, V., Mantovani, F., Rudnick, R.L. and McDonough, W.F., 2013, "*A reference Earth model for the heat-producing elements and associated geoneutrino flux*", Geochem. Geophys. Geosyst., 14, doi:10.1002/ggge.20129.

[54] McDonough, W. F., 2003, "*The Mantle and Core"*, edited by C. R. W. (Elsevier Pergamon, Oxford), volume 2 of *Treatise on Geochemistry*, pp. 547–568.

[55] Neutrino Geophysics: Proceedings of Neutrino Sciences 2005 Volume 99, Issues 1-4 of Earth, moon, and planets, ISSN 0167-9295, Stephen T. Dye, Springer 2007.

[56] Fiorentini, G., Lissia, M., Mantovani, F., "*Geo-neutrinos and earth's interior*", Physics Reports, Volume 453, Issues 5–6, December 2007, Pages 117-172, ISSN 0370-1573, http://dx.doi.org/10.1016/j.physrep.2007.09.001.

[57] Enomoto, S., 2005, "*Neutrino Geophysics and Observation of Geo-Neutrinos at KamLAND"*, Ph.D. thesis, Tohoku University, http://www.awa.tohoku.ac.jp/~sanshiro/research/SanshirosDoctoralDissertation.pdf.

[58] *www.iea.org/publications/freepublications/publication/kwes.pdf*, 08/01/2014, 13h00.

[59] http://www.iaea.org/pris/, 08/01/2014, 13h05.

[60] Klimov, Yu. V., Kopeikin, V.I., Mikaélyan, L.A., Ozerov, K.V and Sinev., V.V., 1994, Atomic Energy 76 (2), p123-127.

[61] Bowden, N.S. *et al*., 2007, Nucl. Instr. and Meth. A572, 985.

[62] Afonin, A.I., Ketov, S.N., Kopeikin, V.I., *et al*., JETP, 94, 1 (1988).

[63] Lewis, E. E., 2008, "*Fundamentals of Nuclear Reactor Physics*", 1st edition, Academic Press.

[64] Loveland, W.D., Morrissey, D.J., Glenn T. Seaborg, 2005, "*Modern Nuclear Chemistry*", 1st edition, Wiley-Interscience.

[65] McGregor, D.S., Vernon, S.M., Gersch, H.K., Markham, S.M., Wojtczuk, S.J. and Wehe, D.K., IEEE Trans. Nuclear Science, 47 (2000) p. 1364.

[66] de Meijer, R.J., Anisichkin, V.F., van Westrenen, W., "*Forming the Moon from terrestrial silicate-rich material*", Chemical Geology, Volume 345, 8 May 2013, Pages 40-49.

[67] http://b-inet.com/intellect/technology/nuclear-reactor/, 08/01/2014, 15h46.

[68] Fallot, M., *et al*., Phys.Rev.Lett. 109, 202504 (2012).

[69] Huber, P., "*Determination of antineutrino spectra from nuclear reactors*," Physical Review C, vol. 84, no. 2, Article ID 024617, 16 pages, 2011, Erratum-ibid. vol. 85, Article ID 029901, 2012.

[70] Cao, J., "*Determining reactor neutrino flux*," Nuclear Physics B-Proceedings Supplements. In press, http://arxiv.org/abs/1101.2266, Proceeding of Neutrino 2010.

[71] Cribier, M., Nuclear Physics B (Proc. Suppl.) 221 (2011) 57–61.

[72] Bernstein, A. *et al.* J.Appl.Phys. 103 (2008).

[73] Nieto, M., *et al*., "*Detection of anti-neutrinos for non-proliferation*", Nucl. Sci. Engin. 149 (2005) 270-276.

[74] Kessler, G., 2011, "*Proliferation-Proof Uranium / Plutonium Fuel Cycles Safeguards and Non-Proliferation*", KIT Scientific Publishing.

[75] Bernstein, A., *et al*., "*Monitoring reactors with cubic meter scale anti-neutrino detectors*", in: R. Avenhaus *et al*.: Verifying treaty compliance: limiting weapons of mass destruction and monitoring, Kyoto Protocol Provisions, Springer, Berlin (2006).

[76] Kopeikin, V.I., Phys.Atom.Nucl. 66 (2003) 472-475, Yad.Fiz. 66 (2003) 500-503 hep-ph/0110030.

[77] Reines, F. and Cowan, C.L. Jr., 1959, Phys. Rev. 113, p273.

[78] Final Report: Focused Workshop on Antineutrino Detection for Safeguards Applications, 28-30 October 2008, IAEA Report STR-361, IAEA, 2009.

[79] Bowden, N.S., 2008, J. Phys. Conf. Ser. 136 (2).

[80] Knoll, G.F., 2000, "*Radiation Detection and Measurements"*, 3rd edition, John Wiley & Sons, New York.

[81] Leo, W.R., 1987, "*Techniques for Nuclear and Particle Physics Experiments*", Springer-Verlag Berlin Heidelberg.

[82] Harpen, Michael D., **"***Positronium: Review of symmetry, conserved quantities and decay for the radiological physicist*", *Med Phys.* 2004 Jan; 31(1):57-61.

[83] Debertin, K. and Helmer, R. G., 1988, "*Gamma- and X-Ray Spectrometry with Semiconductor Detectors*" North-Holland, Amsterdam.

[84] Stapel, C., Limburg, J., De Meijer, R.J. (1997): "*Calibration of BGO scintillation detectors in a bore-hole geometry*". KVI internal report Z-62.

[85] Bevington, P. R. and Robinson, D.K., 1992, "*Data reduction and error analysis for the physical sciences*", 3rd edition, WCB/McGraw-Hill.

[86] Madesen, B., 2011, "*Statistics for non-statisticians*", Springer-Verlag Berlin Heidelberg.

[87] Hughes, I.G. and Hase, T.P.A., 2010, "*Measurements and their uncertainties – A practical guide to modern error analysis*", Oxford University Press Inc., New York.

[88] Daly, F., Hand, D.J., Jones, M.C., Lunn, A.D. and McConway, K.J., 1995, "*Elements of statistics*", Addison-Wesley, The Open University.

[89] Danon, Y., Sones, B. and Block, R., 2007, Nucl. Instr. and Meth. A524, 287.

[90] E.V.D. van Loef., *et al*., Appl. Phys. Lett. 79 (2001) 1573.

[91] Quarati, F.G.A., *et al*., Nucl. Instr. and Meth. A 629 (2011) 157.

[92] Firestone, R.B. and Shirley, V.S., 1998, "*Table of Isotopes*", 8th edition, John Wiley & Sons.

[93] Kohn, M.J. and Vervoort, J.D., 2008, "*U-Th-Pb dating of monazite by single-collector ICP-MS: Pitfalls and potential*", Geochem. Geophys. Geosyst., 9, doi: 10.1029/2007GC001899.

[94] Zucker, M.S., 1985, "*Improved method for the stabilization of NaI-photomultiplier gamma detectors against thermal and other drift*". In 6. symposium on X- and gamma-ray sources and applications, Ann Arbor, MI, USA, 21 May 1985. Retrieved from http://www.osti.gov/scitech/servlets/purl/5844841.

[95] http://nemu.web.psi.ch/doc/manuals/device_manuals/PhotoMultiplier/Photonis.pdf, 28/01/2014, 09h41.

[96] Moszynski, M., *et al*., Nucl. Instr. and Meth. A 568 (2006) 739–751.

[97] Uckan, T., *et al*., "*Spectral Multi-peak Analysis Methodology for Eliminating Effects of NaI Temperature Drift*", Proceedings of the Institute of Nuclear Materials Management Ann; 2010, p1.

[98] Birk, M., Eisen, Y. and Vager, Z., Nucl. Instr. and Meth. A 108 (1973), 611 – 612.

[99] Hehl, T., *et al*., Nucl. Instr. and Meth. A 354 (1995), 505–510.

[100] http://www.hamamatsu.com/resources/pdf/etd/PMT_handbook_v3aE-Chapter7.pdf, 28/01/2014, 09h52.

[101] Reeder P.L., and Stromswold, D.C., 2004, "*Performance of Large NaI(Tl) Gamma-Ray Detectors Over Temperature -50 Degrees C to +60 Degrees C",* PNNL-14735, Pacific Northwest National Laboratory, Richland, WA.

[102] Casanovas, R., *et al*., "*Temperature peak-shift correction methods for NaI(Tl) and $LaBr_3$(Ce) gamma-ray spectrum stabilisation*", *Radiation Measurements,* vol. 47 issue 8, August, 2012, p. 588.

[103] Dathy, C., 2005. Saint-Gobain letter to customer. Available at www.detectors.saintgobain.com/Media/Documents/S00000000000000001004/BrilLanCeLetterOctober2005.pdf.

[104] De Meijer, R.J., Stapel, C., Jones, D.G., Roberts, P.D., Rozendaal, A., MacDonald, W.G., (1997): "*Improved and New Uses of Natural Radioactivity in Mineral Exploration and Processing*". Exploration Mining Geology 6, 105-117.

[105] Hendriks P.H.G.M., (2003), *"In-Depth γ-ray studies - Borehole measurements"*, Ph.D. dissertation, ISBN90-376-1758-2.

[106] Maleka, P.P., (2010), "*In-situ element analysis from gamma-ray and neutron spectra using a pulsed-neutron source*", Ph.D. dissertation, ISBN: 978-90-367-4328-0.

[107] www.ortec-online.com/download/905-series.pdf, 26/04/2014, 12h40.

[108] Zhu, R. Y., (1998), "*Radiation damage in scintillating crystals*", Nucl. Instr. and Meth. A: Accelerators, Spectrometers, Detectors and Associated Equipment, 413(2), 297-311.

[109] GORDON, R. B., (1959), "*Color centers in crystals*", American Scientist, 361-375.

[110] Tilley, R. J., (2000). "*Defects in Solids*", John Wiley & Sons, Ltd.

[111] Wissmann, F., "*Variations observed in environmental radiation at ground level*", Radiation Protection Dosimetry (2006), Vol. 118, No. 1, pp. 3–10.

[112] Kossert, K., *et al*., "*Long-term measurements of ^{36}Cl to investigate potential solar influence on the decay rate*", *Astroparticle Physics 55*, 33 (2014).

[113] Sturrock, P.A., *et al*., "*Analysis of beta-decay rates for Aug108, Ba133, Eu152, Eu154, Kr85, Ra226, and Sr90, measured at the Physikalisch-Technische Bundesanstalt from 1990 to 1996*", ApJ 794 42 (2014).